This dissertation focuses on spin based phenomena of transport in low-dimensional mesoscopic systems. The work contains the theoretical discussion of an experimentally verified spin-transistor concept, which is based on controlling adiabaticity of spin evolution in dilute magnetic semiconductors. Furthermore the effect of spin dephasing on the weak localization and the weak antilocalization conductance corrections is investigated.

In this context, the influence of spin-orbit interaction that scales cubically with the momentum on n- and p-type charge transport is examined. The analyses presented here are based on numerical transport simulations and semiclassical frameworks.

Universitätsverlag Regensburg

9 783868 451078

ISBN 978-3-86845-107-8
gefördert von:
Alumni der physikalischen Fakultät der Universität Regensburg e.V.

UR
Universität Regensburg

Dissertationsreihe Physik - Band 38

Tobias Dollinger

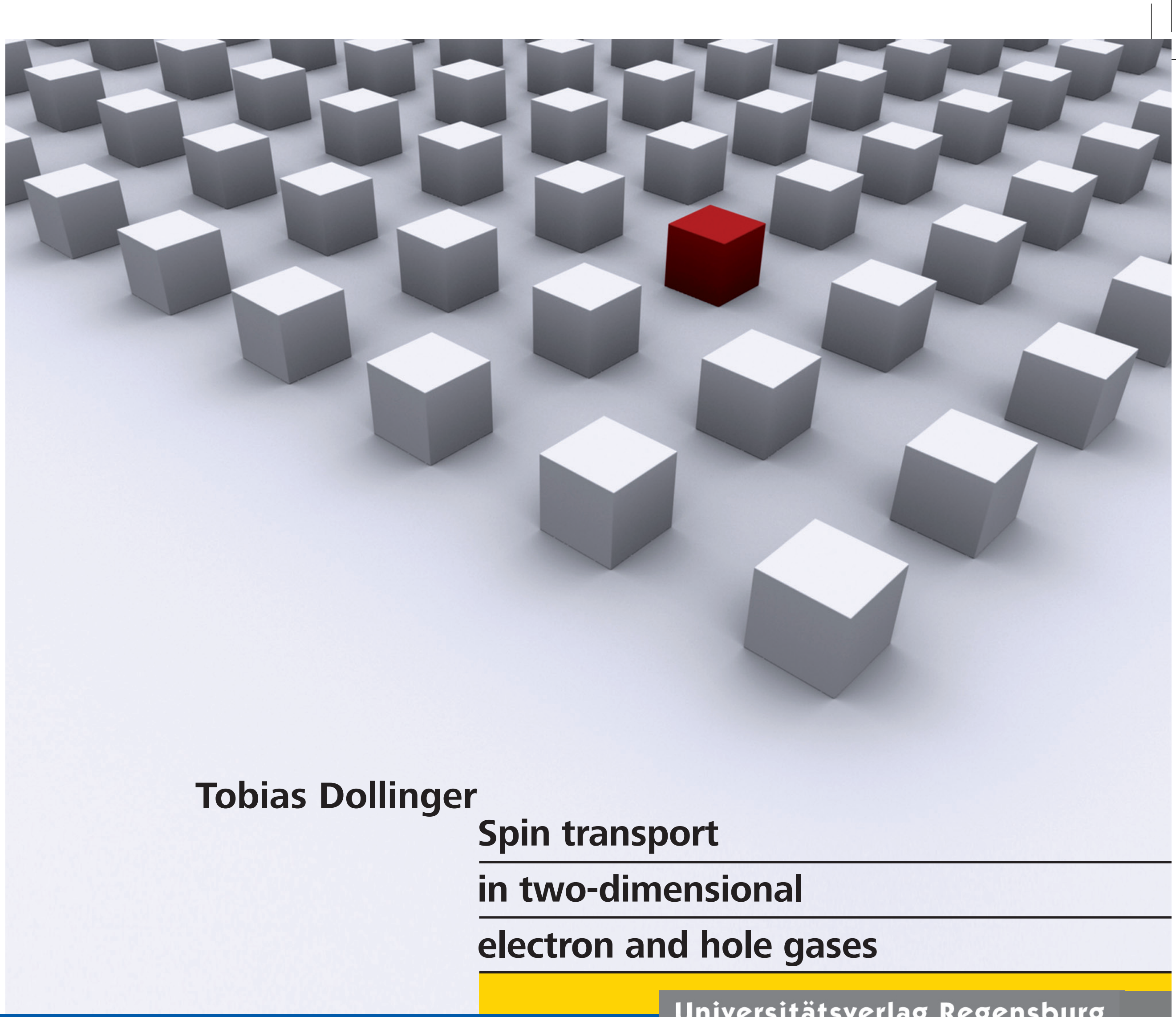

Tobias Dollinger

Spin transport in two-dimensional electron and hole gases

Universitätsverlag Regensburg

38

Dissertationsreihe Physik

Tobias Dollinger

Spin transport
in two-dimensional
electron and hole gases

Spin transport in two-dimensional electron and hole gases

Dissertation zur Erlangung des Doktorgrades der Naturwissenschaften (Dr. rer. nat.)
der naturwissenschaftlichen Fakultät II - Physik der Universität Regensburg
vorgelegt von

Tobias Dollinger

aus Schwabmünchen
im Dezember 2013

Die Arbeit wurde angeleitet von: Prof. Dr. Klaus Richter.
Promotionsgesuch eingereicht am 01.10.2009.

Prüfungsausschuss:	Vorsitzender:	Prof. Dr. Dieter Weiss
	1. Gutachter:	Prof. Dr. Klaus Richter
	2. Gutachter:	Prof. Dr. John Schliemann
	weiterer Prüfer:	Prof. Dr. Gunnar Bali

Dissertationsreihe der Fakultät für Physik der Universität Regensburg, Band 38

Herausgegeben vom Präsidium des Alumnivereins der Physikalischen Fakultät:
Klaus Richter, Andreas Schäfer, Werner Wegscheider

Tobias Dollinger

Spin transport in two-dimensional electron and hole gases

Universitätsverlag Regensburg

Bibliografische Informationen der Deutschen Bibliothek.
Die Deutsche Bibliothek verzeichnet diese Publikation
in der Deutschen Nationalbibliografie. Detailierte bibliografische Daten
sind im Internet über http://dnb.ddb.de abrufbar.

1. Auflage 2014

Leibnitzstraße 13, 93055 Regensburg

Konzeption: Thomas Geiger
Umschlagentwurf: Franz Stadler, Designcooperative Nittenau eG
Layout: Tobias Dollinger
Druck: Docupoint, Magdeburg
ISBN: 978-3-86845-107-8

Weitere Informationen zum Verlagsprogramm erhalten Sie unter:
www.univerlag-regensburg.de

References related to this work

Part of the material presented here has appeared in the following publications:

1. C. Betthausen, **T. Dollinger**, H. Saarikoski, V. Kolkovsky, G. Karczewski, T. Wojtowicz, K. Richter, and D. Weiss, *Spin-transistor action via tunable Landau-Zener transitions*, Science **337** (2012), 324, cited as Ref. [1].

2. H. Saarikoski, **T. Dollinger**, and K. Richter, *Spin transmission control in helical magnetic fields*, Phys. Rev. B **86** (2012), 165407, cited as Ref. [2].

3. M. Kohda, V. Lechner, Y. Kunihashi, **T. Dollinger**, P. Olbrich, C. Schönhuber, I. Caspers, V. V. Bel'kov, L. E. Golub, D. Weiss, K. Richter, J. Nitta, and S. D. Ganichev, *Gate-controlled persistent spin helix state in (In,Ga)As quantum wells*, Phys. Rev. B **86** (2012), 081306, cited as Ref. [3].

4. **T. Dollinger**, A. Scholz, P. Wenk, R. Winkler, J. Schliemann, and K. Richter. *Signatures of spin-preserving symmetries in two-dimensional hole gases*, arXiv:1304.7747 [cond-mat.mes-hall] (2013), submitted to Phys. Rev. B, cited as Ref. [4].

Contents

Chapter 1

Introduction

Research activities related to accessing the electronic spin have attracted significant attention [5]. The Nobel prizes in physics in the years 2007 and 2010 reflect the impact of this field of research on our society. The prizes awarded in 2007 to A. Fert and P. Grünberg for the discovery of the giant magnetoresistance (GMR), and in 2010 to A. Geim and K. Novoselov for experiments on the material Graphene are examples of achievements, that are related to accessing the quantum mechanical intrinsic magnetic moment of the electron, called spin [6].

Especially in the context of data storage and data processing, the rising field of spin based electronics -short, spintronics [7]- has promising potential applications. Proposals in this area go as far as replacing charge based logic by purely spin based logic [8]. This development is inspired by the strive to realize quantum algorithms of potentially dramatic impact [9, 10]. Apart from the ambition to reduce energy consumption [8], another argument motivates the ambition to advance beyond conventional charge based electronics-Moore's phenomenological law of an exponentially growing transistor density in microprocessors [11]. The advancing miniaturization of computational infrastructure, inevitably leads to a confrontation with the fundamental frontier represented by the laws quantum mechanics, which dominate the physics of small length scales [12]. In addition to these points the spin degree of freedom plays a role in the vivid discussion about creating a novel type of quasiparticle at the edges of nanowires on s-wave superconductors, the Majorana Fermion, which is a Fermion that is its own antiparticle [13].

Advances in utilization of the spin degree of freedom have led to various applications that already influence our society [14]. Prominent examples of such applications include the significantly extended storage capacities of todays hard-drives, which are based on GMR-effect [15, 16], or the development of faster computers due to non-volatile magnetic random access memory, which is based on the tunneling magnetoresistance (TMR) [17, 18, 19] phenomenon [14]. GMR is based on the influence of magnetic polarization of the material on charge currents, which can be used to store and read out information [15, 16]. The related concept of TMR consists of two ferromagnetic layers, that are separated by a tunnel barrier, which gives rise to a resistance that is maximal for parallel magnetic polarization and minimal for an antiparallel configuration [17, 18, 19]. Both mechanisms are based on the differences in the density of states of the different carrier spin polarizations [20].

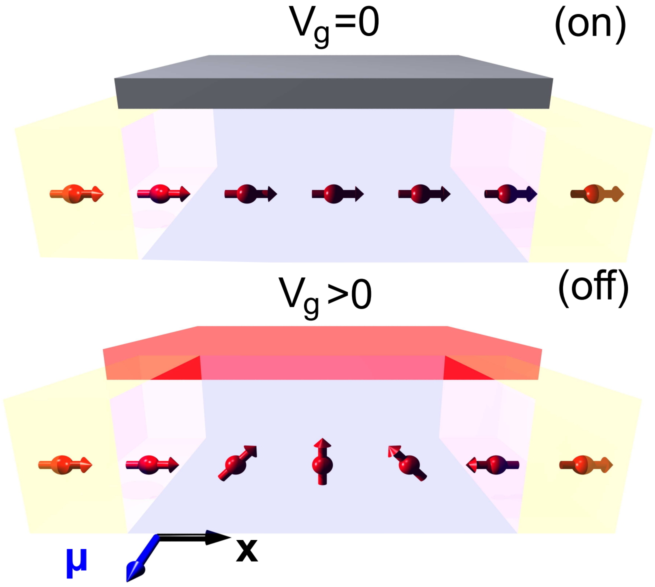

Figure 1.1: (Datta-Das spin transistor) Illustration of the Datta-Das concept of a ballistic spin field effect transistor [21]. Two materials with well defined carrier spin polarization (blue region) are connected by a gated region (yellow region) in which switching the top-gate voltage V_g allows to control spin-orbit interaction, which manifests itself in spin precession around a spin precession axis $\boldsymbol{\mu}$ (blue arrow) of carriers that move along x-direction. If carrier spin in the gated region is parallel to the spin orientation in the ungated region, a maximum overlap of the wavefunctions leads to ideal transmission, which corresponds to the “on” state. To achieve an “off“ state one tunes V_g and realizes a spin precession frequency such that at the right interface the spins are oriented in antiparallel direction, which prohibits transmission.

Part of the current research activity is aimed at the discovery of novel building blocks for future spin based computational devices [21, 22, 23, 24, 25, 26, 27, 28, 8, 29]. The proposal of Datta and Das, illustrated in Fig. 1.1, set this development in motion, since it suggested a simple principle to control and measure carrier spin in a semiconductor by exploiting spin-orbit interaction (SOI) [21].
In the majority of studied classes of semiconductors and their heterostruc-

tures [7], as well as in the present thesis, SOI manifests itself in the form of Bychkov-Rashba [30, 31] or Dresselhaus SOI [32]. The bulk inversion asymmetry of the individual crystal structure gives rise to the Dresselhaus SOI, which therefore is an intrinsic material property [32]. The Bychkov-Rashba term however is induced by asymmetry of the potential landscape in the individual heterostructure [30, 31], and can hence be altered by externally changing the voltage of a gate [33]. See Fig. 1.1 to get an impression how Datta and Das suggested to utilize the Bychkov-Rashba SOI, which gives rise to a precession of the spin. The device allows operations on one dimensional itinerant spin polarized carriers in form of ”on“ and ”off” configurations, that are accessed by switching between different voltages in the top gate [21]. The influence of coupling to additional bands provides an additional source of spin rotation [23]. Operations analogous to the electro-optic modulator are possible in such a device, which opens the possibility to access the quantum mechanical phase information of the spin for logical operations [21, 8].

Experimental attempts to realize the Datta-Das concept [28] however encountered significant obstacles, such as spin injection inefficiency [34] and the issue of various relaxation processes, to which spin is subject [35, 36]. Unfortunately, SOI, which we introduced as a means to control spin, is also a major source of spin relaxation and therefore responsible for the loss of spin information [35, 36]. The timescale of this relaxation is denoted spin lifetime or spin relaxation time [35].

Mentioned issues have initiated an ongoing quest for alternative concepts to create and access stable carrier spin within a device infrastructure.

For example, the proposal of a multi-terminal Onsager spin transistor is motivated by a generalized gauge argument that connects spin currents with the deviation from Onsager’s relation [37] for the spin independent conductance in a two-terminal geometry [29]. Furthermore, an experimental proof of concept was possible for a class off magnetic bipolar transistors [27], in which spin dynamics is reflected in the current-voltage characteristics of a bipolar transistor [26].

Among mentioned examples, one proposal is of particular relevance to the present work. The concept of a nonballistic spin-field-effect transistor, suggested by Schlieman et al., is operational despite the presence of disorder and SOI [25]. It is based on a spin preserving symmetry, that is established in two-dimensional heterostructure quantum wells when the Bychkov-Rashba term is of equal magnitude as the Dresselhaus term [25]. In the corresponding parameter regime, spin relaxation is drastically suppressed and spin evolution is described by a “persistent spin helix” (PSH) [38], that has been detected within transient spin grating spectra [39]. Recently mentioned effect allowed to realize spin lifetimes of $\sim 1\ \mathrm{ns}$ in a semiconductor, in which the PSH manifested itself in characteristic spatial distributions of the spin polarization, that have been mapped within the magneto-optical Kerr rotation technique [40]. The PSH-symmetry is of SU(2) type [38] and its specialization to a U(1) spin preserving symmetry has already been discovered in the mesoscopic conductance corrections within diagrammatic frameworks developed in the 90's [41, 42].

In a transistor, mentioned concept can be put to use in the presence of a constant Dresselhaus term, and a gate voltage to manipulate the Rashba term - which principally allows switching spin polarized currents on or off [25].

However, the symmetry required for the PSH, can only be achieved in materials, in which all contributions to the SOI are neglected, except for those which scale linearly in the crystal momentum k. The physical properties of systems with non-negligible k-cubic contributions to the SOI have to be re-examined carefully [39]. In two-dimensional electron gases (2DEGs) the Dresselhaus contribution includes such k-cubic terms [42]. In two-dimensional hole gases (2DHGs) even the overall momentum dependence of the SOI is to leading order of cubic nature [43, 44, 45]. This motivates us to address the question, whether also 2DHGs possess symmetries, which allow the control spin relaxation.

The objective of the present thesis is to extend the existing knowledge on conditions that allow reliable injection, procession and extraction of spin information. We will illustrate concrete examples of setups, which allow to circumvent the problem of spin relaxation, including systems with k-cubic SOI.

One possibility to achieve this, is by fixing the spin precession axis, by large Zeeman interaction that can be realized in dilute magnetic semiconductors [46]. These points are combined in the following two topics, that are covered in our work.

- Introduction of a novel concept to control spin by inducing or prohibiting Landau-Zener transitions in magnetic semiconductors [1, 2].
- Analysis of parameter regimes corresponding to drastically enhanced spin lifetimes in disordered two-dimensional electron and hole gases with k-cubic spin-orbit interaction [3, 4].

We begin our discussion with an introduction of the considered systems and their respective models in **Chap. 2**. Our discussion covers two-dimensional systems realized in the conduction band as well as the valence band of semiconductors. We review the derivation of the **electronic Hamiltonian model**, including Bychkov-Rashba and Dresselhaus SOI and the special case of magnetically doped materials, in which a significant Zeeman interaction can be realized.

Furthermore we present an effective 2×2 **model for [001] heavy hole quantum wells** that generalizes existing models [43, 44, 45] by including non-axially symmetric terms. Our approach allows for an intuitive understanding of the systems symmetry properties and pointing out similarities to or deviations from the electronic case.

In the present work we focus on transport as means to approach spin dependent material properties. Therefore we continue in **Chap. 3** with an introduction to **transport formalisms** on which our analysis is based, the numerical recursive Green's function approach [47] from which we obtain principally exact results and semiclassical techniques, which we use to interpret the numerical findings.

In **Chap. 4** we present a spin transistor concept which is based on controlling the adiabaticity of the **spin evolution in the dilute magnetic semiconductor Cd(Mn)Te** with giant Zeeman interaction. Our concept - developed in collaboration with the experimental group of Prof. Dieter Weiss - is based on spatially modulated magnetic field textures, that are reflected in (anti-)crossings in the local energy bands of charge carriers with finite spin polarization. The Landau-Zener [48, 49] tunneling induced by the local band minima can be manipulated experimentally and allows for the robust control of spin polarized currents.

Chapter 5 is devoted to an analysis of **mesoscopic conductance corrections in the presence of k-cubic SOI** and the connection of observed phenomena with spin relaxation. We investigate the effect of k-cubic SOI on the PSH symmetry in the electron gas, and interpret the experimental findings of the groups of Prof. Sergey Ganichev and Prof. Dieter Weiss from Regensburg and the group of Prof. Junsaku Nitta from Sendai. We confirm numerically the significance of the influence by the k-cubic SOI on the conductance corrections and discuss conditions for the conservation of the electron spin. Furthermore, in collaboration with the theoretical group of Prof. John Schliemann, we investigate regimes of diminished spin relaxation in valence band heavy-hole quantum wells, in which we identify an analogue to the PSH-symmetry of the conduction band.

Chapter 2

Two dimensional systems in quantum well confinements

2.1 Spin-orbit coupling of a free charged particle

In the present work we discuss effects related to the spin degree of freedom on transport properties of mesoscopic systems. Originally the spin property arises in the Lorentz covariant description of the quantum mechanical wavefunction Ψ of a free electron with mass m and charge e. The latter is given by the Dirac equation [50],

$$[\gamma^{\mu}\left(p_{\mu}+\mathrm{e}A_{\mu}\right)-mc]\,\Psi=0, \tag{2.1}$$

where vector potential $\boldsymbol{A}$ and scalar potential Φ enter in terms of the covariant vector $A^{\mu}=(\phi,\boldsymbol{A})$, with the magnetic field $\boldsymbol{B}=\nabla\times\boldsymbol{A}$. The constant c denotes the speed of light in vacuum in the given context. Preceding results are given in cgs units, all further expressions in this text will be given in SI units, unless otherwise stated. In the theory of condensed matter, the structure of Eq. (2.1) is still subject to ongoing research, since it is recovered in the tight-binding description of electrons in Graphene, which leads to unique phenomena such as Klein-tunneling [50] and enhanced spin relaxation times even at larger temperatures [51]. The left hand side of Eq. (2.1) depends linearly on the momentum $p^{\mu}=(E/\mathrm{c},\boldsymbol{p})$, with $\boldsymbol{p}=-i\hbar\boldsymbol{\nabla}$ and the matrices

$$\gamma^{i}=\begin{pmatrix}0 & \sigma^{i}\\ -\sigma^{i} & 0\end{pmatrix}\quad\text{and}\quad\gamma^{0}=\begin{pmatrix}\sigma^{0} & 0\\ 0 & -\sigma^{0}\end{pmatrix}, \tag{2.2}$$

that contain the Pauli matrices,

$$\sigma_0 = \mathbb{1}_{2\times 2} = \begin{pmatrix} 1 & 0 \\ 0 & 1 \end{pmatrix}, \quad \sigma_1 = \sigma_x = \begin{pmatrix} 0 & 1 \\ 1 & 0 \end{pmatrix}, \quad \sigma_2 = \sigma_y = \begin{pmatrix} 0 & -i \\ i & 0 \end{pmatrix} \\ \text{and} \quad \sigma_3 = \sigma_z = \begin{pmatrix} 1 & 0 \\ 0 & -1 \end{pmatrix}. \tag{2.3}$$

Within the approach mentioned above, the spin structure in Eq. (2.1) is a direct consequence of the relativistic description of a quantum mechanical particle [50]. We will now consider the non-relativistic limit, that is of relevance for materials, in which electrons move at Fermi velocity v_{F} that is typically much smaller than c [52].

For our purposes also the influence of atomic potentials to which the moving particle is exposed, have to be considered. The latter can be approached within the Fouldy-Wouthuysen transformation, which is a unitary transformation applied on Eq. (2.1), calculated from a perturbation expansion in the parameter $1/m$, in order to remove non-diagonal terms in Eq. (2.1) [50]. A similar approach is presented in Ref. [53], where the expansion is executed in the variable v/c to arrive at the Pauli equation

$$\begin{aligned} H_{\text{Pauli}} = & \frac{\boldsymbol{\pi}^2}{2m} - \frac{\boldsymbol{p}^4}{8m^3c^2} + e\Phi + \frac{e\hbar}{2m}\boldsymbol{\sigma}\cdot\boldsymbol{B} \\ & - \frac{e\hbar^2}{8m^2c^2}\nabla\cdot\boldsymbol{E} - \frac{e\hbar}{4m^2c^2}\boldsymbol{\sigma}\cdot\boldsymbol{p}\times\boldsymbol{E} - \frac{e\hbar p^2}{4m^3c^2}\boldsymbol{\sigma}\cdot\boldsymbol{B} - \frac{(e\hbar B)^2}{8m^3c^2}, \end{aligned} \tag{2.4}$$

which describes the non-relativistic limit of the upper 2×2 sub-block in the 4×4 space of Eq. (2.1), where $\boldsymbol{\pi} := \boldsymbol{p} + e\boldsymbol{A}$ and $\boldsymbol{\sigma}$ denotes the vector of the Pauli matrices. The first line of Eq. (2.4) contains the electrostatic and magnetic dipole energy. The leading term in the second line is the Darwin-Term, associated with the Zitterbewegung [50]. For a spherically symmetric potential Φ one finds the second term in the same line of Eq. (2.4), which can be written as Pauli's spin-orbit interaction (SOI),

$$H_{\text{SOI}} = -\frac{\hbar}{4m^2c^2}\boldsymbol{\sigma}\cdot\boldsymbol{p}\times(\nabla V). \tag{2.5}$$

This expression inherits its name from the coupling between the spin $\boldsymbol{\sigma}$ and the orbital momentum $\boldsymbol{p}$, for which it is responsible [50]. After having introduced the basics on the spin degree of freedom, we are going to use above results in order to describe the electronic wavefunction in a solid.

2.2 kp-method and Envelope Function Approximation

In the the present work we focus on charge carriers that are subject to a spatially periodic potential of a crystal lattice. The resulting translational symmetry can be utilized by expanding the wave function of the problem in Bloch functions $e^{i\boldsymbol{k}\cdot\boldsymbol{r}}u_{\nu,\boldsymbol{k}}(\boldsymbol{r})$, where $u_{\nu,\boldsymbol{k}} = \langle \boldsymbol{r}|\nu,k\rangle$ are periodic functions on the lattice with band index ν [54]. For considering both the spin degree of freedom σ and the orbital quantum number ν the usage of the common quantum number n is appropriate, since in the presence of SOI spin is in general no longer a good quantum number [53]. Upon application of the non-relativistic kinetic Hamiltonian and the Pauli spin-orbit term (2.5) one finds a Schrödinger equation for the functions $u_{n,\boldsymbol{k}}$ within the $\boldsymbol{k}\cdot\boldsymbol{p}$-theory [53, 55]. Similar to the approach of Kohn and Luttinger in Ref. [56] one can further expand the objects $|\nu,k\rangle$ in the product basis $\{|\nu'\sigma'\rangle\}$ of spin states $|\sigma\rangle$ and band edge Bloch functions $|\nu,0\rangle$ as

$$|n,\boldsymbol{k}\rangle = \sum_{\nu',\sigma'} c_{n\nu'\sigma'}(\boldsymbol{k})\,|\nu'\sigma'\rangle\,, \tag{2.6}$$

and obtain a matrix equations for the coefficients $c_{n\nu'\sigma}$:

$$\sum_{\nu',\sigma'}\left\{\left[E_{\nu'}(0)+\frac{\hbar^2\boldsymbol{k}^2}{2m}\right]\delta_{\nu\nu'}\delta_{\sigma\sigma'}+\frac{\hbar}{m}\boldsymbol{k}\cdot\boldsymbol{P}_{\substack{\nu\nu'\\ \sigma\sigma'}}+\Delta_{\substack{\nu\nu'\\ \sigma\sigma'}}\right\}c_{n\nu'\sigma'}(\boldsymbol{k}) \\ = E_n(\boldsymbol{k})c_{n\nu\sigma}(\boldsymbol{k}), \tag{2.7}$$

with the matrix elements of the momentum

$$\boldsymbol{P}_{\substack{\nu\nu'\\ \sigma\sigma'}} := \langle\nu\sigma|\,\boldsymbol{\pi}\,|\nu'\sigma'\rangle\,, \tag{2.8}$$

$$\text{and the SOI}\quad \Delta_{\substack{\nu\nu'\\ \sigma\sigma'}} := \langle\nu\sigma|\,\boldsymbol{p}\cdot\sigma\times(\nabla V)\,|\nu'\sigma'\rangle\,. \tag{2.9}$$

The eigenvalues of the infinite dimensional problem defined by Eq. (2.7) yield the exact energies $E_n(\boldsymbol{k})$ [53]. Electromagnetic fields which oscillate slowly over one lattice constant can be treated within the Envelope Function Approximation (EFA) [53]. In this case one arrives at a set of coupled differential equations which have the matrix structure of Eq. (2.7), except for the following differences. Instead of describing $\{c_{n\nu'\sigma}\}$, the EFA equations determine the modulation coefficients of the Bloch functions, the crystal momentum $\hbar\boldsymbol{k}$ is replaced by the corresponding kinetic momentum $\boldsymbol{\pi}$ including the vector potential, and the Zeeman term

$$H_{\mathrm{Z}}^{0} = \frac{\mu_{\mathrm{B}}\mathrm{g}}{2}\boldsymbol{\sigma}\cdot\boldsymbol{B}\delta_{\nu\nu'}\,, \tag{2.10}$$

has to be added under the summation symbol in Eq. (2.7), accounting for the coupling of magnetic field and spin [53]. The constant $\mu_{\mathrm{B}} = e\hbar/2m$ is referred to as Bohr magneton [54].

For a vast range of situations it is fortunately not necessary to compute the eigenvalues of the full infinite-dimensional matrix given in Eq. (2.7). For the cases examined in the scope of the present work, an accurate approximation of the exact energies can be found in a finite-dimensional Hilbert space.

In summary, it is on the one hand Löwdin's perturbation theory [57] that allows one to focus on energies within a subspace of Eq. (2.7), while treating the

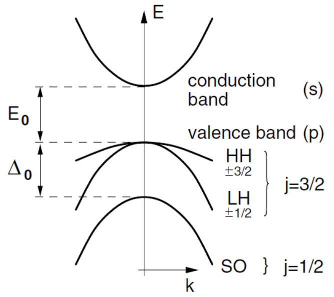

Figure 2.1: (band structure scheme) Sketch from Ref. [53] outlining the band structure of a typical III-IV semiconductor.

coupling to states spanning the remaining Hilbert space as a perturbation. A specialized application on our starting point (2.7) is described in Refs. [53, 58], which utilizes a perturbative construction of an unitary transformation, that decouples the finite subspace from the rest of the matrix. This is analogous to the previously described method applied by Fouldy and Wouthuysen in the context of relativistic electrons [53].

An alternative method to reduce the full $\boldsymbol{k} \cdot \boldsymbol{p}$ problem to a finite dimensional effective Hamiltonian is given in terms of the theory of invariants, which allows a construction of the Hamiltonian from the invariants of the symmetry group corresponding to a particular material [53, 58].

Both of these approaches help to derive the band structure of zinc blende type materials, that are based on a face centered cubic lattice with diatomic basis on the $(0, 0, 0)$ and $(1/4, 1/4, 1/4)$ positions [54].

2.3 Band structures and Kane model

Kane's 8×8 matrix model allows for the interpretation of semiconductor band structures as shown in Fig. 2.1 from Ref. [53], which sketches the typical band structure close to the Γ-point of a direct semiconductor. As indicated, conduction and valence bands are usually split by a finite energy gap E_0 and a so called split-off term Δ_0 separates the heavy hole (HH) and light hole (LH) states from the split-off (SO) states further below the Fermi energy [53].

In agreement with the atomistic tight-binding description of the material, the conduction band and the SO-states correspond to s-orbitals that have a total angular momentum quantum number $j = 1/2$, associated with the spin, while the two upper valence band states are described by p-type orbitals with $j = 3/2$ [53]. The Hilbert spaces corresponding to the various angular momenta are recovered intuitively in Kane's model [53], that leads to spectra such as

Fig. 2.1 close to the conduction band edge,

$$H_{8\times 8}^{\text{Kane}} = \begin{pmatrix} H_{6c6c} & H_{6c8v} & H_{6c7v} \\ H_{8v6c} & H_{8v8v} & H_{8v7v} \\ H_{7v6c} & H_{7v8v} & H_{7v7v} \end{pmatrix}. \tag{2.11}$$

The notation in Eq. (2.11) is identical to its formulation in Ref. [53], where the matrix blocks H_{6c6c}, H_{8v8v} and H_{7v7v} describe the isolated conduction band, HH-LH band and the SO band respectively, while the off-diagonal blocks represent the coupling between the different sub-blocks. According to Löwdin's theory [57] we can consider the spectra of the different sub-blocks separately, if the corresponding energy levels are sufficiently remote from the levels of other bands. In the scope of this thesis we consider the split-off band well separated from the other states, since the theoretical spacings Δ_0^{theo} as well as the experimental values Δ_0^{exp} indicate this for the materials relevant to this work. Particular values include $\Delta_0^{\text{theo}}(\Delta_0^{\text{exp}})$ $\simeq$0.34(0.34) meV in GaAs, 0.4(0.38) meV in InAs and 0.94(0.92) meV in CdTe. In the following we will give the basic expressions for the electronic and the LH-HH sub-blocks.

2.4 Conduction band Hamiltonian

Electrons close to the Fermi surface in a three dimensional crystal can be modeled by an effective mass Hamiltonian [52, 53],

$$H_{6c6c} = \frac{\boldsymbol{\pi}^2}{2m_\star}\mathbb{1}_{2\times 2} + E_c\mathbb{1}_{2\times 2}. \tag{2.12}$$

For convenience we assume an isotropic band structure and therefore a scalar effective mass $m_\star$, and a conduction band minimum at E_c. The kinetic energy term in Eq. (2.12),

$$\mathrm{H}_{\text{kin}} = \frac{\boldsymbol{\pi}^2}{2m_\star}\mathbb{1}_{2\times 2}, \tag{2.13}$$

is identical to the non-relativistic free electron single particle Hamiltonian with a rescaled mass $m_\star$. The reduction of the many particle problem to Eq. (2.12) is described in terms of Fermi liquid theory and valid at low temperatures and hight kinetic energies, when electron-electron as well as electron-phonon interactions can be neglected [54, 59]. The presence of a magnetic field $\boldsymbol{B}$ is taken into account via minimal coupling [60]. In addition, the presence of $\boldsymbol{B}$ lifts the spin degeneracy by giving rise to the Zeeman coupling term, which enters the Hamiltonian (2.12), like in Eq. (2.10), as

$$H_Z = \frac{\mu_{\text{B}} g^\star}{2}\boldsymbol{B}\cdot\boldsymbol{\sigma}, \tag{2.14}$$

where $g^\star$, the effective electronic g-factor replaces the vacuum value $g \approx 2$.

In dilute magnetic semiconductors, which will be subject to our discussion in Chap. 4, $g^\star$ may reach values of the order of 10^2, rendering the Zeeman term the second important energy scale in the system [46]. Now we focus on refining the model (2.12) further, by extending our model by SOI.

2.5 Valence band Hamiltonian

One of the most prominent models describing the HH and LH states of the valence band has been introduced by Luttinger [61]. It is given by the 4×4 Hamiltonian,

$$H_{8v8v} = -\frac{\hbar^2}{2m}\left(\gamma_1 \boldsymbol{k}^2 - 2\gamma_2\left[\left(J_x^2 - \frac{1}{3}J^2\right)k_x^2 + \mathrm{c.p.}\right] - 4\gamma_3\left[\{J_x, J_y\}\{k_x, k_y\} + \mathrm{c.p.}\right]\right), \tag{2.15}$$

with the material dependent Luttinger parameters γ_1, γ_2 and γ_3[1]. Since Eq. (2.15) describes the spectrum of the HH and LH states with $3/2\hbar$ angular momentum, the 4×4 matrix is spanned by the corresponding matrix operators where $\{J_x, J_y, J_z\}$ are the spin-3/2 matrices

$$J_x = \frac{1}{2}\begin{pmatrix} 0 & \sqrt{3} & 0 & 0 \\ \sqrt{3} & 0 & 2 & 0 \\ 0 & 2 & 0 & \sqrt{3} \\ 0 & 0 & \sqrt{3} & 0 \end{pmatrix}, \quad J_y = \frac{i}{2}\begin{pmatrix} 0 & -\sqrt{3} & 0 & 0 \\ \sqrt{3} & 0 & -2 & 0 \\ 0 & 2 & 0 & -\sqrt{3} \\ 0 & 0 & \sqrt{3} & 0 \end{pmatrix},$$

$$J_z = \frac{1}{2}\begin{pmatrix} 3 & 0 & 0 & 0 \\ 0 & 1 & 0 & 0 \\ 0 & 0 & 1 & 0 \\ 0 & 0 & 0 & -3 \end{pmatrix} \quad \text{and} \quad \mathbb{1}_{4\times 4} = \begin{pmatrix} 1 & 0 & 0 & 0 \\ 0 & 1 & 0 & 0 \\ 0 & 0 & 1 & 0 \\ 0 & 0 & 0 & 1 \end{pmatrix}. \tag{2.16}$$

Note that the angular momentum character of HH and LH states imposes particular symmetries on the band structure. These symmetries remain in the spectral anisotropies of a dimensionally reduced model for the HH-states, presented at a later point.

The conduction bands of crystals without inversion asymmetry, such as Si or Ge, described by Eq. (2.12), includes a twofold degeneracy [53]. The valence bands are fourfold degenerate at the center of the first Brillouin zone and twofold degenerate for finite momentum $\hbar\boldsymbol{k}$ [53].

2.6 Giant Zeeman splitting

If a II-VI or a III-V semiconductor is doped with a small quantity of the transition metal Mn, large Zeeman splittings can be observed at low temperatures [46, 1].

---

[1] The shorthand notation c.p. represents the cyclically permuted versions of the first element, as illustrated in Eq. (2.21) [53].

The corresponding g-factors can reach values of the order 100 and are attributed to interaction effects [53]. In n-type systems, such as Cd(Mn)Te, the s-like electron wavefunction couples to the localized d-orbitals of the Mn^{2+}-ions [46]. For p-doped materials, like Ga(Mn)As or In(Mn)As, the p-like wavefunction of the carriers is expected to display an even stronger coupling to the ions, giving rise to even larger g-factors and less sensitive to increasing temperatures than n-doped materials [62]. The underlying physics can be illustrated with a Kondo-like Hamiltonian,

$$H = -\sum_m J(\boldsymbol{r} - \boldsymbol{R}_m)\boldsymbol{S}_m \cdot \boldsymbol{\sigma}, \tag{2.17}$$

where $\boldsymbol{S}_m$ is the spin operator of the 3d shell of the Mn atom located at $\boldsymbol{R}_m$ [53]. An extended carrier wavefunction allows for a mean field approach to the problem, in which electrons, or holes respectively, are exposed to the uniform average magnetic moment of the Mn-ions, aligned along a magnetic field $\boldsymbol{B}$ [53]. As outlined in Refs. [53, 63], this picture simplifies Eq. (2.17) to the Hamiltonian (2.10), where the material specific Landé g-factor $g^\star$ is modified according to

$$g_{\mathrm{eff}} = g^* + \alpha N_0 x_{\mathrm{eff}} \frac{S}{\mu_{\mathrm{B}} B} \mathcal{B}_S \left(\frac{g\mu_{\mathrm{B}} S B}{k_{\mathrm{B}}(T + T_{\mathrm{AF}})} \right). \tag{2.18}$$

The quantity x_{eff} is determined by the Manganese concentration x. The number αN_0 is the *s-d* or *p-d* exchange energy, k_{B} the Boltzmann constant and $\mathcal{B}_S$ the Brillouin function with $S = 5/2$ and $g = 2$, for electronic systems. The functions $x_{\mathrm{eff}}(x) < x$ and $T_{\mathrm{AF}}(x) > 0$ describe the reduction of the magnetization due to anti-ferromagnetic interactions between Manganese spins [46]. The temperature dependence of the problem enters the Brillouin function [54],

$$\mathcal{B}_S(y) = \frac{S + 1/2}{S} \coth\left(\frac{S + 1/2}{S} y \right) - \frac{1}{2S} \coth\left(\frac{y}{2S} \right). \tag{2.19}$$

2.7 Spin-orbit interaction in three dimensions

Important insights concerning relevant contributions to the spin dynamics include Luttinger's and Kohn's description of charge carriers in diamond or zinc blende type materials [60], and the finding of Dresselhaus, who was able to identify selection rules for the perturbative couplings by group theoretic reasoning [32]. In the following we will summarize the relevant couplings to the spin degree of freedom in these materials. Dresselhaus' result allows for the inference from cyclotron resonance experiments in zinc blende materials to the presence of SOI as result of the absence of bulk inversion asymmetry (BIA), nowadays recognized as Dresselhaus SOI [53].

Bulk inversion symmetry is present in crystals described by a centered cubic lattice with the basis vectors $(0, 0, 0)$ and $(1/4, 1/4, 1/4)$ [54]. However, although this diamond structure does not possess a center of inversion in the strict sense, inversion in combination with a translation maps the diamond structure to itself [53]. Crystalline Si and Ge represent examples for materials with diamond structure, leading to a preserved spin degeneracy [54].

Bulk inversion symmetry manifests itself in the degeneracy of the local spin bands in k-space, $E_\sigma(\boldsymbol{k}) = E_{-\sigma}(\boldsymbol{k})$ [53]. This degeneracy can be lifted by three types of effects described in the following.

Replacing one atom in the mono-atomic basis of the diamond structure by a different element yields zinc blende structure - for example realized in III-V material systems, such as GaAs, InGaAs or II-VI compounds like CdTe [54, 53]. The latter class of materials will be subject to our discussion.

2.7.1 Spin-orbit interaction from bulk-inversion asymmetry

In contrast to the diamond structure crystals, the presence of different atoms in zinc blende type materials induces electrical dipole moments on the microscopic level [53]. This leads to bulk inversion asymmetry (BIA) in the lattice. The BIA manifests itself in the Dresselhaus contribution to the Hamiltonian [32]. In the electronic band of many prominent semiconductors it is given by the expression [53]

$$H_{\mathrm{BIA}}^{\mathrm{bulk,6c6c}} = \boldsymbol{\mu}_{\mathrm{BIA}}^{\mathrm{bulk,6c6c}} \cdot \boldsymbol{\sigma}, \tag{2.20}$$

with

$$\left[\boldsymbol{\mu}_{\mathrm{BIA}}^{\mathrm{bulk,6c6c}}\right]_i = \frac{2b_{41}^{6c6c}}{\hbar^3} \sum_{i=1}^{3} \sum_{j=1}^{3} p_i \epsilon_{ijk} p_k^2 \hat{e}_i = b_{41}^{6c6c} \left(\left\{k_x, k_y^2 - k_z^2\right\} \hat{e}_x + \mathrm{c.p.}\right), \tag{2.21}$$

where the Cartesian coordinate system $\{\hat{e}_x, \hat{e}_y, \hat{e}_z\}$ is oriented along the crystallographic axes $\{[100], [010], [001]\}$.

For the heavy and the light hole states of the valence band, the corresponding term is given by

$$\begin{aligned} H_{\mathrm{BIA}}^{\mathrm{bulk,8v8v}} = & \frac{2C_k}{\sqrt{3}} \left[k_x \left\{J_x, J_y^2 - J_z^2\right\} + \mathrm{c.p.}\right] \\ & + b_{41}^{8v8v} \left[\left\{k_x, k_y^2 - k_z^2\right\} J_x + \mathrm{c.p.}\right] \\ & + b_{42}^{8v8v} \left[\left\{k_x, k_y^2 - k_z^2\right\} J_x^3 + \mathrm{c.p.}\right] \\ & + b_{51}^{8v8v} \left[\left\{k_x, k_y^2 + k_z^2\right\} \left\{J_x, J_y^2 - J_z^2\right\} + \mathrm{c.p.}\right] \\ & + b_{52}^{8v8v} \left[k_x^3 \left\{J_x, J_y^2 - J_z^2\right\} + \mathrm{c.p.}\right]. \end{aligned} \tag{2.22}$$

The bracket operator indicates the anti-commutator, $\{a, b\} = \frac{1}{2}(ab + ba)$. Table 6.3. of Ref. [53] summarizes values of the parameters C_k, b_{41}^{8v8v}, b_{42}^{8v8v}, b_{51}^{8v8v}

and b_{52}^{8v8v} for several materials. The quantities proportional to $b_{42}^{\mathrm{8v8v}}, b_{51}^{\mathrm{8v8v}}$ and b_{52}^{8v8v} are usually neglected, since the corresponding contributions have energies that are about two orders of magnitude smaller than the other terms [45]. However, it should be mentioned that theoretically calculated and experimentally found values of the Dresselhaus SOI strength vary over a wide range [64].

2.7.2 Structural asymmetry induced SOI

In addition to the material specific asymmetry discussed previously, structural inversion asymmetry (SIA) is an essential property of in a wide range of experimental setups. Contrasting to BIA, the type and strength of the SIA is accessible by experimental means. The presence of an electric field $\boldsymbol{E} = E_x\hat{\mathbf{x}} + E_y\hat{\mathbf{y}} + E_z\hat{\mathbf{z}}$ in the material causes this type of asymmetry. This field is realized in asymmetrically grown heterostructures, and can be influenced by the directed application of an external gate [33]. The tunability of $\boldsymbol{E}$ and thus control over the SIA represents the key ingredient to many semiconductor based applications in the field of spintronics [35]. Historically the SIA induced spin splitting has been first mentioned in the works of Bychkov and Rashba [30, 31]. Therefore the SIA type terms are also denoted as Rashba SOI or Bychkov-Rashba SOI.

In a mathematical description, the total electric field is included as a perturbation in the Löwdin partitioning after inserting the potential term $\mathrm{e}\boldsymbol{E} \cdot \boldsymbol{r}$ in Eq. (2.15). $\boldsymbol{E}$ is taken into account up to linear order in the resulting contributions to the conduction band Hamiltonian [53],

$$H_{\mathrm{SIA}}^{\mathrm{bulk,6c6c}} = r_{41}^{\mathrm{6c6c}} \boldsymbol{\sigma} \cdot \boldsymbol{k} \times \boldsymbol{E}, \tag{2.23}$$

and to the valence band states,

$$\begin{aligned} H_{\mathrm{SIA}}^{,\mathrm{bulk8v8v}} = & r_{41}^{8v8v} \left[\left(k_y E_z - k_z E_y \right) J_x + \mathrm{c.p.} \right] \\ & + r_{42}^{8v8v} \left[\left(k_y E_z - k_z E_y \right) J_x^3 + \mathrm{c.p.} \right] \\ & + r_{51}^{8v8v} \left[E_x \left\{ J_y, J_z \right\} + \mathrm{c.p.} \right] \\ & + r_{52}^{8v8v} \left[\left(k_y E_z + k_z E_y \right) \left\{ J_x, J_y^2 - J_z^2 \right\} + \mathrm{c.p.} \right] . \end{aligned} \tag{2.24}$$

A summary of above mentioned parameters for prominent materials is included in Table 6.6 of Ref. [53]. The numerical values of the Rashba coefficients $\left\{ r_{ij}^{8v8v} \right\}$ suggest that apart from the term proportional to r_{41}^{8v8v} other contributions for typical samples can be neglected [45].

Furthermore, we will restrict ourselves to situations where there is no inplane potential asymmetry, which results in an electric field oriented along growth direction, here defined by $\mathbf{E} = E_z\hat{\mathbf{z}}$. Asymmetric charge distribution in the growth direction of a heterostructure typically gives rise to such an electric field [53].

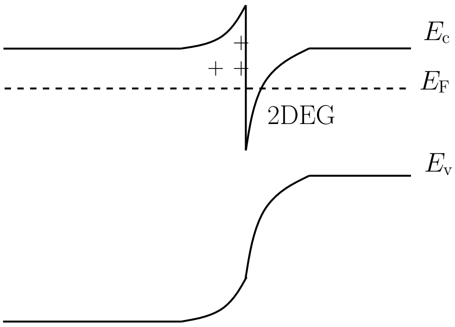

Figure 2.2: (2DEG in a heterostructure) Formation of a 2DEG at a heterostructure interface, as shown in Ref. [52] for n-AlGaAs (left) and intrinsic GaAs (right). The homogeneous Fermi energy along growth direction, indicated by the dashed line, is a consequence of charge redistribution. Conduction and valence band levels are indicated by the labels E_c and E_v respectively. The potential drop below E_F represents a confinement. This reduces the dimensionality of the problem.

2.8 Quasi two-dimensional systems

Heterostructures of semiconductor materials with different ionization energies can be used to generate quasi-two-dimensional conducting layers at the interface [52]. Depending on the experimental details, the carriers responsible for charge transport either consist of electrons or holes - and are therefore denoted two-dimensional electron gases (2DEG) or two-dimensional hole gases (2DHG) respectively.

An GaAs-AlGaAs interface is a prominent example of how a 2DEG can be realized [52]. The chemical potential, i.e. the energy change upon removal of a single electron, of n-doped AlGaAs is larger than in intrinsic GaAs. In contact, carriers are exchanged until this difference is compensated [52]. The equilibrium carrier distribution however locally induces dip in the conduction band energy, with respect to which a Fermi energy E_F can be established as shown in Fig. 2.2. As a consequence, the states close to E_F are subject to a confining potential $U(z)$, which localizes the electrons in a small range on the [001] crystallographic axis, while in the other two directions no confining potential is present [52]. Inserting a product ansatz for the electronic wave function $\Psi(\boldsymbol{r}, E_\mathrm{F}) = \phi(x,y)Z(z)$ in the effective mass description (2.12) of this problem, one obtains a discrete set of states $Z_n(z)$ with quantized sub-band energies E_n.

If only the first sub-band is below E_F, this represents a 2DEG, if there is support for more than one sub-band, but n still small, we speak of a quasi-2DEG. If a large number of states are below E_F, we have a good approximation of a three-dimensional system.

The picture for holes is analogous, up to the fact that the corresponding energies are negative, due to a different sign of the charge. In the given example the confining potential is approximately of triangular shape, for which $Z_n(z)$ are given by Airy functions [65]. It is however also possible to create harmonic or quantum well-like confinements [53]. In a perfect 2DEG, the individual shape of the confining potential hence seems to be of minor importance. However, the symmetry of the device structure can have a drastic influence on spin relaxation, since it enters the Rashba SOI [33].

Experiments in $\mathrm{InAlAs/In}_x\mathrm{Ga}_{1-x}\mathrm{As/InAlAs}$ heterostructures have shown, that with increasing structural symmetry, SOI is reduced [33]. Tuning Rashba SOI experimentally is a delicate problem. Plainly speaking, the asymmetry of the potential can be increased upon biasing with an external gate voltage. The bias however not only changes the electric field in the quantum well directly, but also indirectly by carrier redistribution. In addition, it changes the carrier density or, in other words, the Fermi energy within the heterostructure. These intertwined effects make it difficult to predetermine the magnitude of Rashba SOI. Nowadays, a variety of methods exists to quantify the SOI, allowing for control experiments. These methods can be categorized in optical and transport measurements. Optical techniques that have been applied in this context so far include the time-resolved Faraday rotation technique [66, 39] or measurements based on the spin galvanic effect or the circular photogalvanic effect [67, 3].

Transport measurements include Hanle measurements [68], and recording universal conductance fluctuations [69] or weak antilocalization [70, 71, 72, 3] in disordered systems. In this work we focus on the latter technique as method of choice for identifying SOI in a system, since it provides the advantage of potential all-electrical device operation. Optical measurements seem problematic in the context of gated devices, which are often buried in a layered heterostructure.

In particular, in contrast to the asymmetric confining potential previously discussed, it is possible to engineer a symmetric quantum well along the [001] direction. An overview of alternative methods and state of the art techniques is given for instance in Ref. [73].

For a rigorous derivation of the effects at a confinement, one can again utilize the method of Löwdin. The basis in terms of which the Hamiltonian can be expanded, are the eigenstates of a quantum well. The zeroth order contribution of this perturbation energy is just the expectation value of the Hamiltonian with respect to the ground state wave functions in [001] direction [53].

An asymmetric quantum well, as shown in Fig. 2.2, can be realized for instance at the interface of $\mathrm{GaAs/Al}_x\mathrm{GaAs}_{1-x}$-compounds [52, 74]. A symmetric quantum well is generated by sandwiching the material containing the two-dimensional system between two materials with identical ionization energy [64] and compensating remaining voltage differences via external gate voltages. If a quantum well is of asymmetric shape, the potential drop along the quantum

well, or equivalently, the electric field associated with it, leads to Rashba-type SOI in these setups. The strength of the corresponding contribution to the spin splitting is in first order proportional to this electric field. Using specific gating it is however possible, to compensate the asymmetry and eliminate this type of SOI completely [33]. In contrast to the material-specific Dresselhaus SOI, where this type of tunability is absent, Rashba SOI allows external control and switching of the SOI, leading to groundbreaking devise proposals for spin based logic, such as the famous Datta-Das spin transistor [21].
Let us specify the resulting Hamiltonian relevant in the present context. Given a confinement in [001] direction, here parallel to the materials growth direction, an effective 2×2 Hamiltonian can be found for the conduction band. It is given by

$$\mathrm{H} = \mathrm{H}_{\mathrm{kin}} + \boldsymbol{\mu} \cdot \boldsymbol{\sigma}, \tag{2.25}$$

where $\mathrm{H}_{\mathrm{kin}}$ denotes the kinetic energy defined in Eq. (2.13) and $\boldsymbol{\mu}$ is a shorthand notation of the relevant terms coupling to the spin degree of freedom. In Eq. (2.25) these terms are accumulated in an effective Zeeman term. The structure of $\boldsymbol{\mu}$ depends on the considered material and specifics of the quantum well. Additionally, in the subsequent chapter we show that above formulation is in certain limits appropriate for the description of the valence band forming a 2DHG. In this thesis we focus on three system and carrier types, in which distinct physical phenomena can be observed, specifically:

1. Cd(Mn)Te conduction band with inhomogeneous Zeeman term, $\boldsymbol{\mu} = \boldsymbol{\mu}_{\mathrm{Z}}(\boldsymbol{r})$,
2. III-V semiconductor conduction band with $\boldsymbol{\mu} = \boldsymbol{\mu}_{\mathrm{2DEG}}(\boldsymbol{k})$,
3. III-V semiconductor valence band with $\boldsymbol{\mu} = \boldsymbol{\mu}_{\mathrm{2DHG}}(\boldsymbol{k})$.

The Zeeman interaction in Cd(Mn)Te, $\boldsymbol{\mu}_{\mathrm{Z}}$, is considered within a momentum independent effective mean-field Hamiltonian (2.14). It includes spatial structure caused by the inhomogeneous texture of an externally applied magnetic field.
The electronic SOI is given by

$$\boldsymbol{\mu}_{\mathrm{2DEG}}(\boldsymbol{k}) = \boldsymbol{\mu}^{1}_{\mathrm{2DEG}}(\boldsymbol{k}) + \boldsymbol{\mu}^{3}_{\mathrm{2DEG}}(\boldsymbol{k}), \tag{2.26}$$

where $\boldsymbol{\mu}^{1}_{\mathrm{2DEG}}$ and $\boldsymbol{\mu}^{3}_{\mathrm{2DEG}}$ denote the linear and cubic wavenumber scaling of the contribution to the spatially homogeneous SOI,

$$\boldsymbol{\mu}^{1}_{\mathrm{2DEG}} = \alpha \boldsymbol{k} \times \hat{\boldsymbol{z}} + \beta \left(k_x \hat{\boldsymbol{x}} - k_y \hat{\boldsymbol{y}} \right) \tag{2.27}$$

and

$$\boldsymbol{\mu}^{3}_{\mathrm{2DEG}} = \gamma \left(-k_x k_y^2 \hat{\boldsymbol{x}} + k_y k_x^2 \hat{\boldsymbol{y}} \right). \tag{2.28}$$

$\boldsymbol{\mu}^{1}_{\mathrm{2DEG}}$ is the shorthand notation for all relevant contributions that scale linearly in the wavenumber k. It consists of the Rashba term, indicated by the prefactor

α, and the Dresselhaus contribution, associated with the prefactor β. Consistent with the notation of Ref. [53], the Rashba coefficient is defined as

$$\alpha = r_{41}^{6c6c} E_z. \tag{2.29}$$

The Dresselhaus coefficients are given as

$$\gamma \quad = b_{41}^{6c6c} \quad \text{or} \tag{2.30}$$

$$\beta \quad = b_{41}^{6c6c} \left\langle k_z^2 \right\rangle , \tag{2.31}$$

where k_z is the momentum component in [001] direction. Within a quantum well, the latter scales inversely with the quantum well diameter. The terms linear in the momentum are separately addressed as Rashba or Dresselhaus contribution. In Fig. 2.3 a) the respective Fermi contours and effective field is shown for a purely Bychkov-Rashba type SOI, while in Fig. 2.3 b) is the respective plot for a linear Dresselhaus term.

The expressions for Bychkov-Rashba and Dresselhaus SOI are well established and widely used in the context of semiconductor spintronics research. While the experimental values of the parameters, may deviate from the microscopic dependencies given above [64], their respective structure is widely agreed upon. This is due to the fact, that apart from the constants α or β, the linear contributions to the effective spin-orbit field (2.27) can be inferred solely from group theoretic reasoning. The reason for this is, that a pseudo-tensor that couples spin and momentum in zinc blende structure with C_{2v} symmetry, has only two non-vanishing invariant irreducible components - which yield Rashba and Dresselhaus terms [67].

Expressions with a similar 2×2 matrix structure can be derived as well for hole gases. One of the major differences between the models consists of the dominance of the terms cubic in the momentum in the hole gases, while in electronic systems the latter can often be neglected. In the discussion on interference phenomena in the variety of investigated systems, we start by considering electronic systems where the cubic terms are of considerable magnitude and impact physical properties significantly. This is mainly due to the fact, that the electronic cubic Dresselhaus field is of distinctly different structure, visualized in Fig. 2.3 c).

A main motivation for the subsequent discussions is a particular parameter regime that can be established in 2DEGs with negligible cubic SOI. The regime is realized if Rashba and Dresselhaus terms are of equal magnitude and fulfill the relation $\alpha = \pm\beta$. This feature is of profound significance for the realization of spintronic applications, since it represents a mechanism that suppresses spin relaxation. We will elaborate on this point in a more detailed fashion later. As first intuitive argument one might infer this feature already from considering the respective spin-orbit field in the first Brillouin zone. The latter possesses a uniaxial orientation in the reciprocal space. The choice of the spin quantization axis along the given direction, i.e. the $-45°$ orientation, allows for the definition of good quantum numbers for the spin. As a result, even in the presence of momentum randomizing scattering processes, the spin information is conserved [25]. We show the respective field in Fig. 2.3 d) for $\alpha = +\beta$. The Fermi contours of the respective spin polarizations $\epsilon_+(\boldsymbol{k})$ (blue) and $\epsilon_-(\boldsymbol{k})$ (red), indicate, that after a basis transformation the contours $\epsilon_\uparrow(\boldsymbol{k})$ and $\epsilon_\downarrow(\boldsymbol{k})$, given by the two circles visible in Fig. 2.3 d), are related by a shift in momentum space, which describes a long lived excitation of the spin [36] corresponding to the exact SU(2) symmetry introduced by Bernevig et al. in Ref. [38].

In the presence of an increased cubic Dresselhaus contribution, the shown symmetry is no longer preserved exactly [3].

We will show in this thesis, that there is a one-to-one correspondence of this type of symmetry with experiments in hole gases in particular materials, even in the presence of non-negligible cubic SOI. In the context of identification of enhanced spin lifetimes in 2DHG based devices, our theory represents an interesting finding [4]. Mentioned theory is based on a particular model of 2DHGs, presented in the following.

2.9 Two-dimensional hole gases

In the context of numerical weak localization studies, it has been shown that naively treating a two-dimensional hole gas (2DHG) as a 2DEG with a negative inverted mass does not reflect the correct Berry phases [75]. The experimental observation of weak antilocalization and weak localization in magnetically doped (Ga,Mn)As-based hole gases [76] could also not be explained satisfactory by simplified two-dimensional models including Zeeman interaction [77].

The question which sub-bands to include in a realistic model suitable to describe a particular experimental setup depends on the considered material, the diameter of the quantum well and the Fermi energy. Analytically the weak localization correction for multiple sub-bands has been calculated within the axial approximation of the Kohn-Luttinger model [60, 78]. Based on group theoretic reasoning, in this approximation only the axially symmetric substructure of the Hamiltonian is considered [53]. Narrow quantum dots of several nm width, have typically a large sub-band splitting, which allows for projecting above model via Löwdin perturbation theory to a 2×2 subspace [45].

In the following we extend a 2×2 model that takes into account the coupling to the first light-hole sub-band. Compared to previous models [43, 44, 45, 79], we generalize beyond the axially symmetric case. This helps us uncover a spin preserving symmetry and parameter regimes associated with extended spin lifetimes based on a intuitive symmetry analysis [4]. In addition, our ap-

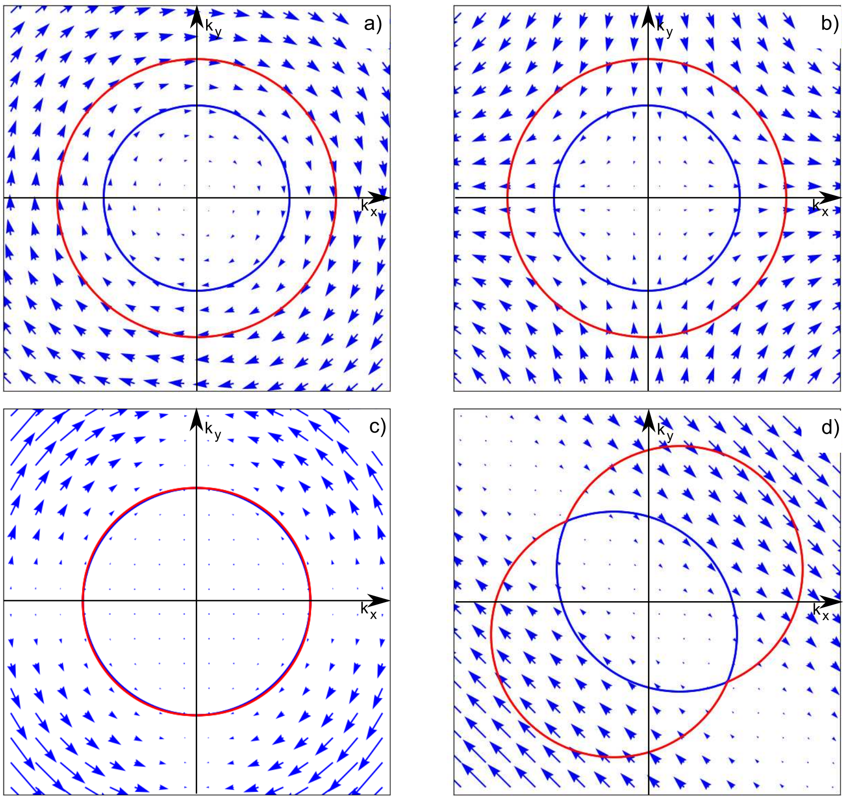

Figure 2.3: (2DEG SOI texture) Fermi contours in the first Brillouin zone in a 2DEG with Rashba SOI $\alpha\hat{\boldsymbol{k}} \times \hat{\boldsymbol{z}}$ (a), linear Dresselhaus SOI $\beta\,(k_x\hat{\boldsymbol{x}} - k_y\hat{\boldsymbol{y}})$ (b) and cubic Dresselhaus term $\boldsymbol{\mu}^3_{\mathrm{2DEG}}$ (c) for the two different spin polarizations (marked by blue and red color). In d) an example of the persistent spin helix symmetry is shown for $\alpha = \beta$, in which the spin precession axis orientation is uniform in the reciprocal space. In all plots the blue arrows indicate the momentum dependent orientation of the effective spin-orbit field $\boldsymbol{\mu}_{\mathrm{2DEG}}$.

proach allows the application of diagrammatic frameworks [80, 81] for 2DEGs in the weak disorder limit, to obtain analytical expressions for the magnetoconductance [4]. This is a considerable simplification in contrast to larger 4×4 effective Hamiltonians which have so far been treated within semi-analytical frameworks [77] or have been considered within the axial approximation [78].

Alternatively, a similar calculation could be performed for materials in which the coupling between the heavy hole (HH) ground state and its first excited state is larger than the coupling between ground state and light hole (LH) ground state. However, the latter case is of particular interest to us, since extended spin lifetimes in narrow quantum wells have been predicted by theory [82]. A density matrix based Bloch-Redfield approach focusing on phonon-HH interactions indicates the possibility of HH spin lifetimes that exceed electronic spin lifetimes [45]. This finding is a promising advance in the utilization of spin based phenomena beyond lab temperatures and motivates us to focus on narrow quantum wells, i.e. strongly two-dimensional HH-gases [45].

Furthermore, Having outlined the basic setup, we proceed with the application of Löwdin's theory to the multi-band hole-gas Hamiltonian.

We start from the Luttinger model of hole bands with heavy and light effective mass (2.15). Since we aim at describing effects due to bulk symmetry and the application of an externally controlled electric field, we include the previously introduced terms (2.22) and (2.24) respectively. Note that this treatment is appropriate, although each of these results have been obtained individually within perturbation theory, since to leading order the sequential application of Löwdin's method with respect to different parameters converges to the same result [53].

We describe states at the Fermi energy close to the valence band maximum, where the inplane momentum $k_{\|} = \sqrt{k_x^2 + k_y^2}$ is small. Therefore $k_{\|}$ will only be taken into account up to third order, i.e. $O(k_{\|}^3)$.

By summing up the contributions (2.15), (2.22) and (2.24), we arrive at the perturbation theoretical expression for the bulk Hamiltonian $H' = H^{8\mathrm{v}8\mathrm{v}} + H^{8\mathrm{v}8\mathrm{v}}_{\mathrm{BIA}} + H^{8\mathrm{v}8\mathrm{v}}_{\mathrm{SIA}}$, which has a 4×4 matrix structure. The corresponding Hilbert space is classified into heavy (HH) and light holes (LH) according to the respective angular momenta with respect to the $\hat{e}_z$-axis.

An orthogonal transformation O is applied to H'. We choose $O = P_{34}P_{24}$, where P_{ij} permutes i-th and j-th line or column, and rearrange H' such that the states corresponding to the angular momentum quantum numbers $j_z = \pm 3/2$, or heavy holes (HH), form the basis of the upper left 2×2 block, while the states with $j_z = \pm 1/2$, or light holes (LH), form the lower right 2×2 block. The remaining blocks describe the coupling between these subspaces. Hence, the result has the structure:

$$H'' = OH'O^T = \begin{array}{c} \\ j_z = +3/2 \\ j_z = -3/2 \\ j_z = +1/2 \\ j_z = -1/2 \end{array} \begin{array}{c} \begin{array}{cccc} j_z = +\frac{3}{2} & j_z = -\frac{3}{2} & j_z = +\frac{1}{2} & j_z = -\frac{1}{2} \end{array} \\ \left(\begin{array}{cccc} H'_{11} & H'_{14} & H'_{12} & H'_{13} \\ H'_{41} & H'_{44} & H'_{42} & H'_{43} \\ H'_{21} & H'_{24} & H'_{22} & H'_{23} \\ H'_{31} & H'_{34} & H'_{32} & H'_{33} \end{array} \right) \end{array} . \tag{2.32}$$

Eq. (2.32) still describes the band structure of a three dimensional bulk hole gas. Next we establish a confinement in growth direction in order to realize a 2DHG. As previously explained, an electric field $\mathbf{E} = E_z\hat{\mathbf{z}}$ is associated with the latter. $E_z\hat{\mathbf{z}}$ lifts the $k_{\|} = 0$ degeneracy of HH and LH states and introduces sub-band structure due to the confinement. For convenience we consider a confining potential sufficiently steep such that the solutions of an infinite one dimensional potential well of width W_z,

$$\sqrt{\frac{2}{W_z}}\sin\frac{n\pi z}{W_z}, \tag{2.33}$$

represent the appropriate basis in order to perform the perturbation theory.

Our aim is to model the arising physical situation within an effective 2×2 Hamiltonian, describing the highest valence band modes, or the ground state of the quantum well in $\hat{e}_z$-direction.

Contrasting to the electronic case, where only one spin split sub-band has to be considered, one has to choose carefully the appropriate subspace as zeroth order term of Löwdin's expansion. The states that correspond to the minimal kinetic energy, are of HH structure in typical semiconductor materials, while it depends on the considered material, which type of states are the energetically adjacent to the latter [53].

In order to select the appropriate sub-bands for the 2×2 model, it is helpful to quantify the confinement induced splitting energies of the individual bands via the approximations for the effective masses in $\hat{z}$-direction from Ref. [53],

$$\frac{m_0}{m_z^{\mathrm{HH}}} = \gamma_1 - 2\tilde{\gamma} \quad \text{and} \quad \frac{m_0}{m_z^{\mathrm{LH}}} = \gamma_1 + 2\tilde{\gamma}, \tag{2.34}$$

inserted into the energy of the n-th sub-band in quantum well as a rough estimate,

$$E_n(\mathrm{LH}) = -\frac{\hbar^2\pi^2\mathrm{n}^2}{2\mathrm{m}_\mathrm{z}^{\mathrm{LH}}\mathrm{W}_\mathrm{z}^2} \quad \text{and} \quad \mathrm{E}_\mathrm{n}(\mathrm{HH}) = -\frac{\hbar^2\pi^2\mathrm{n}^2}{2\mathrm{m}_\mathrm{z}^{\mathrm{HH}}\mathrm{W}_\mathrm{z}^2}, \tag{2.35}$$

with the quantum well depth W_z, the bare electron mass m_0 and the effective growth direction dependent Luttinger parameter

$$\begin{aligned} \tilde{\gamma} &= (1-\zeta)\,\gamma_2 + \zeta\gamma_3, \\ \zeta &= \sin^2\theta\left\{3 - \frac{3}{8}\sin^2\theta\,[7+\cos(4\phi)]\right\}. \end{aligned} \tag{2.36}$$

Here, the angles θ and ϕ indicate the growth direction of the material. We will restrict our considerations to the growth direction [001], for which one obtains $\tilde{\gamma} = \gamma_2$. Now the material dependent Luttinger parameters γ_1 and γ_2 determine the structure of the states of the lowest confinement quantum numbers n. For different known values we obtain Table 2.1, with $E_0 = \hbar^2\pi^2/(2m_0\mathrm{nm}^2) \approx 752\,\mathrm{meV}$ and $\tilde{E}_n(\mathrm{LH/HH}) = E_n(\mathrm{LH/HH})W_z^2\mathrm{nm}^{-2}$.

Note that the ground state of the HH states is always the lowest energy state that has to be considered, while depending on the material, the next lowest level, marked by blue colors, may be of HH or LH nature. Furthermore, although the first excited LH state can be considered sufficiently remote for narrow quantum wells, the coupling to the LH ground state may still be of importance, as second next to lowest level (green color) as well as next to lowest level.

Table 2.1: Material parameters from Ref. [53] and estimation of relative positions of heavy hole (HH) and light hole (LH) bands in dimensionless values for an infinitely deep rectangular quantum well in growth direction.

	γ_1	γ_2	γ_3	$\tilde{E}_1(\mathrm{HH})$	$\tilde{E}_2(\mathrm{HH})$	$\tilde{E}_1(\mathrm{LH})$
GaAs	6.85	2.10	2.90	-2.65	-10.6	-11.05
AlAs	3.25	0.65	1.21	-1.95	-7.8	-4.552
InSb	37.1	16.5	17.7	-4.1	-16.4	-70.1
InAs	20.4	8.30	9.10	-3.8	-15.2	-37
AlSb	4.15	1.01	1.71	-2.13	-8.52	-6.17
$\mathrm{Ga_{0.47}In_{0.53}As}$	11.97	4.36	5.15	-3.25	-13	-20.69
$\mathrm{Al_{0.47}In_{0.53}As}$	6.17	1.62	2.31	-2.93	-11.72	-9.41
InP	4.95	1.65	2.35	-1.65	-6.6	-8.25
CdTe	5.30	1.70	2.00	-1.9	-7.6	-8.7
ZnSe	4.30	1.14	1.84	-2.02	-8.08	-6.58

These results only represent a rough estimate, as can be seen from the fact that the band ordering of GaAs is not pictured correctly and in accordance with the numerical results shown in Ref. [53]. A harmonic confinement has been used for the band structure calculation shown in [53] which explains this discrepancy. Restricting ourselves to the hard wall confinement, we may however safely approximate AlAs,ZnSe, AlSb and $\mathrm{Al_{0.47}In_{0.53}As}$ by a 2×2 model in the HH-subspace, where only the coupling to the ground state of the LH-bands is taken into account.

The splitting between heavy and light hole states $\Delta_{\mathrm{HL}} = \frac{2\pi^2\hbar^2\gamma_2}{m_0 W_z^2}$ can be read of from Eq. (2.34) directly and hence enters within Löwdin perturbation theory to describe the HH subspace in 2 dimensions, by an effective 2×2 Hamiltonian for a small confinement depth W_z, according to

$$\begin{aligned} H_{\mathrm{2DHG;mm'}} \simeq & H_{0;mm'} + \frac{1}{2}\sum_{s=3,4(\in\mathrm{LH})} H''_{ms}H''_{sm'}\left(\frac{1}{E^0_m - E^0_s} + \frac{1}{E^0_{m'} - E^0_s}\right) \\ = & H_{0;mm'} + \frac{1}{\Delta_{\mathrm{HL}}}\sum_{s=3,4(\in\mathrm{LH})} H''_{ms}H''_{sm'}, \end{aligned} \tag{2.37}$$

where $m, m' \in 1, 2$ are the indexes corresponding to the HH-subspace of H'', and the zero-order term of the expansion is given by

$$H_0 = \begin{pmatrix} H'_{11} & H'_{14} \\ H'_{41} & H'_{44} \end{pmatrix}. \tag{2.38}$$

We furthermore consider only the lowest sub-band due to the confinement, which means that, according to Löwdin's theory, we substitute the powers of k_z

by their respective expectation values, meaning $\langle k_z \rangle = 0$ and $\left\langle k_z^2 \right\rangle = \pi^2/W_z^2$. We find the effective Hamiltonian,

$$H_{\mathrm{2DHG}} \simeq \frac{\hbar^2 {\mathbf{k}_\parallel}^{\mathbf{2}}}{2m_{\mathrm{eff}}} + V_z + \boldsymbol{\mu}_{\mathrm{2DHG}} \cdot \boldsymbol{\sigma}, \tag{2.39}$$

in which $\boldsymbol{\sigma}$ refers to the subspace spanned by the HH states of spin angular momenta $\pm 3\hbar/2$. We find the effective spin-orbit field describing heavy holes,

$$\begin{aligned} \boldsymbol{\mu}_{\mathrm{2DHG}} &= \beta_{\mathrm{HH}} \boldsymbol{k} \\ &+ \lambda_{\mathrm{D}} \left\{ -\bar{\gamma} k_{\mathrm{F}}^2 \boldsymbol{k} + \delta [k_x^3 \hat{\boldsymbol{x}} + k_y^3 \hat{\boldsymbol{y}} - 3k_x k_y (k_y \hat{\boldsymbol{x}} + k_x \hat{\boldsymbol{y}})] \right\} \\ &+ \lambda_{\mathrm{R}} \left\{ \delta k_{\mathrm{F}}^2 (k_y \hat{\boldsymbol{x}} + k_x \hat{\boldsymbol{y}}) + \bar{\gamma} [-k_y^3 \hat{\boldsymbol{x}} - k_x^3 \hat{\boldsymbol{y}} + 3k_x k_y \boldsymbol{k}] \right\}, \end{aligned} \tag{2.40}$$

with the intrinsic Dresselhaus parameters

$$\beta_{\mathrm{HH}} = -\sqrt{3} C_k \left(\frac{1}{2} - \frac{2\hbar^2 \left\langle k_z^2 \right\rangle \gamma_3}{m_0 \Delta_{\mathrm{HL}}} \right), \tag{2.41}$$

$$\lambda_{\mathrm{D}} = \frac{\sqrt{3}\hbar^2}{2m_0 \Delta_{\mathrm{HL}}} \left[C_k + \sqrt{3} b_{41}^{8v8v} \left\langle k_z^2 \right\rangle \right], \tag{2.42}$$

the structural Bychkov-Rashba parameter,

$$\lambda_{\mathrm{R}} = \frac{3\hbar^2}{2m_0 \Delta_{\mathrm{HL}}} \langle E_z \rangle \, r_{41}^{8v8v}, \tag{2.43}$$

which depends on the electrical field $\langle E_z \rangle$, and the Luttinger parameters $\bar{\gamma} = (\gamma_3 + \gamma_2)/2$ and $\delta = (\gamma_3 - \gamma_2)/2$ as in Ref. [83]. The given notation is particularly transparent in revealing which parameters correspond to axial symmetry, established by setting $\delta = 0$, or an asymmetric situation at $\bar{\gamma} = 0$. In Fig. 2.4 we show sketches of the respective spin-orbit fields and Fermi contours, attributed to either $\delta = 0, \bar{\gamma} \neq 0$ in sub-figure a) and $\delta \neq 0, \bar{\gamma} = 0$ sub-figure b), which is considered to be of rather artificial nature. The field resulting from the more realistic superposition of both contributions of different magnitude is depicted in Fig. 2.4 c). A special symmetry arises for equal and finite values of δ and $\bar{\gamma}$, which possesses a close similarity with the persistent spin helix type symmetry of electronic systems with equal Rashba and Dresselhaus contributions to the SOI [25]. As in the electronic case, this symmetry protects the spin against relaxation, due to the presence of a fixed spin precession axis orientation in the reciprocal space. The latter situation is illustrated in Fig. 2.4 d).

The interplay of both axially symmetric and antisymmetric contributions to the Hamiltonian is crucial for the realization of extended spin lifetimes in 2DHGs [4]. This is one of the main results of our study on weak localization in 2DHGs [4]. In addition our model allows for the description of a broader range of materials and includes anisotropies that are important, for instance, in the plasmon spectra of HH systems [84].

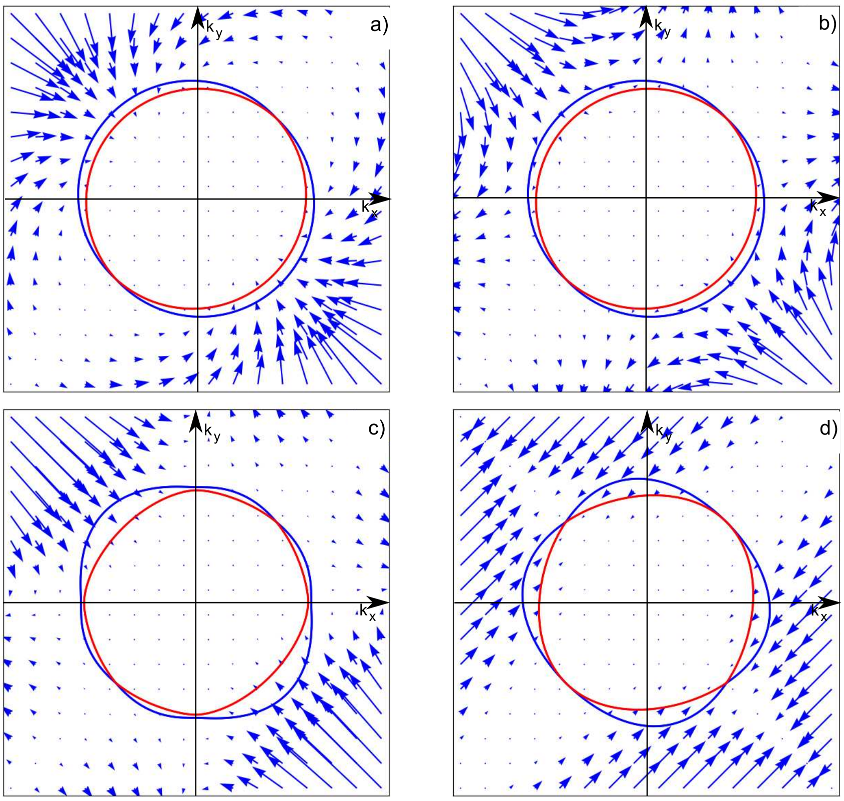

Figure 2.4: (2DHG SOI texture) Fermi contours (blue and red contour for the different spin species) and effective spin-orbit field of our 2DHG model (2.40) within the spherical approximation $\delta = 0, \bar{\gamma} = 0.5$ (a), the regime $\delta = 0.5, \bar{\gamma} = 0$ (b), an intermediate case $\delta = 0.4, \bar{\gamma} = 0.6$ (c) and a persistent spin helix type symmetry with uniaxial spin precession axis at $-\delta = \bar{\gamma} = 0.5$ (d). In all plots the blue arrows indicate the momentum dependent orientation of the effective spin-orbit field $\boldsymbol{\mu}_{\mathrm{2DHG}}$.

For completeness, Löwdin's theory results also in corrections of the effective mass and the potential,

$$m_{\mathrm{eff}}^{-1} = \frac{\gamma_1+\gamma_2}{m_0} + \frac{C_k^2}{2\hbar^2\Delta_{\mathrm{HL}}} + \frac{\sqrt{3}b_{41}^{8v8v}C_k\left\langle k_z^2\right\rangle}{\hbar^2\Delta_{\mathrm{HL}}} + \frac{6\hbar^2\left\langle k_z^2\right\rangle\gamma_3^2}{m_0^2\Delta_{\mathrm{HL}}}, \tag{2.44}$$

$$\text{and} \quad V_z = -\frac{\hbar^2\left\langle k_z^2\right\rangle}{2m_0}\left(\gamma_1 - 2\gamma_2\right) + \frac{C_k^2\left\langle k_z^2\right\rangle}{\Delta_{\mathrm{HL}}}. \tag{2.45}$$

The effect on the first term entering into m_{eff}^{-1}, which is the effective mass of the isolated HH-band, will be ignored in the following discussion. The shift of the potential is compensated by a shift of the Fermi energy.

Our approach is very similar to the technique used by Winkler et al. [44, 79] or Bulaev and Loss [45]. We obtain the result of Ref. [45], when we specify our expression (2.40) to the axially symmetric case, upon setting $\delta = 0$ and neglecting terms proportional to C_k.

The Hamiltonian in Ref. [45] is an extension of Winkler's earlier result of the Rashba term for hole gases, shown in Ref. [44] [2].

The Hamiltonian of a hole gas with Rashba and Dresselhaus SOI within axial approximation is given by [45, 44]

$$H_{\mathrm{BL}} = \imath\alpha_{\mathrm{R}}(k_-^3\sigma_+ - k_+^3\sigma_-) - \alpha_{\mathrm{D}}(k_-k_+k_-\sigma_+ + k_+k_-k_+\sigma_-), \tag{2.46}$$

which can be recast, using the definition of the shorthand notations $k_\pm = k_x \pm \imath k_y$ and $\sigma_\pm = \frac{1}{2}(\sigma_x \pm \imath\sigma_y)$, into

$$\begin{aligned} H_{\mathrm{BL}} &= -\alpha_{\mathrm{D}}\left(k_x^3\sigma_x + k_y^3\sigma_y\right) + 3\alpha_{\mathrm{R}}\left(k_x^2k_y\sigma_x + k_xk_y^2\sigma_y\right) \\ &\quad - \alpha_{\mathrm{D}}\left(k_xk_y^2\sigma_x + k_x^2k_y\sigma_y\right) - \alpha_{\mathrm{R}}\left(k_y^3\sigma_x + k_x^3\sigma_y\right). \end{aligned} \tag{2.47}$$

A comparison of the coefficients

$$\alpha_{\mathrm{R}} = \frac{1}{2m_0\Delta_{\mathrm{HL}}}\left[3\left\langle E_z\right\rangle r_{41}^{8v8v}\gamma_2\right] \quad \text{and} \tag{2.48}$$

$$\alpha_{\mathrm{D}} = -\frac{1}{2m_0\Delta_{\mathrm{HL}}}\left[3\left\langle k_z^2\right\rangle b_{41}^{8v8v}\gamma_2\right], \tag{2.49}$$

with our result (2.40) yields perfect agreement in the parameter regime that establishes axial symmetry.

The material properties presented in Table 2.1, however show no materials that fulfill the criterion $\gamma_3 \approx \gamma_2$ exactly. This motivates us to work with Eq. (2.40) as generalization of the model described by Eq. (2.46).

In Ref. [79] above model has been extended to include a k-linear Dresselhaus term. The expression is however also based on the axial approximation of the Hamiltonian.

For further analysis the terms proportional to the small parameter C_k are neglected in Eqs. (2.41) and (2.42) since, for a narrow confinement, the physics are dominated by the terms proportional to $b_{41}^{8v8v}\left\langle k_z^2\right\rangle$ in realistic materials, as shown in Table 6.3 in Ref. [53]. Furthermore, the linear Dresselhaus term (2.41) effectively rescales the axially symmetric part of the cubic Dresselhaus contribution.

---

[2] In Ref. [44] the Rashba term was derived to explain an anomalous dependence of the Rashba coefficient on externally applied electric fields in two-dimensional hole gases. In the discussed systems, the Rashba spin splitting counter-intuitively increases upon decreasing external electric fields. The effect is attributed to the inverse dependence of the Rashba coefficient on the sub-band separation, which is more strongly influenced by an electric field in two-dimensional hole gases, than the respective coefficient describing valence band states [44].

Chapter 3

Theory of mesoscopic spin and charge transport

In the present chapter we describe the methods we use to obtain spin and charge transport properties of a given system. The formalisms with which we approach transport provide a valid description are current measurements in two-dimensional mesoscopic heterostructures.

In the context of electronic transport, our model specifics are to a large portion motivated by experimental studies discussed in Refs. [1, 3]. First, we perform exact numerical calculations based on a finite difference scheme, which is briefly introduced here. Additionally, we establish a qualitative understanding of the observed phenomena on fundamental system properties by means of an illustrative semiclassical analytical description. The assumptions on which both of the mentioned approaches are based, are presented in the following.

3.1 Transport in mesoscopic samples

In Fig. 3.1 we sketch a mesoscopic system, in which typically relations

$$\lambda_{\mathrm{F}} \ll L \ll L_{\phi}, \tag{3.1}$$

are fulfilled [52]. The parameters entering Eq. (3.1) are the system size L, the phase coherence length scale L_{ϕ}, and the Fermi wavelength λ_{F}. $\lambda_{\mathrm{F}} = \frac{2\pi}{k_{\mathrm{F}}}$ is the wavelength associated with electrons or holes at the Fermi surface.

L_{ϕ} is the distance over which phase information is conserved. This length scale is typically determined by the temperature Θ, since electron-electron or electron-phonon scattering induce phase relaxation at a value of Θ that deviates from 0 [85]. Thermal broadening attributed to temperatures significantly

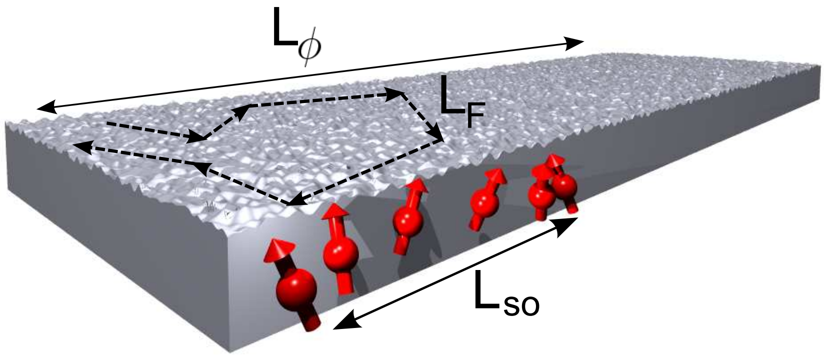

Figure 3.1: (disordered conductor) Schematic potential landscape of a disordered mesoscopic scattering region in which phase coherence length L_ϕ, elastic mean free path L_F and spin precession length L_so obey the relation $L_\phi \gg L_\mathrm{so}, L_\mathrm{F}$.

larger than 1 K typically leads to smearing out of quantum mechanical relevant details.

The term "mesoscopic" suggests the focus on systems within an intermediate regime of length scales. Although a typical mesoscopic system can be much larger than an atom, the laws of quantum mechanics are reflected in the systems properties [52]. This feature is contained in the relation $\lambda_\mathrm{F} \ll L$.

The conservation of phase information or phase coherence sets the stage for quantum mechanical interference phenomena. Well known examples of coherence effects include universal conductance fluctuations [86, 87], strong localization [88], weak localization, for which interference of backscattered paths such as the example shown in Fig. 3.1 is responsible [89, 90]. If spin of the transported particles, whose precession is described by the length scale L_so in Fig. 3.1, is subject to randomization, backscattered paths give rise to weak anti-localization [91].

Mentioned phenomena are typically connected to the presence of disorder in a mesoscopic device[1]. In particular weak (anti-)localization will be subject to a more detailed discussion in the remaining text.

The conductance of a disordered sample is determined by charge carriers at the Fermi surface, that evolve diffusively [52]. If scattering processes are sep-

---

[1] A variety of mentioned phenomena has been summarized under the context "quantum-interference at defects (QIAD)" in a review of Bergmann [90]. For completeness, although weak localization effects or conductance fluctuations are widely discussed phenomena in disordered conductors, they occur in ballistic structures as well. Particularly in structures that have have classically chaotic analogues, the mentioned effects are of universal nature and can accurately be described within semiclassical frameworks or random matrix theory [92, 93, 94, 95].

arated by the timescale τ, the mean free path L_{F} which particles with Fermi velocity v_{F} travel, is thus given by

$$L_{\mathrm{F}} = v_{\mathrm{F}}\tau. \tag{3.2}$$

The corresponding diffusion coefficient D in two dimensions is estimated as

$$D = \frac{v_{\mathrm{F}}^2\tau}{2}, \tag{3.3}$$

assuming isotropic scattering [96].

In many systems which are larger than phase coherence length, $L > L_\phi$, mesoscopic phenomena are observable as well. This point is relevant to the experimental detectability of semiconductor based quantum interference effects, since typical measurement setups are performed in multi-terminal geometries of several $\mu\mathrm{m}$ spatial extend, such as a Hall-bar setup [3, 1]. In these cases the length scale L_T replaces the absolute system size L in Eq. (3.1) in the respective measurement. The Thouless length L_T is given by the distance a diffusively propagating particle traverses before loosing its phase coherence [52, 97]. The whole sample can hence be thought of as an incoherent decomposition of identical subsystems with length L_T, in each of which interference phenomena appear independently [85].

To build a realistic model, the presence of lattice imperfections and impurities should be accounted for, since they can not be completely avoided in an experimental setup [52]. Consequently, also in the idealistic limit $\Theta = 0$, we expect a limited value of L_{F}. This quantity is determined by elastic scattering processes at a disorder potential, to which the electronic wavefunction is subject.

To obtain universal results and to model small temperature fluctuations of transport experiments, the observables that we calculate are averaged over a large number of disorder configurations [52].

Transport properties depend on the ratio L/L_{F}. Considering a given system with otherwise constant parameters, say we start from $L_{\mathrm{F}} = L$ and decrease L_{F} relative to L, we observe a transition from ballistic to diffusive transport. If we decrease L_{F} further, we are able to suppress diffusive transport and obtain insulating behavior. Anderson showed, that in this case the average carrier wavefunction is sharply localized [88]. The conductance G scales accordingly [52], like

$$G(L/L_{\mathrm{F}}) \sim \exp\left(-L/L_{\mathrm{F}}\right). \tag{3.4}$$

The described behavior is observed if the condition $k_{\mathrm{F}}L_{\mathrm{F}} \ll 1$ holds [88].

Note that, we do not focus on the Anderson regime, but the weak scattering limit, associated for which the Yoffe-Regel criterion $k_{\mathrm{F}}L_{\mathrm{F}} \gg 1$ holds [98]. The latter is also known as metallic regime [99]. Fulfilling the given criterion allows for comparison of our numerical results with diagrammatic results on localization phenomena [4, 89, 91, 42, 80, 81, 100, 101].

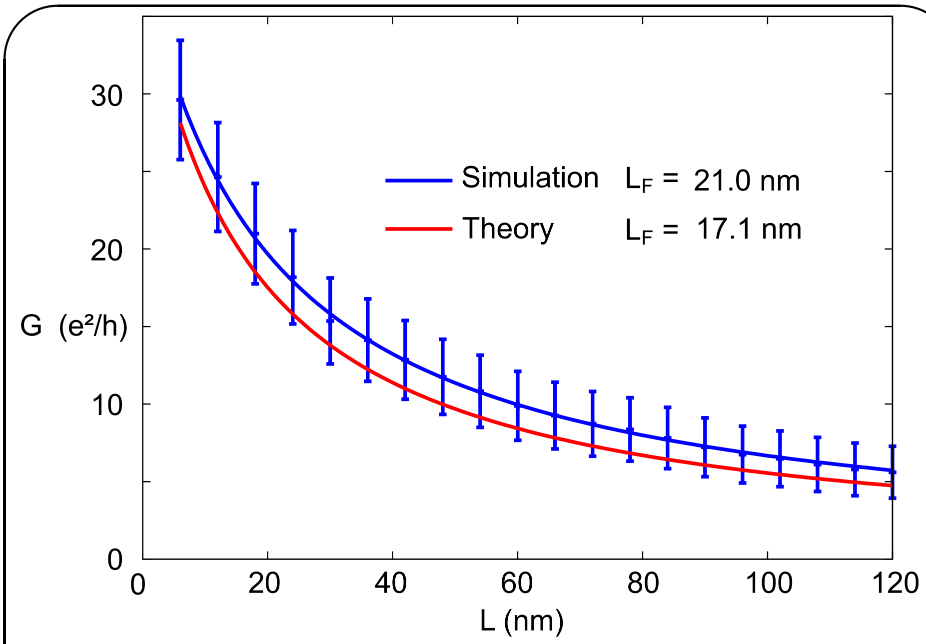

Figure 3.2: (length dependence of the conductance) Average conductance G of a 2DEG with Anderson disorder versus the system length. The estimate of the mean free path from Fermi's golden rule (red line) is predicting the numerically observed behavior (blue line) well. The considered system has a width of 80 nm, is operated at a Fermi energy of 19.5 meV and a finite magnetic field of 2 T to suppress conductance corrections. To obtain this plot we average over 100 disorder configurations. The theoretical value of the mean free path $L_\mathrm{F} = 17.1\,\mathrm{nm}$ is extracted from a single parameter fit from Eq. (3.5).

For the moment ignoring interference effects, we consider a regime where the conductance scales according to

$$G(L/L_\mathrm{F}) \sim (1 + L/L_\mathrm{F})^{-1}\,. \tag{3.5}$$

The numerically obtained transport data shown in Fig. 3.2, illustrate the given behavior for a weakly disordered sample. Mentioned scaling behavior is also used as validation of our numerical models presented later.

We include disorder in the respective Hamiltonian (2.25) by extending it by a disorder potential term U_D, to

$$\mathrm{H} = \mathrm{H}_\mathrm{kin} + \boldsymbol{\mu}\cdot\boldsymbol{\sigma} + U_\mathrm{D}. \tag{3.6}$$

For theoretical purposes, two-dimensional disorder is modeled by a locally changing random potential $U_\mathrm{D}(\boldsymbol{r})$. In practice two disorder models are widely used, Gaussian and Anderson type disorder. These two disorder classes fulfill upon average over disorder configurations $\langle ... \rangle_D$,

$$\langle U_\mathrm{D}(\boldsymbol{r})\rangle_\mathrm{D} = 0 \quad \text{and} \tag{3.7}$$

$$\langle U_\mathrm{D}(\boldsymbol{r})U_\mathrm{D}(\boldsymbol{r}')\rangle_\mathrm{D} = \sigma_\epsilon^2 \delta_\epsilon(\boldsymbol{r}' - \boldsymbol{r}), \tag{3.8}$$

where $\delta_\epsilon(\boldsymbol{x})$ becomes the delta function $\delta(\boldsymbol{x})$ in the limit $\epsilon \to 0$. This limit represents Anderson disorder in the strict sense [88]. Gaussian disorder is characterized by a superposition of randomly distributed Gaussians with uniformly distributed height and standard deviation and a finite Gaussian correlation. In the limit $\epsilon \to 0$ the peak height gets infinitely large and σ zero, so that one recovers an exact representation of Anderson disorder [102].

We implement Ando's disorder model on the finite differences grid in our numerical calculations [103]. The disorder potential in each unit cell is taken randomly from the interval $[+U_0/2, -U_0/2]$, following a uniform distribution. Under the given conditions, in a simple 2DEG the dependence

$$L_\mathrm{F} = 48 \frac{1}{a^2} \frac{E_\mathrm{F}^2}{U_0^2 k_\mathrm{F}^3}, \tag{3.9}$$

between disorder strength U_0, Fermi Energy $E_\mathrm{F} = \frac{\hbar^2 k_\mathrm{F}^2}{2m^\star}$, mean free path L_F and a cross section of each potential box of a^2 represents a reasonable estimate. This is demonstrated in Fig. 3.2, in which the typical numerically obtained transmission values are compared to the theoretical prediction. They obey the scaling (3.5), which can be specified to a concrete number of open channels $N = 38$, by the expression $G/(e^2/h) = N(1 + L/L_F)^{-1}$ [52].

Note that the validity of Eq. (3.6) for any of the previously mentioned material and carrier types relies on the assumption that $\mu = |\boldsymbol{\mu}|$ is a small contribution compared to the effective mass kinetic energy $\langle \boldsymbol{k} | \mathrm{H}_\mathrm{kin} | \boldsymbol{k} \rangle = \mathrm{E}_\mathrm{kin} \approx E_\mathrm{F}$, which applies to the experiments and models considered in the present text [1, 2, 3, 4]. In diluted systems with giant Zeeman interaction [1] the ratio of Zeeman splitting and E_F is of the order of 1/10, which is still considered a small quantity in Chap. 4.

In the following we introduce the Green's function, which establishes a connection between our model and a systems transmission properties.

3.2 Green's function

Our focus on mesoscopic systems justifies the application of standard quantum mechanical concepts, such as the Green's function.

The Green's function is based on a quantum mechanical operator $\hat{\mathrm{G}}$ that fulfills

$$\lim_{\eta \to 0} (E - \hat{\mathrm{H}} + i\eta)\hat{\mathrm{G}} = \mathbb{1}. \tag{3.10}$$

for a Hamiltonian $\hat{\mathrm{H}}$ and the identity operator $\mathbb{1}$ [52]. Particular representations of Green's functions are the retarded (G^R) or advanced Green's function (G^A), which one obtains upon setting $\eta \geq 0$ or $\eta \leq 0$ respectively. The position space matrix element

$$\mathrm{G}^{\mathrm{R}}(\mathbf{q}, \mathbf{q}', E) = \langle \mathbf{q} | \hat{\mathrm{G}}^{\mathrm{R}}(E) | \mathbf{q}' \rangle \tag{3.11}$$

is relevant for the Landauer-Büttiker approach that underlies several numerical and analytical aspects of this work. It describes a complex amplitude which relates a position $\mathbf{q}$ to a position $\mathbf{q}'$ for a fixed energy E. The subject of the momentum space representation $\mathrm{G}^{\mathrm{R}}(\mathbf{k}, \mathbf{k}', E)$ will only be briefly touched in the present thesis, although it is essential to the standard perturbative approaches for the transport properties of disordered conductors, that are derived from the Kubo formula [104, 52].

Like H, combined with the knowledge on the boundary conditions, the object $\hat{\mathrm{G}}^{\mathrm{R}}$ supplies all information on a quantum mechanical system to calculate observables that are of relevance to our discussions.

This description is exact for zero temperature. Particle transport, which is a non-equilibrium phenomenon, can be well described within the linear response picture, which essentially holds for small temperatures and small potential differences. This statement will be clarified in the following paragraph. We continue our discussion by showing exact relations between transport properties and the Green's function.

3.3 Landauer-Büttiker theory

Transport of noninteracting fermions can be considered as particle flux between spatially separated reservoirs with different electrochemical potentials [105]. A bias V is usually obtained by gating the sample in longitudinal direction. The connection of conducting region and the reservoirs is modeled by ideal leads. Ideal in this context means, that the leads are considered as ballistic quantum point contacts [106], supporting a discrete number of non-evanescent modes. The reservoirs are in quasi-equilibrium [52]. We assume that each reservoir contains a large number of particles. Consequently their electrochemical potential remains roughly constant despite a finite particle flux [107]. Ideal also means that scattering at the interface between lead and reservoir is considered negligible [105]. Note that our discussion discussion holds at low temperatures and is valid in the linear response regime, associated with small voltage drops over the conducting region [52]. Within linear response, charge current I is given by the product of the conductance G and V,

$$I = G \cdot V. \tag{3.12}$$

Based on this picture, the DC conductance of a device with an arbitrary number channels has been presented in the work of Büttiker *et al.* [107]. In the present work we restrict ourselves to two-terminal setups. The corresponding relation of G and transmission matrices t is given by [107]:

$$G = \frac{e^2}{h} T = \frac{e^2}{h} Tr(tt^\dagger) = \frac{e^2}{h} \sum_{n,m,\sigma,\sigma'} \left| t_{nm}^{\sigma\sigma'} \right|^2 . \tag{3.13}$$

We calculate the conductance in the zero temperature limit. Temperature dependence can be included in the Landauer picture via an average over the derivative of the Fermi distribution [20]. At $\Theta \to 0$ the distribution assumes the structure of a Dirac δ-function, which is peaked at the Fermi energy E_{F}. Hence quantities that enter the trace on the right hand side of (3.13) are evaluated on the Fermi surface.

The real quantity T is called transmission function. When we consider only a classical problem, T is given by the sum of the transmission probabilities for all considered channels. However the influence of quantum mechanics causes T to deviate from classical expectations. The conductance G of a d-dimensional sample with linear dimension a is related to the conductivity σ by $G = a^{d-2}\sigma$. Specifically, for a two-dimensional conductor of width W and length L holds $G = (W/L)\sigma$ [108]. Experimentally the conductance is accessible by measuring voltage drops and using the Landauer framework that connects measured resistances with G [52].

The constant prefactor in (3.13) is half of the universal conductance quantum [52] $2\frac{e^2}{h} = (12.9\ k\Omega)^{-1}$. Integer multiples of the latter are reflected in the conductance quantization within the quantum hall effect (QHE) [109] or in a ballistic quantum point contact (QPC) [106]. The factor 2 is due to spin, when considered degenerate. We will discuss systems, where a splitting between different spin orientations can be achieved. Therefore we normalize the conductance by $\frac{e^2}{h}$.

We establish the dependence of T on the sample properties within the scattering theoretic framework of Fisher and Lee [110]. In their work Fisher and Lee consider semi-infinite leads and use Kubo's formula [104] in the evaluation of the transmission matrices t entering Eq. (3.13). The system specifics then enter t via the Green's function [110]. Below we show the resulting relation, generalized to the spin dependent case:

$$\begin{aligned} t_{n,m}^{\sigma,\sigma'} = -i\hbar\sqrt{v_{n,\sigma} v_{m,\sigma'}} \int_0^{D'} \mathrm{d}y' \int_0^{D} \mathrm{d}y \phi_n^\star(y) \mathrm{G}^{\sigma\sigma'}(L, y'; 0, y; E_F) \phi_m(y') \\ \Theta(-|\mathrm{Im}(v_{n,\sigma})|)\Theta(-|\mathrm{Im}(v_{m,\sigma'})|). \end{aligned} \tag{3.14}$$

Let us elaborate on the objects entering this relation, which has a central character in our theories. The matrix structure of the Green's function in Eq. (3.14)

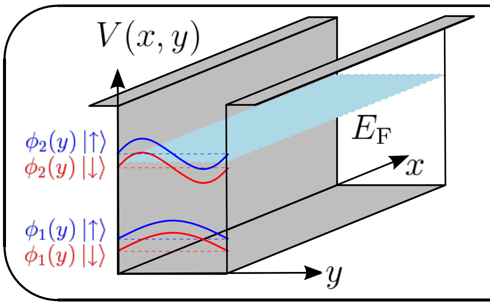

Figure 3.3: (lead spin polarization) Sketch of the potential landscape in a lead with Zeeman splitting and spin polarized transversal channel $\phi_2(y)$.

is indicated by the indexes σ and σ'. Latter correspond to an arbitrary set of complete basis states $\{|\sigma\rangle, |\sigma'\rangle\}$, with respect to which the Green's function is represented as

$$\mathrm{G}^{\sigma\sigma'}(\mathbf{q}',\mathbf{q};E_\mathrm{F}) = \langle\sigma|\,\mathrm{G}\,(\mathbf{q}',\mathbf{q};E_\mathrm{F})\,|\sigma'\rangle\,. \tag{3.15}$$

We consider a transverse confinement potential $V(x,y)$, as depicted in Fig. 3.3.

For illustration we ignore the presence of orbital effects due to a magnetic field in the leads. The lead eigenstates ξ can then be obtained via separation,

$$\left|\xi_n^{\pm,\sigma}(\mathbf{r})\right\rangle = \frac{1}{\sqrt{v_{\sigma,n}}}e^{\pm ikx}\cdot\phi_n(y)\,|\sigma\rangle\,. \tag{3.16}$$

The velocity prefactor in (3.16) ensures normalization of the wavefunctions with respect to unit flux [110]. This choice of normalization results in a unitary scattering matrix S, that obeys $SS^\dagger = \mathbb{1}$ [107, 110].
The transverse component $\phi_n(y)$ entering Eq. (3.16), is indexed by an integer quantum number n [52]. For a hard wall transversal confinement[2], $\phi_n(y)$ is an eigenstate of a one dimensional infinite potential well,

$$\phi_n(y) = \sqrt{\frac{2}{D}}\sin\left(\frac{n\pi y}{D}\right). \tag{3.17}$$

The lead's diameter is given by D. In Fig. 3.3 given eigenstates of the ground state and the first excited level are plotted. A homogeneous magnetic field $B_z\hat{z}$ in the leads couples via Zeeman interaction to the spin degree of freedom and lifts the degeneracy of the eigenstates, indicated by the blue and red coloring in Fig. 3.3.
The overall energy of the wavefunction $|\xi\rangle$ has to add up to Fermi Energy E_F, since energy is conserved. To determine which channels contribute to the asymptotic wavefunction, we look at the dispersion relation of ξ_n

$$E_\mathrm{F} = \frac{\hbar^2k^2}{2m_\star} + \frac{\hbar^2\pi^2n^2}{2m_\star D^2} + \sigma\frac{\mu_B g_\mathrm{eff} B_z}{2}. \tag{3.18}$$

---

[2] A hard wall confinement is defined by $V(y=0) = V(y=D) = \infty$; $V(y\in]0,D[) = 0$.

Particles in the leads hence have longitudinal velocities

$$v_{n,\sigma} = \sqrt{2/m_\star}\sqrt{E_\mathrm{F} - \frac{\hbar^2 n^2 \pi^2}{2m_\star D^2} - \sigma\frac{\mu_B g_\mathrm{eff} B_z}{2}}, \tag{3.19}$$

which depend on their spin polarization σ and transverse channel number n respectively. In the context of this work we neglect terms due to spin-orbit coupling in the leads.

Thus, the value of E_F determines the number of conducting channels, i.e. the quantum numbers n for which the velocities defined above remain purely real quantities. Complex velocities result due to normalizability in an asymptotically decaying scattering state. We implemented this mathematically via the Heavyside functions,

$$\Theta(x) = \begin{cases} 1 & \text{if } x > 0 \\ 0 & \text{else} \end{cases}, \tag{3.20}$$

entering Eq. (3.14). Note that due to the lifted spin degeneracy, the maximum integer number N_σ for which this holds, may differ for both spin species. Thus the number of conducting channels that contribute to spin polarized current is

$$\Delta = |N_\uparrow - N_\downarrow|. \tag{3.21}$$

An example is indicated by the choice of the Fermi energy, marked by the blue surface, in Fig. 3.3. The shown lead supports both spin polarizations in the transverse ground state, which correspond to particle current that is not spin polarized. However only one spin direction is supported for the first excited state, rendering the latter spin polarized.

The unpolarized channels lead to the classical background conductance G_Bg. We consider a two terminal device with identical leads, containing the same number of propagating channels N. Because of the unitarity of the scattering matrix, the total reflection R and transmission T must obey the relation [52],

$$T + R = N. \tag{3.22}$$

Note that the Fisher-Lee relations and the conditions outlined so far, constitute the starting point for further numerical as well as analytical considerations.

We will now explain how the conductance can be obtained concretely. The first method that we use throughout this work is a numerical algorithm explained in the subsequent section 3.4, while the second approach is of analytical nature and consists of the semiclassical approximation to quantum mechanicals systems. This point will be presented in section 3.5

3.4 Numerical approach to the transport problem

In order to perform numerical calculations on the various system classes we utilize a recursive Green's function library developed by Wimmer [47, 20]. The foundation of this scheme is the iterative calculation of the Green's function from a given Hamiltonian and specified boundary conditions to obtain the linear response scattering matrix.

3.4.1 Mapping to a tight binding Hamiltonian

For this purpose the physical system is mapped to a matrix. The latter can be given in terms of a tight binding Hamiltonian using atomic orbitals as basis. While the latter approach is helpful for the description of Graphene structures, electron and hole gas systems can be modeled in terms of a similar description, which is based on the method of finite differences [20].

This is achieved by mapping the differential operators acting on a spatially dependent wavefunction $\Psi(x, y)$ onto the corresponding approximate expressions in discretized space. The latter is defined by a square grid, such as shown in Fig. 3.4. For example the longitudinal kinetic energy component at position (x_i, y_i) is represented as [52],

$$\left[-\frac{\hbar^2}{2m_\star}\frac{\partial^2}{\partial x^2}\Psi(x,y)\right]|_{x=x_i,y=y_l} \to t\left(2\Psi(x_i,y_l) - \Psi(x_{i-1},y_l) - \Psi(x_{i+1},y_l)\right), \tag{3.23}$$

which motivates a renormalization of all numerical energy scales by the hopping parameter

$$\tilde{t} = \frac{\hbar^2}{2m_\star a^2 \mathrm{nm}^2} =: \frac{m_\mathrm{e}}{m_\star} t. \tag{3.24}$$

The quantity $\tilde{t}$ depends on the spacing between grid points a. The closer we approach the limit of $a \to 0$, the better the differential operators are modeled. It is useful to establish a universal transformation between numerical and SI units and remove the material dependence of the effective mass $m_\star$ from the hopping parameter. This is achieved by using the free electron mass m_e in the definition of t on the right hand side of Eq. (3.24).

As consequence of renormalization an SI-energy E is related to a numerical energy scale $\tilde{E}$ by

$$\tilde{E} = \frac{E}{t} \approx 0.02625 a^2 \frac{E}{\mathrm{meV}}. \tag{3.25}$$

Intuitively this allows for the construction of a matrix, which connects the set of discretized position eigenstates $|x_i\rangle\,|y_l\rangle\,, |x_j\rangle\,|y_m\rangle$, where the indexes $i(j)$ and $l(m)$ represent all positions on the square grid which are part of the considered system.

Since we aim at describing derivatives up to cubic order, we have to include next- and third-nearest neighbor hopping terms in the numerical grid, as shown in Fig. 3.4. More precisely, to correctly model the cubic momentum dependence in a 2DEG, no second-next-nearest neighbor terms have to be included due to the absence of the cubic terms k_x^3 or k_y^3.

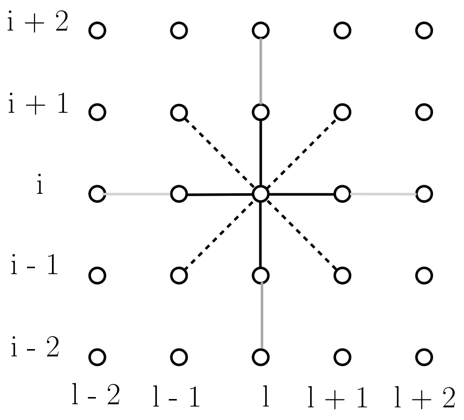

Figure 3.4: (numerical grid) Numerical relevant grid for descretization of derivatives in two-dimensions, including nearest-, next-nearest, and second-next-nearest neighbor hopping terms, indicated by the connections between the nodes. The second-next-nearest neighbor connections are marked by the gray coloring. While for the description of the 2DEGs in these text they are not of relevance, they have to be included in the 2DHG model.

For illustration we give below the expressions for all relevant derivatives, that are treated in the present and related works [20, 64].

$$\zeta_1 k_x/t \to -i\frac{\zeta_1}{2ta_0}\mathrm{sgn}(x_j - x_i)\delta_{i,j\pm1}\delta_{l,m}; \tag{3.26}$$

$$\zeta_1 k_y/t \to -i\frac{\zeta_1}{2ta_0}\mathrm{sgn}(y_m - y_l)\delta_{l,m\pm1}\delta_{i,j}; \tag{3.27}$$

$$\zeta_2 k_x^2/t \to \frac{\zeta_2}{t}(2\delta_{i,j} - \delta_{i,j\pm1})\delta_{l,m}; \tag{3.28}$$

$$\zeta_2 k_y^2/t \to \frac{\zeta_2}{t}(2\delta_{l,m} - \delta_{l,m\pm1})\delta_{i,j}; \tag{3.29}$$

$$\zeta_3 k_x^3/t \to i\frac{\zeta_3}{2ta_0^3}\mathrm{sgn}(x_j - x_i)(\delta_{i,j\pm2} - \delta_{i,j\pm1})\delta_{l,m}; \tag{3.30}$$

$$\zeta_3 k_y^3/t \to i\frac{\zeta_3}{2ta_0^3}\mathrm{sgn}(y_m - y_l)(\delta_{l,m\pm2} - \delta_{l,m\pm1})\delta_{i,j}; \tag{3.31}$$

$$\zeta_3 k_x^2 k_y/t \to i\frac{\zeta_3}{2ta_0^3}\mathrm{sgn}(y_m - y_l)(\delta_{i,j\pm1}\delta_{l,m\pm1} - 2\delta_{i,j}\delta_{l,m\pm1}); \tag{3.32}$$

$$\zeta_3 k_x k_y^2/t \to i\frac{\zeta_3}{2ta_0^3}\mathrm{sgn}(x_j - x_i)(\delta_{i,j\pm1}\delta_{l,m\pm1} - 2\delta_{i,j\pm}\delta_{l,m}); \tag{3.33}$$

Note that except for Eq. (3.30) and Eq. (3.31), it suffices to consider only next nearest neighbor hopping, despite the cubic structure of differential operators. This is due to our particular choice of discretization, which allows for enhanced performance when performing calculations on 2DEG systems.

The quantities ζ_1 and ζ_3 represent the linear and cubic SOI parameters that are discussed in this work. Their respective relations with their dimensionless numerical counterparts are given by

$$\tilde{\zeta}_1 = \frac{\zeta_1}{2ta} \approx 0.001312a\frac{\zeta_1}{\mathrm{meV\AA}} \quad \text{and} \tag{3.34}$$

$$\tilde{\zeta}_3 = \frac{\zeta_1}{2ta^3} \approx 0.001312a^{-1}\frac{\zeta_3}{\mathrm{meV\AA}^3}. \tag{3.35}$$

In the finite difference scheme the coupling of the magnetic gauge field $\boldsymbol{A}$ to the momentum is established using Peierl's substitution [111]. The corresponding phase term is calculated via Gaussian quadrature integration [112] along the link connecting two grid points $\boldsymbol{x}_1$ and $\boldsymbol{x}_2$. The resulting value of

$$\exp\frac{i}{\hbar}\int_{\boldsymbol{x}_1}^{\boldsymbol{x}_2}\boldsymbol{A}(\boldsymbol{x})\cdot\mathrm{d}\boldsymbol{x}, \tag{3.36}$$

is then multiplied to the respective link matrix element [20].

The numerically used magnetic field strengths are consequently related to a realistic field by

$$\tilde{B} = \frac{2\pi\mathrm{nm}^2}{\phi_0}B \approx 0.001519\frac{B}{T}. \tag{3.37}$$

Zeeman terms are rescaled accordingly,

$$\tilde{E_{\mathrm{Z}}} = \frac{\mu_{\mathrm{B}}g_\star B}{2t} \approx 0.4993a^2 g_\star\tilde{B}. \tag{3.38}$$

We will consider transport in the linear response regime close to the Fermi energy. Therefore the kinetic contribution to the energy is expected to dominate other relevant energy scales.

Consequently we approximate the experimentally measurable charge carrier density n_s to E_{F} by the density of states of a two-dimensional electron gas only described by the Helmholtz-equation as [52]

$$E_{\mathrm{F}} = 2\pi\frac{\hbar^2}{2m_\star}n_s = 2\pi\frac{\hbar^2}{2m_\star}\frac{N_s}{V}, \tag{3.39}$$

where N_s is the number of carriers in a two-dimensional electron or hole gas with spatial extend V. In the experiments discussed in this work, n_s assumes values of the order $10^{15} - 10^{16}\mathrm{m}^{-2}$ and correspondingly several meV of E_{F}.

When neglecting SOI terms of the dispersion, the connection of the inplane momentum $\boldsymbol{k}_\|$ to the density of states $\rho_{2D}(E)$ is easily established via the relation,

$$N_s = \int_0^{E_{\mathrm{F}}}\mathrm{d}E\rho_{2D}(E) = \int_0^{E_{\mathrm{F}}}\mathrm{d}E\frac{2}{(2\pi)^2}\int\mathrm{d}k_\|\delta\left(\frac{\hbar^2k_\|^2}{2m_\star}-E\right) = \frac{m_\star}{\pi\hbar^2}E_{\mathrm{F}}, \tag{3.40}$$

and the approximation

$$E_{\mathrm{F}} \approx \frac{\hbar^2k_{\|,\mathrm{F}}^2}{2m_\star}, \tag{3.41}$$

which leads to

$$k_{\|,\mathrm{F}}^2 = 2\pi N_s. \tag{3.42}$$

3.4.2 Requirements for numerical convergence

The SOI terms with cubic momentum dependence entering our 2DHG model make it necessary to discuss the convergence of our numerical ansatz specifically. Our goal is to identify the appropriate granularity for the used discretization in order to model a physical system correctly. One obvious criterion of correctness is the resolution of the smallest wavelength on the numerical grid. The Fermi wavelength λ_{F} represents this quantity. Thus, for a given energy, λ_{F} should contain enough lattice points of the numerical grid. The specific values we typically use is of the order 10 lattice points per λ_{F}.
In addition to this heuristic rule, we estimate the quality of our approximation by comparing exact dispersions with the energies of the corresponding discretized operators, as introduced in Eq. (3.23).
To verify whether a free particle is described correctly within this approximation, we insert into the right hand side of Eq. (3.23) a solution of the one dimensional free particle Schrödinger equation with wavenumber k, i.e. $\Psi(x) = \exp(ikx)$. We drop all constant prefactors for the sake of simplicity. From this procedure we hence obtain the approximate dispersion

$$E_2 = \frac{1}{a^2}(2 - 2\cos ka) = k^2 - \frac{1}{12}k^4a^2 + \mathcal{O}(a^4). \tag{3.43}$$

This means the ratio of the first order error term and the exact energy of a free plane wave $E_k = k^2$ is given by

$$\frac{|\delta E_2|}{E_k} = \frac{1}{12}k^2a^2. \tag{3.44}$$

Accordingly, we discretize a unidirectional cubic derivative as

$$i\frac{\partial^3}{\partial x^3}\Psi(x) \approx -i\frac{\Psi(x+2a) - \Psi(x-2a) - 2\Psi(x+a) - 2\Psi(x-a)}{2a^3}, \tag{3.45}$$

which yields, when applied to a plane wave

$$E_3 = \frac{i}{2a^3}(2 - 2\cos ka) = -\frac{1}{a^3}(\sin(2ka) - 2\sin(ka)) = k^3 - \frac{1}{4}k^5a^2 + \mathcal{O}(a^5), \tag{3.46}$$

and the error estimate with $E_k = k^3$,

$$\frac{|\delta E_3|}{E_k} = \frac{1}{4}k^2a^2, \tag{3.47}$$

which is already a factor of 3 larger than the discretization of the second derivative.
Thus cubic derivatives with second-next-nearest neighbor hopping demand for a finer discretization of the numerical grid a and restrict the regime of numerically converged results to small k. On the other hand, electronic calculations with cubic derivatives but without second-next-nearest neighbor hopping are less involved.

Apart from the requirements to the numerical mesh, there are additional limitations to which the the cubic spin-orbit terms are subject.
The latter are the result of an expansion in the inplane momentum to third order in $\boldsymbol{k}$, based on the assumption that they represent small corrections to the kinetic energy only [53]. Thus a physically meaningful choice of parameters is restricted to small ratios

$$\frac{\gamma k_{\mathrm{F}}^3}{\frac{\hbar^2}{2m_{\mathrm{eff}}}} = 2k_{\mathrm{F}} a\tilde{\gamma} = 2\tilde{k}\tilde{\gamma}, \tag{3.48}$$

with a numerical wavenumber $\tilde{k}$ and spin precession length $\tilde{\gamma}^{-1}$. In the calculations of the 2DEG the value of this ratio is not larger than 7%, in the 2DHGs not larger than 5%.
Stated prerequisites for the accurate numerical modeling of a realistic system are directly connected with the expensiveness of the algorithm. The computation time scales cubically with the number of grid points per lead width N_g in a stripe geometry, but only linearly with the respective length of the scattering region [47]. The currently used implementation [47] of the algorithm is highly optimized. Moreover our calculations are parallelized and carried out on the Athene high performance cluster at the university of Regensburg. Nevertheless, modeling typical low temperature experiments in semiconductors, in which E_{F} is of the order of eV and system widths exceed several hundred nm, are not feasible. Therefore, we simulate transport in a model, in which energy and length scales are downscaled consistent with experimental parameters. That is, ratios of relevant energy scales such as Fermi and Zeeman energies are identical to the experimental ratios. Length scale ratios of mean free path and modulation lengths of spatial potential anisotropies are taken into account accordingly. We take into account the self averaging of extended samples [52], by adjusting the ratio of numerical system length and mean free path, to the experimental phase coherence length and mean free path, since, strictly speaking, the numerical phase coherence length would be infinite, but is effectively limited by the discretization. We mimic extended samples and the two-dimensional bulk, by periodically extending the grid in transversal direction. This procedure hardly changes the computational cost and also diminishes boundary effects, if mean free path and spin precession lengths are exceeded by one unit cell width of the periodical superlattice. We are grateful to Viktor Krückl for helping with the implementation of the periodic boundary conditions.

3.4.3 Recursive calculation of the scattering matrix

A detailed description of the used numerical approach is to be found in Ref. [20]. In the following we restrict ourselves to a brief summary of appendix B in

Ref. [20]. Key elements of the recursive Green's function (RGF) scheme is the application of the iterative application of the Dyson equation

$$\mathrm{G} = \mathrm{G}_0 + \mathrm{G}_0 \mathrm{V} \mathrm{G}. \tag{3.49}$$

According to the latter, the retarded Green's function G can be calculated recursively from the unperturbed Green's function G_0 in the presence of a perturbation V. In the case of our numerical scheme, the objects corresponding to G_0 are Green's functions of the isolated system and the leads respectively. We remind ourselves that the isolated system is represented as a matrix H. The corresponding Green's function is defined as the inverse of this matrix, upon neglecting the infinitesimal element. Additionally the surface Green's functions of the isolated leads can be determined semi-analytically. Goal of the RGF method is to evaluate the Green's function of the connected system. To this end, the system is partitioned into N slices, in the following indexed by the integer i. The connection between the slices is given by the matrix

$$V = \begin{pmatrix} 0 & H_{i-1,i} & \\ H_{i,i-1} & 0 & \\ & & \ddots \end{pmatrix}, \tag{3.50}$$

which enters Dyson's formula as pseudo perturbation, A numerical iteration over the identities

$$G^{r(i-1)}_{i-1,i-1} \quad = \left(E - H_{i-1,i-1} - H_{i-1,i} G^{r(i)}_{i,i} H_{i,i-1}\right)^{-1} \quad \text{and} \tag{3.51}$$

$$G^{r(i-1)}_{N+1,i-1} \quad = G^{r(i)}_{N+1,i} H_{i,i-1} G^{r(i-1)}_{i-1,i-1}, \tag{3.52}$$

ultimately yields the objects $G_{N+1,0}$ and $G_{0,0}$, from which the transmission and reflection amplitudes of a two-terminal device can be extracted using a generalized form of the Fisher-Lee relations [20].

In the used notation, $G^{r(i-1)}$ denotes the Green's function of the subsystem that includes all blocks with index $\geq i$. Equation (3.52) explains the scaling of the computation time with system dimension, since the numerical matrix inverse scales cubically with the matrix dimension, which in turn is given by the number of grid points of a single slice.

3.5 Semiclassical approach to transport

In this section we specify the connection between the semiclassical picture of a precessing spin and transmission of a mesoscopic conductor. We will first introduce the semiclassical Green's function, on which is central to this discussion.

3.5.1 Semiclassical Green's function with spin

Our analytical results are based on the semiclassical approximation [113], which is valid if $\mathrm{Min}(k_{\mathrm{F}}L, k_{\mathrm{F}}L_{\phi}) \gg 1$ holds.

An intuitive connection between spin physics and transport properties can be obtained by applying the semiclassical formalism. Semiclassical in the context of the present work is not to be confused with the terminology of Ref. [54], in which the expression is mentioned in the context of the Boltzmann approach.

Instead, our present discussion is based on Gutzwiller's semiclassical formulation of the retarded Green's function on the energy shell at E_{F}, which can be generalized to the spin dependent representation [95, 114, 108, 115]

$$\mathrm{G}_{\mathrm{sc}}^{\sigma\sigma'}\left(\mathbf{q}',\mathbf{q};E_{\mathrm{F}}\right) = \sum_{r(\mathbf{q}\to\mathbf{q}')} -\sqrt{\frac{i}{2\pi\hbar^3}}\frac{1}{v_{\mathrm{F}}\sqrt{|\mathrm{M}_{12}^r|}}\exp\left(\frac{i}{\hbar}S(\boldsymbol{q},\boldsymbol{q}',E_{\mathrm{F}})_r - i\frac{\nu_r\pi}{2}\right)\mathrm{D}_r^{\sigma\sigma'}. \tag{3.53}$$

M_{12}^r is a matrix element of the classical stability matrix M_r. The latter describes the evolution of a small displacement perpendicular to the trajectory r and is defined as

$$\mathrm{M}^r := \begin{pmatrix} \frac{\partial q'_\perp}{\partial q_\perp} & \frac{\partial q'_\perp}{\partial p_\perp} \\ \frac{\partial p'_\perp}{\partial q_\perp} & \frac{\partial p'_\perp}{\partial p_\perp} \end{pmatrix}_r , \tag{3.54}$$

where $(\boldsymbol{q}_\perp(t), \boldsymbol{p}_\perp(t))$ and $(\boldsymbol{q}'_\perp(t), \boldsymbol{p}'_\perp(t))$ are phase space coordinates in a reference frame perpendicular to trajectory r, at initial and finite point respectively [116].

A detailed presentation of how to arrive at result (3.53) for a spin dependent effective mass Hamiltonian can be found in Ref. [108].

For the illustrative purpose of the semiclassical approach used in the following, we focus on the details of the derivation relevant to our results in appendix B. In G_{sc} the quantity r indexes all classical trajectories that connect the two points $\boldsymbol{q}$ and $\boldsymbol{q}'$ on the energy surface defined by $E_{\mathrm{F}} = H(\boldsymbol{p},\boldsymbol{q})$. Up to the spin dependent terms, the quantum mechanical Hamilton operator H, as it has been defined in Eq. (2.25), is the Weyl representation of the classical Hamiltonian H. S_r is the classical action calculated along the path r. The quantity ν_r is called Maslov index and takes into account singular points of the amplitude along the path r [113]. Such points include caustics, or simply the reflection at a hard wall, which leads to a phase jump of π.

As for the exact Green's function, the matrix structure of Eq. (3.53), depends on a basis $\{|\sigma\rangle, |\sigma'\rangle\}$ and is given by

$$\mathrm{G}_{\mathrm{sc}}^{\sigma\sigma'}\left(\mathbf{q}',\mathbf{q};E_{\mathrm{F}}\right) = \langle\sigma|\,\mathrm{G}_{\mathrm{sc}}\left(\mathbf{q}',\mathbf{q};E_{\mathrm{F}}\right)|\sigma'\rangle\,. \tag{3.55}$$

The same holds for the matrix D_r, which contains the information connected with spin Berry phase related physics [114]. The trajectories r are usually treated decoupled from the spin dynamics [95]. This is justified by the dominance of the kinetic energy term in the Hamiltonian, ensuring that in the reference frame of the particle spin evolution is a continuous process. Consequently D_r is defined for each phase space trajectory $\{\boldsymbol{q}_r(t), \boldsymbol{p}_r(t)\}$ via the time dependent matrix equation

$$\mathrm{i}\hbar \frac{\partial}{\partial t} \mathrm{D}_r(t) = \boldsymbol{\sigma} \cdot \boldsymbol{\mu}_r \left[\boldsymbol{q}_r(t), \boldsymbol{p}_r(t)\right] \mathrm{D}_r(t). \tag{3.56}$$

Equation (3.56) is also denoted as spin transport equation, consistent with other semiclassical studies of spin evolution [53, 114]. Remarkably, although the Green's function is defined on a surface of constant energy, the spin evolution kernel D_r can be expressed as the solution of the time dependent problem defined by Eq. (3.56).

Equation (3.56) offers a general definition of the spin evolution kernel found by iterative solution, in terms of the time ordered exponential $\mathrm{Texp}(x)$,

$$D_r(t) = \mathrm{Texp}\left(-\frac{\mathrm{i}}{\hbar} \boldsymbol{\mu} \cdot \boldsymbol{\sigma}\right). \tag{3.57}$$

Additionally Eq. (3.56) has an intuitive connection to the dynamics of a spinning particle. This is demonstrated by Bolte and Keppeler in Ref. [114]. Mentioned authors define a spin operator $\boldsymbol{\Sigma}(t)$ via the relation

$$\frac{\partial}{\partial t} \boldsymbol{\Sigma}(t) := \mathrm{D}_r^\dagger(t) \boldsymbol{\sigma} \mathrm{D}_r(t), \tag{3.58}$$

with the initial condition $\boldsymbol{\Sigma}(0) = \boldsymbol{\sigma}$. Upon application of Eq. (3.56), they show that the time evolution of the spin operator is described by the Bloch equation [117, 36],

$$\frac{\partial}{\partial t} \boldsymbol{\Sigma}(t) := \frac{1}{\hbar} \boldsymbol{\mu}(t) \times \boldsymbol{\Sigma}. \tag{3.59}$$

Equation (3.59) obviously describes a vector $\boldsymbol{\Sigma}$ that precesses around the axis defined by a magnetic moment $\boldsymbol{\mu}$ and can be parameterized in order to describe spin [114] with classical equations of motion, including the Thomas-precession [118].

Spin relaxation is usually described by phenomenological equations based on Eq. (3.59), which include the relevant spin relaxation rates [36].

A rapidly varying spin along path r leads to a breakdown of this picture used in the underlying Trotterization ansatz outlined in Ref. [108]. We summarize the main points in appendix A.

To illustrate the effectiveness of the semiclassical approach, we proceed by checking the semiclassically calculated result for the transmission of a ballistic waveguide. The latter has a well known energy dependence, the characteristic transmission staircase of a quantum point contact [119].

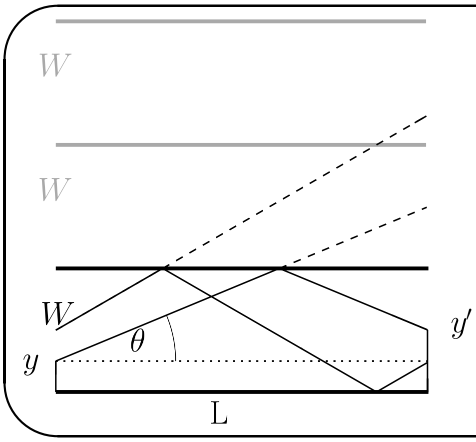

Figure 3.5: (extended zone scheme for a waveguide) Ballistic waveguide with hard walls. Gray colored horizontal lines represent the extended zone scheme. The dashed paths traverse the same distance as the classical paths with incident angle θ. Depending on whether the path includes an even or odd number of reflections there is a unique relation between coordinate y and y' as given in (B.7) and (B.8).

3.5.2 Spin degenerate waveguide structures

We consider a ballistic waveguide of width W and length L. The latter is considered as extension of two leads, between which charge current flows. A simple sketch of such a waveguide is shown in Fig. 3.5.

Throughout this text we assume that the condition $k_{\mathrm{F}}L \gg 1$ holds, for a given Fermi wavenumber k_{F}. This criterion renders the classical action the dominant phase contribution and justifies the multiple application of the stationary phase approximations that lead us to the expression (3.53). We further simplify the problem by neglecting the vector potential and start with a spin degenerate ballistic waveguide. The Schrödinger equation of the latter is equivalent to the Helmholtz equation [116], for which Eq. (3.53) is specialized to

$$G_{sc}^{\sigma\sigma'}(x',y',x,y;E_{\mathrm{F}}) = -\frac{\mathrm{i}m}{\sqrt{2\pi\mathrm{i}}\hbar^2}\sum_{r(y\to y')}\frac{1}{\sqrt{k_{\mathrm{F}}l_r}}\mathrm{e}^{\mathrm{i}k_{\mathrm{F}}l_r-\mathrm{i}n_r\pi}, \tag{3.60}$$

which is explicitly given in Ref. [120]. The phase and the stability terms are recast in terms of the trajectory length l_r. The Maslov indexes are specified by the number of hard wall reflections n_r due to the absence of other critical points along each path.

In the case of the ballistic waveguide, the semiclassically obtained transmission amplitude t coincides with the exact quantum mechanical solution,

$$t_{nm} = i\delta_{nm}\exp\left(ik_{\mathrm{F}}L\cos\theta_n\right), \tag{3.61}$$

with the transversal momentum component of a propagating mode n, given by

$$\cos\theta_n = \sqrt{1-\left(\frac{n\pi}{k_{\mathrm{F}}W}\right)^2}. \tag{3.62}$$

It is straightforward to obtain the eigenfunctions of the waveguide. The latter lead to the exact Green's function in spectral representation [52]. Now we are able to compare the exact transmission to the semiclassical result. We achieve this by inserting the exact and the semiclassical Green's function (3.60) respectively in the Fisher-Lee relation (3.14) and integrating the resulting expression out.

In appendix B we present the calculation in detail. Despite the simplicity of the basic problem, we are unaware of a published semiclassical computation of a closed expression for the transmission, possibly because the explicit summation over semiclassical paths is technically involved. We show an example of such paths, using an extended zone scheme [121], in Fig. 3.5.

3.5.3 Spin in semiclassical transport theory

In Ref. [122] we find an expression for the semiclassical conductance between two leads,

$$T = \int \mathrm{d}y \int \mathrm{d}y' \sum_{r,r'} A_r A^\star_{r'} e^{\frac{i}{\hbar}(S_r - S_{r'})} \mathrm{Tr}\left[D_r D_r^\dagger\right], \tag{3.63}$$

with actions S_r, stability amplitudes A_r and spin evolution matrices D_r of a classical trajectory r, defined in consistence to the Refs. [94, 95].

Considering either a wide ballistic waveguide structure or a disordered system, we usually neglect effects of the systems boundary on the spin. In the context of semiclassical theory, the latter issue is extensively discussed in Ref. [122][3]. Corrections to the semiclassical Green's function, in which D_r in above formula is the leading order term of a series expansion Ref. [122]. We consider only the leading order because we restrict ourselves either to system with negligible SOI as compared to the Zeeman coupling (Chap. 4) or consider the two-dimensional bulk of a disordered conductor in our discussions in which SOI is relevant (Chap. 5).

Eq. (3.63) describes systems with leads which are unpolarized with respect to spin. This means that every channel supports both spin species. The latter justifies tracing out the spin degree of freedom.

Since we are explicitly considering spin polarized leads in Chap. 4, the trace can no longer be applied. It is therefore necessary to proceed with the Fisher-Lee relation (3.14) introduced previously, when deriving the semiclassical approximation to the transmission amplitude. To obtain semiclassical transmission amplitudes, we insert the semiclassical Green's function into Eq. (3.14). We continue from this point in a straightforward fashion and evaluate the integrals over the leads via a stationary phase approximation. For an integrable

---

[3] More precisely, focus of Ref. [122] was the impact of boundary corrections to the Green's function of quantum chaotic systems in the spirit of Balian and Bloch [123, 124, 125], which manifested itself in non-universal corrections to the spin conductance with respect to the random matrix theory (RMT). One of the major findings in cited work includes the correct prediction of the spin Hall effect, which could not be explained within RMT frameworks.

waveguide structure we show in appendix B the explicit calculation, which is non-universal, in contrast to the universal approach to a quantum mechanical systems with classically chaotic analogues. While integrable structures like the waveguide are characterized by path bundles which can be summed systematically, paths in chaotic structures are assumed to be isolated. As consequence semiclassical sum rules based on the ergodicity property of the phase space of such systems can be applied to simplify the calculation considerably [94].

Note that the presence of disorder may also render a waveguide chaotic. Independent if the system is chaotic or the special case of an integrable ballistic waveguide, the general structure of a semiclassical transmission coefficient is typically given by the expression,

$$t_{mn}^{\sigma\sigma'} = \sum_{r:n,\sigma'\to m\sigma} B_r e^{\frac{i}{\hbar}S_r} \left\langle \sigma \right| D_r \left| \sigma' \right\rangle , \tag{3.64}$$

with a renormalized classical stability amplitude B_r.

Details on the classical quantities are further of no relevance to our discussion. They are approximated as independent by the spin. Therefore new information content due to spin is included in the spin kernel.

Including spin in our waveguide example will consequently be achieved by straightforward extension of Eq. (3.61) to

$$t_{mn}^{\sigma\sigma'} = i\delta_{nm} \exp\left(ik_{\mathrm{F}} L \cos\theta_n\right) \left\langle \sigma \right| D_n \left| \sigma' \right\rangle . \tag{3.65}$$

Note that the saddle points of the semiclassical approximation uniquely link each classical trajectory to the incident angle of the quantum mechanical mode n.

To obtain the final transmission including geometric phases of the spin, we evaluate the spin evolution equation for D_n from (3.56) after inserting the relevant classical trajectory in the magnetic dipole Hamiltonian $\boldsymbol{\mu} \cdot \boldsymbol{\sigma}$.

Having shown the remarkable potential of the semiclassical approach to transport, we apply the theory presented above to a waveguide with nontrivial magnetic field texture in the subsequent chapter.

Chapter 4

Adiabaticity mediated spin control

The presence of a magnetic field $\boldsymbol{B}$ influences transport in various ways. Within the semiclassical description it affects the physics of a two-dimensional system on three levels:

- A magnetic field changes the classical dynamics of a charged particle. Straight line trajectories are replaced by cyclotron orbits perpendicular to the direction of a homogeneous $\boldsymbol{B}$.[1]
- Presence of a vector potential changes the action of each path by minimal coupling.
- Addition of spin structure to the problem via Zeeman coupling.

Consideration of a large Zeeman splitting allows us to focus on the third point, while other effects are of minor significance in the present context.

The first point is typically relevant at large values of B, which are associated by a cyclotron orbit radius

$$r_c = \frac{m_\star v_\mathrm{F}}{\mathrm{e}B}, \tag{4.1}$$

of the order or smaller than the mean free path [127]. We are interested in magnetic field scales that are small in that respect. In a simple picture the paths of the carriers are cyclotron orbits with radii that exceed the system size significantly. Thus these paths are approximately indistinguishable from carrier dynamics in absence of a magnetic field.

The second point is of major relevance to the problem of weak localization phenomena. It introduces a phase difference between otherwise time reversal

---

[1] Inhomogeneous magnetic fields lead to highly nontrivial classical trajectories. The latter have been extensively studied in the context of semiclassical transport in disordered samples [126].

symmetric paths [90]. We rule out mentioned effects in the present chapter because of the permanent presence of magnetic stray fields in the setups that inspired the upcoming discussion [1]. Hence we ignore the second point by considering time reversal symmetry broken. $\boldsymbol{B}$ may furthermore point in any direction. Components of $\boldsymbol{B}$ in the plane of the two-dimensional system, however should not effect orbital dynamics. This can be shown by choosing a convenient gauge for the vector potential $\boldsymbol{A}$ [64].

4.1 Motivation for the measurements

We present a mechanism that allows to manipulate spin polarized currents. Several advantages of our approach compared to previous concepts suggest ramifications to future device engineering.

The injection of spin polarized current from a ferromagnet into a semiconducting material is problematic because of the conductance mismatch problem. Latter is caused by the interface between both materials, which makes it hard to detect current spin polarization experimentally [34].

We circumvent this issue by using a dilute magnetic semiconductor as host material for our device. The latter is already intrinsically spin polarized at finite magnetic fields and low temperatures, as we show in Chap. 2.

The choice of this setting gives rise to spin polarized current. Controlling the this current's polarization is the goal of our proposed device building block, that acts as a spin transistor.

The presence of spin relaxation, which is caused by a number of different mechanisms, complicates them realization of similar devices [36].

In the present context, the Zeeman splitting is energetically much larger than momentum dependent SOI [1]. This feature renders the device operation robust against conventional spin relaxation.

The Datta-Das concept for a spin manipulation device relies on the presence of a momentum dependent Rashba type spin-orbit coupling [21]. This principally allows for tuning an external gate voltage to access the spin precession axis [21]. A demonstration of the Datta-Das type rotation of spin has so far only been identified in small signals in nonlocal measurements [128].

It should be noted that the term “spin transistor” is used ambiguously in the literature. In a standard electric transistor it is possible to control an output current with a smaller switching current, representing signal amplification, also called “gain”.

With respect to the gain property, our proposed device would be physically inefficient, since the output signal in terms of spin current amplification is very small compared to the current that is used to generate an external magnetic field - which defines the input signal. Contrasting to this perspective, we use the term “spin transistor” in Ref. [1] to describe a device property that Datta and Das originally denoted as “analogue to the electro-optical modulator” [21]. To summarize, the functionality of our proposed device is not based on gain, but on the ability to control the spin polarization of a given charge current - in analogy to the optical modulator, which allows to manipulate the polarization of light.

Achieving this kind of control relies on the coupling of spin to a spatially dependent magnetic superstructure. Although the underlying physics can principally be generalized to different setups, such as temporally driven systems, the discussion in the context of transport is illustrative and has been experimentally verified [1].

Mentioned magnetic texture is generated by a periodic array of pre-magnetized Dysprosium stripes separated from the 2DEG by an insulating layer as sketched in Fig. 4.1.

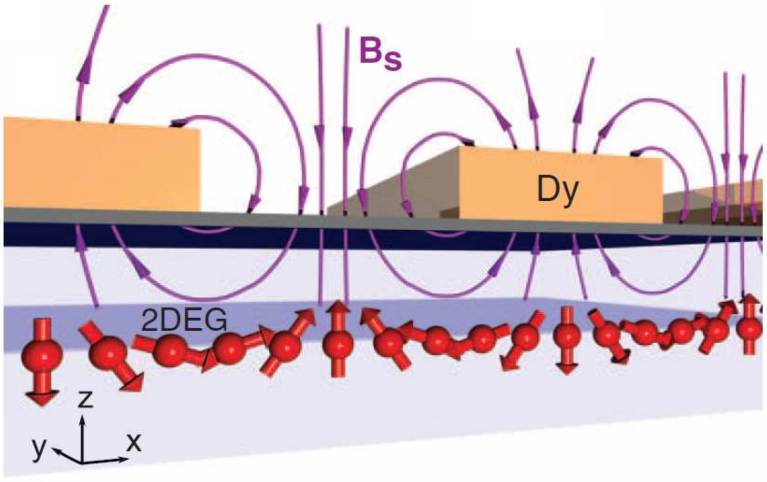

Figure 4.1: (experimental setup) Sketch of a 2DEG subject to the stray field texture $\mathbf{B_s}$ of magnetized Dy-stripes. The local electronic spin precession axis rotates periodically due to the spatially dependent Zeeman interaction. The picture includes the definition of the coordinate system and has been published in Ref. [1].

In the given setup spin dynamics can be controlled experimentally via switching of an additional magnetic field.

4.2 Experiment and model

We achieve control over current spin polarization in a CdTe semiconductor into which Manganese impurities are introduced. At low temperatures the s-d exchange coupling turns the material into a dilute magnetic semiconductor(DMS) [46]. As explained in section 2.6 of this work, a DMS is characterized by a large spin splitting, that can be described by a Zeeman term within a mean field model [63].

Because of the dominance of the giant Zeeman interaction, the spin precession axis follows the local magnetic field direction in the sample. This is indicated by the red arrows in Fig. 4.1. In a perfectly clean sample the local carrier spin polarization coincides with this direction in the referred setup. This behavior is attributed to the picture of adiabatic evolution in the context introduced by Born and Fock [129] and further outlined in appendix C.

For a formal description of how transmission is mapped to a time dependent problem of adiabatic spin evolution, we consider spin dependent quantum transport within the framework of the Landauer-Büttiker formalism [105, 107] as discussed in section 3.3. We use the effective mass Hamiltonian of the 2DEG in the (Cd,Mn)Te sample in the presence of a magnetic field $\mathbf{B}(\mathbf{x})$,

$$\hat{\mathrm{H}} = \frac{\hbar^2 \boldsymbol{k}^2}{2m_\star} + \boldsymbol{\mu} \cdot \boldsymbol{\sigma}, \tag{4.2}$$

as model.

For the beginning we ignore the magnetic vector potential $\mathbf{A}(\mathbf{x})$. Here, the Larmor frequency ω_L in the experiments of Ref. [1],

$$\omega_L = \frac{g_{\mathrm{eff}} \mu_{\mathrm{B}} B}{\hbar}, \tag{4.3}$$

is typically much higher as the corresponding cyclotron frequency ω_c,

$$\omega_c = \frac{eB}{m_\star}. \tag{4.4}$$

At low temperatures and a maximum magnetic field of 1 T we obtain values of $\omega_c = 1.8$ THz which is by a factor of $\sim 10^2$ smaller than ω_L. This factor is determined by the Zeeman splitting E_{Z} in the dilute magnetic semiconductor sample, described by the formula (2.18).

The periodic array of Dy-stripes, separated by an insulating layer from the conducting region, is magnetized prior to the transport measurements. The structure of the resulting stray field $\boldsymbol{B}_s$ is sketched as purple curves in Fig. 4.1.

After magnetization the sample is exposed to an additional external magnetic field $\boldsymbol{B}$, which is changed while the resistance is recorded within a multi-terminal measurement. The sweep of the external magnetic field contains values sufficiently below the coercive field of the Dy-stripes [1]. Thus we consider the stray field of the stripes effectively constant during each sweep.

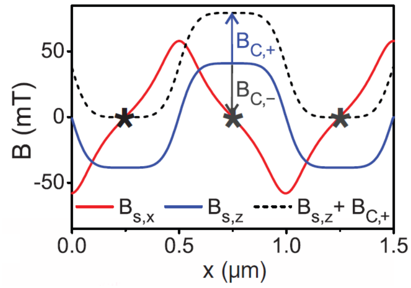

Figure 4.2: (stray field texture) Magnetic stray field plot from Ref. [1] of the typical out-of-plane stray field texture $B_{s,z}$ (blue line) and the longitudinal component $B_{s,x}$ (red line). Upon tuning an additional external field we manipulate the effective value of $B_{s,z} + B_{C,+}$ (dashed line), such that the total magnetic field amplitudes becomes zero at the position marked by an asterisk for the critical external field value B_C.

The total magnetic field in the 2DEG is consequently given by the superposition of $\boldsymbol{B}_s$ and $\boldsymbol{B}$ and has a component in the out of plane direction and one longitudinal component. We neglect any transversal component, which is justified if we consider the Dy-stripes as infinitely long [130]. The resulting field texture is periodic. In Fig. (4.2) we show a typical calculated stray field texture. Most importantly, as this plot indicates, at a critical value of the external field B_C, the total magnetic field can be tuned to zero value at certain positions in the 2DEG. These positions are indicated by the asterisk in Fig. (4.2).
The magnetic field enters the Zeeman term in the standard way,

$$\boldsymbol{\mu} \cdot \boldsymbol{\sigma} = \frac{1}{2} g_{\text{eff}} \mu_B (\mathbf{B} + \mathbf{B}_{\text{s}}(x)) \cdot \boldsymbol{\sigma}. \tag{4.5}$$

The out of plane component is given by $\boldsymbol{B} = B\hat{\boldsymbol{z}}$, while we use an approximation for the magnetic stray field,

$$\mathbf{B}_{\text{s}}(x) \approx B_{\text{s}} \sin(2\pi x/a)\hat{\mathbf{x}} + B_{\text{s}} \cos(2\pi x/a)\hat{\mathbf{z}}. \tag{4.6}$$

The distance between two Dy-stripes is defined here as a and ranges from 0.5 to 8 μm in Ref. [1]. The given cycloidal approximation of the stray field in the plane of the 2DEG covers the main characteristic of the exact field texture of Fig. 4.2, which includes the periodicity and the phase shift between the components.
The model has already been subject to various studies of spin transport in magnetically modulated structures [131] and in the context of helimagnets [132].
Based on the model previously outlined, we will focus on theoretical consequences - in particular the signatures in the spin transmission resulting from the variation of the locally inhomogeneous magnetic field.

For further details about the experimental setup and how the measurements were performed, we recommend to the reader the supplementary to Ref. [1] and the dissertation of Christian Betthausen [133], who produced the experimental data presented in Figs. 4.5 a) c) and d), and 4.6.
The micro-magnetic estimates of the stray field amplitudes in Fig. 4.6 a) have been calculated by Henri Saarikoski, and the numerical results on transport presented in Figs. 4.5 b), Fig. 4.6 b), Fig. 4.9 and Fig. 4.9 have been obtained in collaboration with Henri Saarikoski.

4.3 Spin polarized conductance

In the theoretical model of the described sample, the leads are covered homogeneously with Dysprosium. This induces locally a homogeneous magnetic field, which gives rise to a finite Zeeman splitting. The latter leads to a significant spin polarization with respect to the number of propagating channels Δ, defined in Eq. (3.21).

4.3.1 Lead eigenstates

The leads are hence fully transparent for one spin species while they reflect all modes n for which the tuple (n, σ) leads to an imaginary component of the longitudinal velocity $v_{n,\sigma}$, introduced in Eq. (3.19). For the states m in the identical right lead, the argument holds analogously for spin polarization σ', which is, like σ, considered with respect the $\hat{\mathbf{z}}$-spin quantization axis.
The eigenenergies E_n, given by the values $\frac{\hbar^2}{2m_*}\frac{\pi^2 n^2}{W^2}$; $(n = 1, 2, 3, ...)$ contribute to the transversal energy of the wavefunction or channel n, which is supported in the leads.
The semi-infinite leads are situated at the positions $x = 0$ and $x = L = ja$ with integer j. A total constant magnetic field of $(B + B_\mathrm{s})\hat{\mathbf{z}}$ is present inside the leads, which ensures continuity of the Zeeman field at the lead-cavity interface. Equation (3.18) correspondingly yields the energies of the lead wavefunctions,

$$E_{n,\sigma}(k) = \frac{\hbar^2 \boldsymbol{k}^2}{2m_*} + E_n + \frac{\sigma}{2} g_\mathrm{eff} \mu_\mathrm{B} (B + B_\mathrm{s}). \tag{4.7}$$

A tuple (n, σ) uniquely characterizes a spin channel, which is either transmitted or evanescent. Evanescent channels with a transmitted counterpart for identical index n contribute to the net current spin polarization, as sketched in Fig. 3.3.
Now we focus on the conducting region between two leads, or analogously the region between two magnetic stripes separated by distance a - see Fig. 4.3 for illustration.

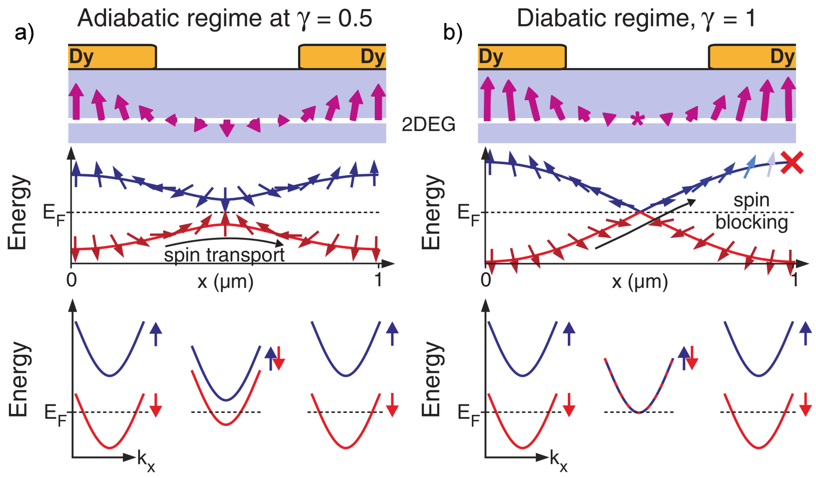

Figure 4.3: (schematic side view of the experiment) Sketch from Ref. [1] showing one segment of a magnetically modulated semiconductor with the magnetic field in the 2DEG plane (upper panel), the resulting inhomogeneous Zeeman splitting (middle panel) and the respective local band diagrams for both spin species (lowest panel). In the left plot (a) the magnetic field is tuned corresponding to a parameter $\gamma = B/B_s = 1/2$ which allows adiabatic spin evolution, the right situation (b) indicates reflection of one spin component at $\gamma = 1$ due to enhanced transition probability into an eigenstate that is reflected at the spin polarized lead. The amplitude of the stray field B_s is fixed while the external field B is changed to vary the parameter γ experimentally.

4.3.2 Spin dynamics in the cavity

We base the subsequent discussion on the semiclassical transport formalism introduced in paragraph 3.5.3, for a ballistic waveguide. Considering the scattering region as ballistic is a reasonable first approximation, justified by the experimental mean free paths which exceed the spacings in the Dy pattern.

The simplified system consists of a ballistic 2DEG waveguide with hard wall boundary conditions, and the field texture defined by Eq. (4.6).

Magnetically modulated patterns have been studied extensively in previous works. Kim et al. suggested that a semiconductor below a periodic array of permanent magnets can be used to control spin polarized currents in systems with large effective gyromagnetic factor [134]. This result was derived for a magnetic Kronig-Penney model [135] of periodically repeating maxima of the magnetic field component parallel to $\hat{z}$ while neglecting inplane components.

Spin polarization is attributed to the formation of minibands of the periodic superlattice imposed on the system [134]. In this discussion current spin polarization increases with an increasing number of modulations [134].

Extended studies on a variety of field textures including inplane magnetic field components exhibit a rich structure in the magnetoconductance, which is attributed to the presence of magnetic minibands [136].

The findings of Refs. [134, 135, 136] are however relevant to systems in which the period a of the superstructure is much smaller than the phase coherence length L_ϕ.

Although the current experimental setup includes periodic patterns, our results apply to systems in which L_ϕ is of the order of a. Hence effects due to superlattice-induced sub-band formation should be of minor importance.

We demonstrate in appendix B, that the semiclassical transmission amplitude between different channels can be expressed in terms of a summation over classical trajectories r.

As we show in paragraph 3.5.3, this is easily generalized to a spin dependent problem, if we treat the spin evolution matrix as a slowly evolving quantity relative to the quickly oscillating terms. Analogous to the spinless example, the spin dependent Green's function (3.53) is inserted into the Fisher-Lee relation (3.14).

The saddle points in the stationary phase approximation in the integral over the lead-cavity interface determine the classically relevant paths between initial lead channel (n, σ) and final lead mode (m, σ'). This gives rise to the amplitude

$$t_{mn}^{\sigma\sigma'} = i\delta_{nm} \exp\left(ik_{\mathrm{F}} L \cos\theta_n\right) \langle\sigma| \mathrm{D}_n |\sigma'\rangle \,. \tag{3.65}$$

the semiclassical approximation for a ballistic waveguide with spin split leads.

The initial position at the incident lead is set to the origin. The longitudinal component of trajectory $\boldsymbol{q}$ at this position is then approximated by

$$q_x(t) \approx v_{n,\sigma} t, \tag{4.8}$$

which we use to parameterize the spin transport equation,

$$\mathrm{i}\hbar \frac{\partial}{\partial t} \mathrm{D}_n(t) = \boldsymbol{\sigma} \cdot \boldsymbol{\mu} \left[\boldsymbol{q}_n(t), \boldsymbol{p}_n(t)\right] \mathrm{D}_n(t). \tag{4.9}$$

Now we focus on a channel n, for which only one spin polarization σ is propagating in the leads, the other evanescent. From Eq. (3.65) we then obtain,

$$|t_{mn}^{\sigma\sigma}|^2 = \delta_{nm} \exp \left|\langle\sigma| \mathrm{D}_n |\sigma\rangle\right|^2 , \tag{4.10}$$

from which we calculate the contribution to the transmission T_Δ of all spin polarized channels n,

$$T_\Delta = \sum_{n\in\Delta} \left|\langle\uparrow| \mathrm{D}_n |\uparrow\rangle\right|^2 , \tag{4.11}$$

where we consider spin polarization $\sigma = \uparrow$ with respect to the $\hat{z}$-quantization axis. This restriction suppresses the remaining 3 matrix elements that include $\downarrow$-polarization in one of the leads, $\langle\uparrow|\,\mathrm{D}_n\,|\downarrow\rangle\,, \langle\downarrow|\,\mathrm{D}_n\,|\uparrow\rangle$ and $\langle\downarrow|\,\mathrm{D}_n\,|\downarrow\rangle$.

At close inspection the velocity changes locally along a trajectory due to changing size of the Zeeman field. Here we rely on the argument on which the semiclassical approximation was based, that spin texture to first order does not affect quasiclassical paths [108]. This point is responsible for the fact that our simplified analytical approach does not obey the unitarity condition imposed on the scattering matrix. A more rigorous treatment including pseudo paths of multiple (back-) scattering processes between the energy minima principally should solve this problem. The latter is however beyond the scope of this work, in which the semiclassical picture merely enables basic understanding non-adiabatic transitions of the spinor in the given context.

An alternative approach to a related problem has been brought forward by G. Hagedorn and A. Joye in Ref. [137]. Mentioned authors calculated exact transmission amplitudes for Gaussian wavepackets with spin structure, that are subject to a magnetic texture. The probability amplitudes of the Landau-Zener model appear in the analytical results of Ref. [137] as leading order terms of a perturbation expansion of the exact transition rates. In contrast to this quantum mechanically exact approach, in the current discussion we focus on the illustrative character of our presentation, at the expense of unitary.

The main simplification in this respect consists of the approximative separation between classical evolution and evolution in the reference frame of the spin.

4.3.3 Non-adiabatic tunneling processes

The spinor part of the wavefunction is determined by the time dependent equation (4.9), which is formally analogous to the problem to which Berry introduced an analytical solution in terms of geometric phases [138].

We illustrate this connection by defining the quantum mechanical wavefunction of the time dependent spinor with initial polarization σ,

$$|\Psi(t)\rangle := \mathrm{D}_n(t)\,|\sigma\rangle\,, \tag{4.12}$$

which, combined with Eqs. (4.8) and (4.9) leads to the Schrödinger equation,

$$\mathrm{i}Q_{n,\sigma}^{-1}\frac{\partial}{\partial\tau}\,|\Psi(\tau)\rangle = \tilde{\mathrm{H}}\,|\Psi(\tau)\rangle\,, \tag{4.13}$$

on which the subsequent discussion will be based. Equation (4.13) for the specific magnetic texture (4.6) is given by the Hamiltonian

$$\tilde{\mathrm{H}}(\tau) = \begin{pmatrix} \gamma + \cos\tau & \sin\tau \\ \sin\tau & \gamma - \cos\tau \end{pmatrix}, \tag{4.14}$$

and the effective timescale

$$\tau := \frac{2\pi}{a} v_{n,\sigma} t. \tag{4.15}$$

For each semiclassical trajectory through the system we have an effective adiabaticity parameter

$$Q_{n,\sigma} = \frac{1}{2} \frac{\omega_{\mathrm{L}}}{\omega_{\mathrm{F}}^{n,\sigma}}, \tag{4.16}$$

with the Larmor frequency due to the stray field

$$\omega_{\mathrm{L}} := \frac{g_{\mathrm{eff}} \mu_{\mathrm{B}} B_{\mathrm{s}}}{\hbar}, \tag{4.17}$$

and the frequency $\omega_{\mathrm{F}}^{n,\sigma}$ with which a particle at velocity $v_{n,\sigma}$ traverses a periodically repeated segment of length a,

$$\omega_{\mathrm{F}}^{n,\sigma} := \frac{2\pi}{a} v_{n,\sigma} \quad \text{or} \quad \omega_{\mathrm{F}} := \frac{2\pi}{a} v_{\mathrm{F}}, \tag{4.18}$$

which is independent of the channel. Samples of μm width and Fermi energies exceeding 1 meV support a large number of open channels. In these cases, as well as disordered samples, it is convenient to define an alternative effective adiabaticity parameter Q for estimating whether a system behaves adiabatically,

$$Q := \frac{\omega_{\mathrm{L}}}{\omega_{\mathrm{F}}} \tag{4.19}$$

Adiabatic evolution of the spinor may only be observed, if $Q > 1$ holds.

We now consider the dimensionless equation (4.13). The solutions $\{|\chi_\sigma(\tau)\rangle\}$ of the instantaneous eigenvalue problem,

$$\tilde{\mathrm{H}}(\tau) \, |\chi_\sigma(\tau)\rangle := \tilde{e}_\sigma(\tau) \, |\chi_\sigma(\tau)\rangle \tag{4.20}$$

correspond to the eigenvalues

$$\tilde{e}_\sigma(\tau) := \sigma \sqrt{1 + \gamma^2 + 2\gamma \cos(\tau)}, \tag{4.21}$$

where $\sigma \in \{\pm 1\}$. The local structure of the eigenenergies is visualized in the middle panel of Fig. 4.3. An instantaneous spin precession axis $\mathbf{\Sigma}$ for these states is given by,

$$\mathbf{\Sigma}(\tau) = \langle \chi_\sigma(\tau) | \, \boldsymbol{\sigma} \, |\chi_\sigma(\tau)\rangle \, , \tag{4.22}$$

whose direction is indicated by the arrows placed on the respective bands in Fig. 4.3.

Analytically solving an equation of the structure (4.13) for a general time dependent $\tilde{\mathrm{H}}(\tau)$ is a nontrivial problem. One approach includes computation via Magnus expansion [139]. This method makes it however still hard to obtain a closed expression, since the complexity of occurring terms increases drastically with the considered order of the expansion.

Berry found an elegant way to circumvent complications like these by exploiting the fact that a wavefunction evolves adiabatically during slow changes of the Hamiltonian $Q_{n,\sigma}\tilde{\mathrm{H}}(t)$, according to the adiabatic theorem of quantum mechanics stated by Born and Fock [129, 138][2].
This holds for sufficiently large values of the adiabaticity parameter $Q_{n,\sigma}$, or Q for simplicity, which is illustrated by a renormalization of the time coordinate in Eq. (4.13) by Q. Realization of a large Zeeman splitting, as well as considering channels close to the Fermi surface, ensure this in the case of the experiments we describe in Ref. [1].
Based on the dimensionless equation (4.13), if the parallel transport requirement to the eigenstates is met [138], and the adiabaticity criterion $Q \gg 1$ holds, Berry showed that a wavefunction, that is initially polarized in one of the instantaneous eigenstates, remains in the eigenstate during variation of $\tilde{\mathrm{H}}(t)$, up to the trivial dynamical phase and an additional phase that it acquires. Latter phase has henceforth been denoted “Berry phase” or “Geometric phase”, since it is a geometrical property of a closed curve in the parameter space of $\tilde{\mathrm{H}}$.
A large value of Q is however not a sufficient condition for adiabatic evolution, as illustrated on the right side of plot 4.3. If the instantaneous bands approach each other, tunneling between the different levels occurs with a finite probability [48, 49, 140].
The spatially inhomogeneous Zeeman coupling is responsible for these transitions, which turn spin polarization σ into $-\sigma$, with respect to the local basis. We use the Landau-Zener model [48, 49] to describe these transitions analytically, in the adapted formula for the transmission amplitude,

$$\left|t_{mn}^{\sigma'\sigma}\right|^2 \sim \delta_{nm} \left|\langle\sigma'|\ \Psi_{n,\sigma}(\tau_{\mathrm{f}})\rangle\right|^2 = \delta_{nm}(1 - P_{n,\sigma}), \tag{4.23}$$

with the time τ_{f} after which an incident particle with initial spin σ, that entered the system at $\tau = 0$, crosses over to the outgoing lead.
This specifies T_Δ from Eq. (4.11) to,

$$T_\Delta = \sum_{n\in\Delta} (1 - P_{n,\uparrow}). \tag{4.24}$$

Here we used the definition of the spin dependent wavefunction given in Eq. (4.12) and introduced the non-adiabatic tunneling probability derived by Landau [48] and Zener [49],

$$P_{n,\sigma} = e^{-\Gamma_{n,\sigma}}, \tag{4.25}$$

which drops exponentially with the rate

$$\Gamma_{n,\sigma} = \pi Q_{n,\sigma}(|\gamma| - 1)^2, \tag{4.26}$$

---

[2] Appendix C of the present text includes a brief introduction to adiabatic evolution in a time dependent problem.

into which enters the experimentally controllable ratio of external field and stray field amplitude

$$\gamma := B/B_s. \tag{4.27}$$

We obtain the result (4.26) by directly applying Zener's model [49] for the probability P_{D} of adiabatic transition between bands close to an avoided crossing,

$$P_{\mathrm{D}} = e^{-\Gamma} \quad \text{with} \quad \Gamma = 2\pi \frac{\epsilon_{12}^2(0)}{\hbar \left| \frac{\partial}{\partial t} \left(\epsilon_+(t) - \epsilon_-(t) \right) \right|}, \tag{4.28}$$

and with the level splitting $2\epsilon_{12}(0)$. and the energies of the adiabatic eigenstates $\epsilon_\sigma(t)$. In Eq. (4.28) the energy minimum associated with the avoided crossing is situated at $t = 0$.

To obtain Eqs.(4.25) and (4.26) we evaluate Eq. (4.28) for the local band structure of our problem. The explicit structure of the eigenstates, which coincide the eigenstates of σ_z at the ends of the waveguide, i.e. $\tau = 0$ and, $\tau = 2\pi j$ with integer j. In the present discussion we only take into account one complex degeneracy point along a classical trajectory. This corresponds to considering one segment of the periodically repeated structure as isolated from the other segments. If the phase coherence length is of the order of the spacial periodicity this treatment is justified. Otherwise paths between different degeneracy points should be considered.

If a spinor that is an eigenstate with quantum number σ with respect to the $\hat{z}$-quantization axis enters the system, it remains in the state with the same quantum number with probability $1 - P_{n,\sigma}$. With the probability $P_{n,\sigma}$ tunneling to the different eigenstate with quantum number $-\sigma$ occurs in the cavity. At the final lead however, if we consider a spin polarized channel, the particle is reflected by the barrier that the growing Zeeman term represents for the spin polarization $-\sigma$. Therefore the spin polarized contribution of a current can be fully suppressed by this mechanism.

Note that Zener derived his expression for dispersions $\tilde{\epsilon}_\sigma$, here given by dimensionless quantities, that only coincide with our explicit problem to first order within a Taylor expansion. Dykhne generalized Landau's and Zener's result using complex analysis. In the work of Davis and Pechukas, Ref. [140], Dykhne's refined result is given as,

$$\Gamma = 2Q\mathrm{Im}\left\{ \mathrm{i} \int_{\mathrm{C}} \mathrm{dt} \left(\tilde{\epsilon}_+(\mathrm{t}) - \tilde{\epsilon}_-(\mathrm{t}) \right) \right\}, \tag{4.29}$$

where it is assumed that the instantaneous level splitting possesses a complex degeneracy at time τ_c. In Eq. (4.29), C is a path that starts at $\mathrm{Re}(\tau_c)$ on the real axis and ends at τ_c in the complex plane. Note that all units are absorbed into the parameter Q and the time coordinate t in the integration, as well as τ_c, are given by rescaled dimensionless quantities, to simplify the calculation.

For the Hamiltonian (4.14) we find the complex degeneracy point

$$\tau_c = \mathrm{iarccosh}\left(\frac{1+\gamma^2}{2\gamma}\right) + \pi, \tag{4.30}$$

and correspondingly a transition amplitude of

$$\Gamma_{n,\sigma} = |(1-\gamma)|\, 8Q_{n,\sigma}\mathrm{Im}\left\{\mathrm{E}\left[\mathrm{iarccosh}\left(\frac{1+\gamma^2}{2\gamma}\right), \frac{2\mathrm{i}\sqrt{\gamma}}{|1-\gamma|}\right]\right\}, \tag{4.31}$$

where a definition of the incomplete elliptic integral $\mathrm{E}(\phi,k) := \int_0^\phi \mathrm{d}\theta\sqrt{1-k^2\sin^2\theta}$ appears [112]. A comparison of the results (4.26) and (4.31) however shows, that for typical parameters the simple expression of the Landau-Zener tunneling rate (4.26) represents a good approximation to Dykhne's general result. Numerical results for a narrow waveguide with one propagating spin polarized channel indicate a good agreement with our resulting approximation to the transmission probability. We verify this for several different effective adiabaticity parameters $Q_{1,\uparrow}$ in Fig. 4.4.

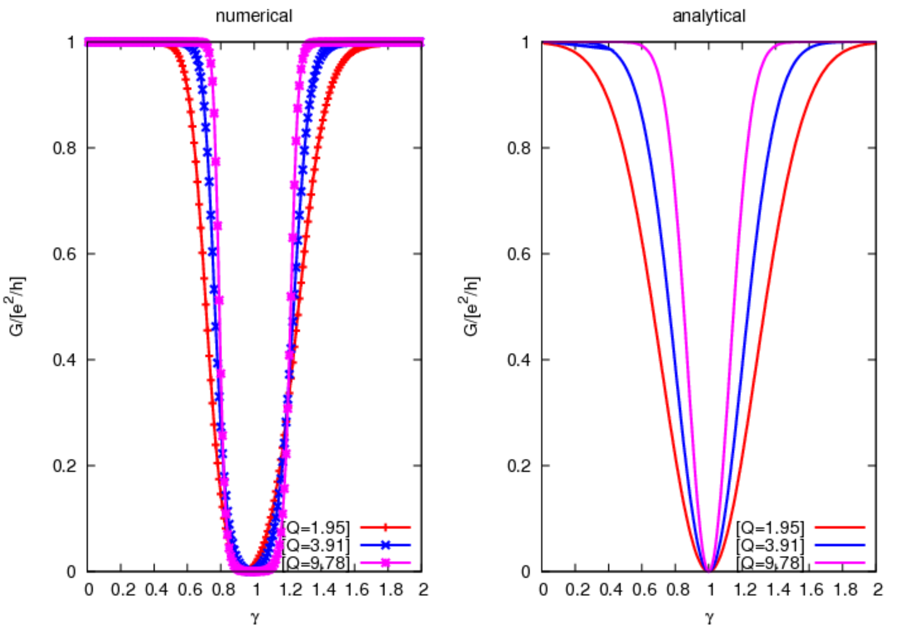

Figure 4.4: (numerical and analytical Landau-Zener transitions) Adiabatic transition probability of a waveguide with one spin polarized channel versus the normalized external field γ, indicating a reasonable agreement between exact calculations based on the recursive Green's function scheme (left) and the analytical transmission probability based on the Landau-Zener tunneling rate (4.26) (right) for different values of the adiabaticity parameter Q.

Next we apply the formula to a setup with a larger number of conducting channels $N = N_{\mathrm{Bg}} + \Delta$, where N_{Bg} denotes the number of channels which are responsible for the classical background of the current since they are transparent for both spin polarizations with respect to the $\hat{z}$-quantization axis.

The additional number of spin polarized channels Δ can be suppressed if the probability $P_{n,\sigma}$ is enhanced for each channel. Although the individual probabilities differ, with respect to the experimentally controlled parameter γ they possess minima at the same positions - at $\gamma = \pm 1$, while $\gamma = 0$ corresponds to fully adiabatic transport in the alternative situation. Note that described behavior with respect to γ is experimentally only observed, if spin evolution is adiabatic for optimum choice of γ. The latter is only ensured if a large value of Q is realized - which we achieve by utilizing giant Zeeman interaction.

4.4 Signatures of non-adiabatic transitions

The strong temperature dependence of the detectability of conductance minima at the adiabatic transition points - as shown in Fig. 4.5 a)- indicates the validity of our argument, since the n-d-interaction mediated giant Zeeman splitting is typically fragile with respect to increasing temperature [1]. In Fig. 4.5 b) we reproduce this effect in numerically computed magnetoresistance traces, using the RGF-approach [47], presented in paragraph 3.4.

Above discussion allows a comparison of the experimental data with the semiclassical summation formula for the overall magnetoconductance trace,

$$\frac{G}{e^2/h}(\gamma) = \sum_{(n,\sigma)\in\Delta(\gamma)} (1 - P_{n,\sigma}(\gamma)) + N_{\mathrm{Bg}}(\gamma), \tag{4.32}$$

and with numerical calculations of a model that includes spin structure.

Two important aspects follow from the ideas presented here.

The first aspect is the *detectability*.

All spin polarized channels are completely suppressed at $\gamma = \pm 1$, which will be the case if the stray field amplitude B_s and the external perpendicular field B coincide. This means that, given the conditions for adiabatic spin transport are otherwise met, we expect two minima in the total transmission at the critical fields $B_{C,+}$ and $B_{C,-}$, in agreement with the experiment [1].

This insight can be generalized to arbitrary textures of the magnetic field, where B_s is then replaced by the value of the out-of-plane component of the magnetic field, at which the longitudinal component of the stray field is locally zero.

We calculate realistic field textures micro-magnetically and compare the resulting values with the critical fields at which minima in the conductance were observed in Ref. [1]. In Figs. 4.5 and 4.6 we review the comparison of experimental, numerical and analytical results for a variety of setups presented in Ref. [1]. Described procedure shows remarkable agreement for a wide range

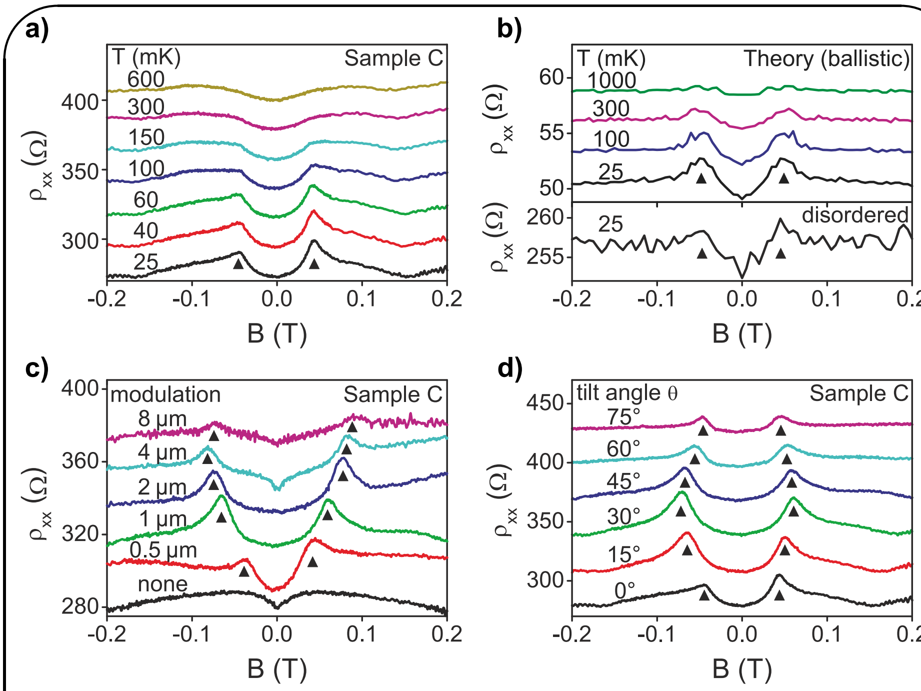

Figure 4.5: (typical experimental data and theory) Experimental (a,c,d) and numerical (b) figures published in Ref. [1] indicating signatures of non-adiabatic transitions of the spinor at critical values B_C of the externally applied magnetic field B. The black triangles indicate the values of B_C at which micro-magnetic simulations combined with our theory suggest conductance minima - or respectively - maxima in in the longitudinal resistance ρ_{xx}. Temperature variation (a) indicates that the observed phenomenon is caused by the spin structure and mediated by giant Zeeman interaction. We confirm this behavior for a numerical model system in (b). Experimental results upon variation of the distance between the Dy-stripes from 0.5 to 8μm in (c) as well as tilting the sample by different angles with respect to the direction of $\boldsymbol{B}$ (d) indicate a remarkable agreement with the theory discussed in the present chapter.

of performed experiments, including spatial variations of the period of the Dy-pattern - shown in Fig. 4.5 c) - and tilting the samples by arbitrary angles - as in Fig. 4.5 d) [1]. A summary on the data on changing the magnetic field orientation is shown in Fig. 4.6 a), in which theoretical and experimental values for the difference of the critical magnetic fields $\Delta := B_{C,+} - B_{C,-}$ show a striking agreement, including the symmetry with respect to $\theta = \pi/4$. The latter is consistent with the symmetry properties of the integral over the periodic magnetization density in the layer with the Dy-stripes [130]. In Fig. 4.6 b) we illustrate the temperature dependence of the relative resistance peak height, $\Delta\rho_{xx}/\rho_{xx}$, which is given by the difference of the longitudinal resistance at the critical field, and the resistance at zero magnetic field$\Delta\rho_{xx} = \rho_{xx}(B_C) - \rho_{xx}(0)$,

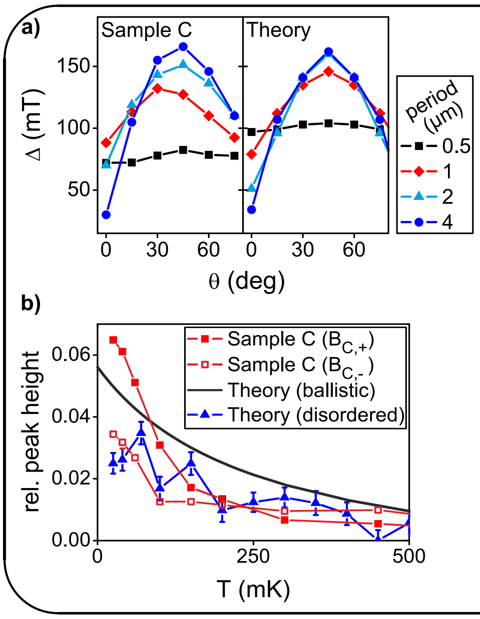

Figure 4.6: (comparison of theory and experiment) Measured and calculated anisotropy of the stray field $\Delta = B_{C,+} - B_{C,-}$ (a) and the relative resistance peak height $\Delta\rho_{xx}/\rho_{xx}$ (b) from Ref. [1]. In (b), for the theoretical model including disorder, the mean free path is $4\mu\mathrm{m}$ with respect to a cavity length of 18μm and a stray field modulation period of $1\mu\mathrm{m}$. We take as reference value ρ_{xx} the resistance in absence of giant-Zeeman splitting at 1 K.

normalized by ρ_{xx}, the resistance of a sample without giant Zeeman splitting. The line shape of the ballistic theory (solid black curve) is determined by the Brillouin-function in the formula for the effective g-factor (2.18), that enters our mean-field model of the Zeeman splitting. The found temperature dependence is a clear indication that the observed resistance peaks are related to the effect of the giant Zeeman splitting on the electronic spin [1]. Certainly the observation of the resistance dips in a large number of different experimental realizations of modulation periods and stripe widths rule out that the observed phenomenon originates from orbital effects of the periodically modulated magnetic fields, that can cause positive magnetoresistance if the field texture fulfills very specific requirements [141].

The second key aspect is, that our findings can be applied to *spin transport*.

The given setup provides a current with a well defined and rather large spin polarization, which ranges between 8 and 15$\%$ [1]. We showed that by tuning an experimentally accessible parameter γ the spin polarized part of a particle current can be entirely suppressed. This will happen if the critical field B_C is applied to the sample. This provides a means to switch spin polarization of a current on or off. Thus presented mechanism can be used in a building block of a spin logic device to manipulate spin via an external signal.

By numerical simulations of the proposed model in a system with a stray field amplitude B_s of 0.1 T and one period within the RGF approach we find a dip in the transmission for exactly $B = B_s$. We use the dimensionless quantity $\gamma = B/B_s$ in the respective Fig. 4.7. In our numerical framework we may also distinguish the different contributions to the total conductance, which can decomposed in terms of the transmission amplitudes associated with the processess to which a spin is subject, according to,

$$\frac{G}{e^2/h} = T_{\uparrow\uparrow} + T_{\downarrow\downarrow} + T_{\uparrow\downarrow} + T_{\downarrow\uparrow}. \tag{4.33}$$

Here by the first two quantities we denote the part of the transmission processes that preserve the spin that is initially in the state $|\uparrow\rangle$ or $|\downarrow\rangle$ with respect to the $\hat{z}$-quantization axis. The transmission probabilities with anti-parallel arrows correspond to processes that alter the spin after transmission through the sample. According to our theory presented above, only one of the spin diagonal contributions $T_{\uparrow\uparrow}$ or $T_{\downarrow\downarrow}$ give rise to a visible Landau-Zener conductance minimum at the critical magnetic field for which the non-adiabatic transition probability reaches its maximum. This is in good agreement with the numerical findings summarized in Fig. 4.7, in which only $T_{\uparrow\uparrow}$ experiences a transmission minimum that translates into the overall transmission. Note that upon increasing the magnetic field further, the value of $T_{\uparrow\uparrow}$ increases. This is caused by the enhancement of spin polarization by the increasing external field in the leads, as indicated by the increase of $\Delta(\gamma)$ in the lower graphic of Fig. 4.7. The reachable Fermi energies in our numerical models with system width of order 100 nm are small compared to the experimentally accessible values. Therefore, the squeezing out of channels due to Landau quantization is reflected more drastically in the total channel number $N(\gamma)$ as in the experiment this can mask the observation of the minima induced by non-adiabatic transitions of the spinor, as indicated by Fig. 4.7.

On the other hand, we find for small Fermi energies fully spin polarized systems with $N = \Delta$, in which the dip in the conductance is strongly pronounced. The realization of such devices hence would to operate with controllable fully spin polarized currents. Further numerical investigation shows, that the depth of the conductance dip relative to the total conductance decreases with increasing Fermi energies.

The current system is composed of 8 periods of the magnetic modulation. By calculating magnetoconductance traces for 1-32 modulations, we find that the position of the diabatic conductance dip at $\gamma = 1$ is not modified by a changed number of modulations. This is consistent with our semiclassical model. An increased modulation frequency however numerically indicates that around $\gamma = 1$ the minima are pronounced more sharply, which disagrees with our semiclassical summation formula (4.32). This behavior is expected, since in our analytical model we neglected interferences on length scales that exceed the period of one modulation. This is justified by the phase coherence lengths L_ϕ in the experiment, which are of the order of the periodicity. In the numerical setup however, the phase coherence length is replaced by the system length [64].

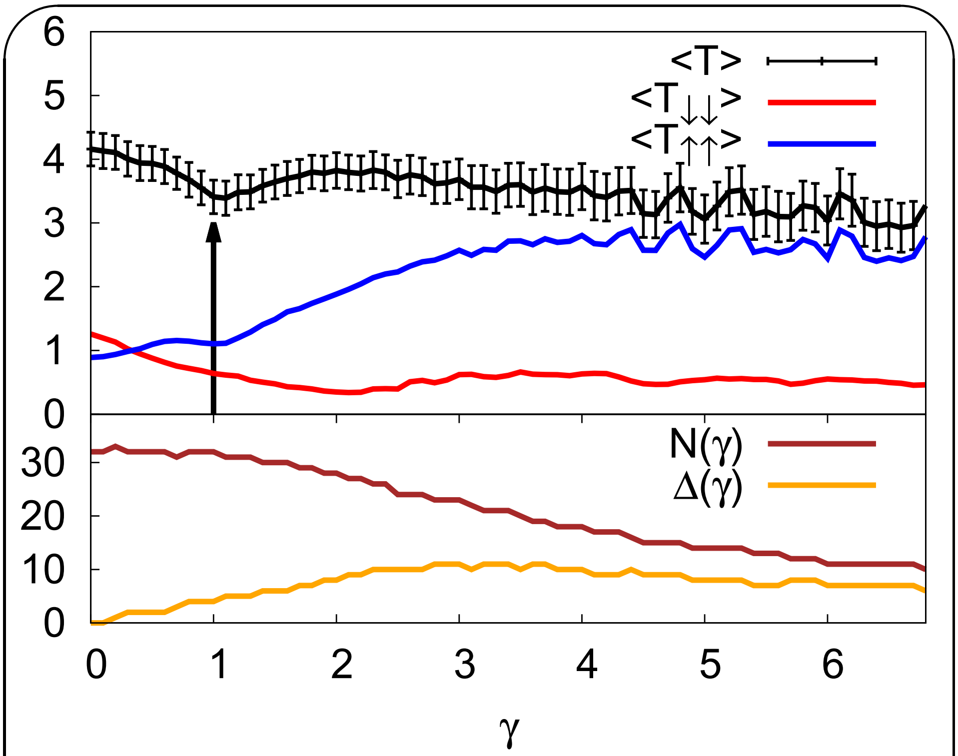

Figure 4.7: (numerical result for magnetotransport) Disorder average over 1000 impurity configurations of the total dimensionless conductance $T = G/(e^2/h)$ and the spin diagonal transmission probability $T_{\uparrow\uparrow}$, which displays a dip at $\gamma = 1$ of the stray field - external field ratio γ (upper plot) . The position of the minimum is consistent with our model for the helical magnetic field texture. (lower plot) Number of all channels N and spin polarized channels Δ, that change with variation to the external field, i.e. for changed parameter γ. Due to enhancement of the Zeeman splitting in the leads, Δ increases with γ. Because of Landau quantization, N decreases with γ. In the calculation we took $E_{\rm F} = 4$ meV, a system length of 5μ m, a width of 500 nm, an elastic mean free path of 500 nm, $g_{\rm eff} \sim 250$, 8 magnetic modulations and a stray field of 0.1 T.

Numerics thus indicate, that the minima at $\gamma = \pm 1$ are still observed for larger values of L_ϕ, although the line shape can no longer be predicted within our simplified model.

At roughly $\gamma = 3$, which corresponds to $B = 0.3\,T$, we observe the onset of the Shubnikov-de-Haas oszillations (SdHO) [54]. In the experiments, SdHO are used to determine the carrier density [54] and the additional beating pattern in the SdHO is used to determine the effective Zeeman splitting [1]. The magnetic field scales relevant for the picture of Landau-Zener transitions in spin space are typically much smaller.

Since a continuous magnetic field at the lead-cavity interface requires the presence of both stray field and external field inside the leads, the number of spin polarized channels is expected to change with variation of γ.

4.4.1 Orbital effects

For our numerical simulation shown in Fig. 4.5 b), the value of $m_\star$ is chosen as the effective mass of CdTe of approximately $0.1\ m_{\mathrm{e}}$. We neglect orbital effects induced by the magnetic vector potential in the kinetic energy term. This approximation will be valid if the cyclotron radius is much larger than the relevant length scales at magnetic fields of the order of the stray field amplitudes at which the conductance is measured [2].

To simulate transport of realistic systems of the experimental parameters of Ref. [1], with a model including orbital terms, we would need to consider high energy scales. The latter require a very fine discretization which is currently not accessible, even by utilization of parallel computing on a high performance cluster.

The modulation of the magnetic field is remote from the parameter range where it would effect the magnetoconductance correction such as discussed in Ref. [141].

A complication arises when we consider wide structures, in which orbital terms originating from the magnetic gauge field can no longer be excluded from our picture. The latter gives rise to Landau quantization and has an effect on background N_{Bg}, which manifests itself as a parabolic dependence of the transmission on the externally applied field. Numerical studies on models including orbital terms showed an enhancement of the observed conductance minima at critical magnetic field values, as we demonstrate in Fig. 4.8 and discuss in Ref. [2]. Note that the parabolic shape of the analytical data shown in Fig. 4.8 originates from standard perturbation theory, in which the first order correction of the orbital diamagnetic contribution to the Hamiltonian is considered [142]. However, the conductance minima of analytical and numerical calculations are found at identical values of B_C - which agrees well with the experimental results.

4.4.2 Disorder effects

The lower inset of Fig. 4.5 b) shows the result of our calculation in the presence of a small Anderson-like disorder with a mean free path L_{F} of 4$\mu\mathrm{m}$. The results suggest, that the adiabatic transitions should be observable in realistic systems, which typically are not ballistic. Interestingly, at the value $L_{\mathrm{F}} = 0.65\mu\mathrm{m}$, which is found in the experiments [1], the non-adiabatic conductance minima can no longer be observed. We attribute this point to the disorder model and

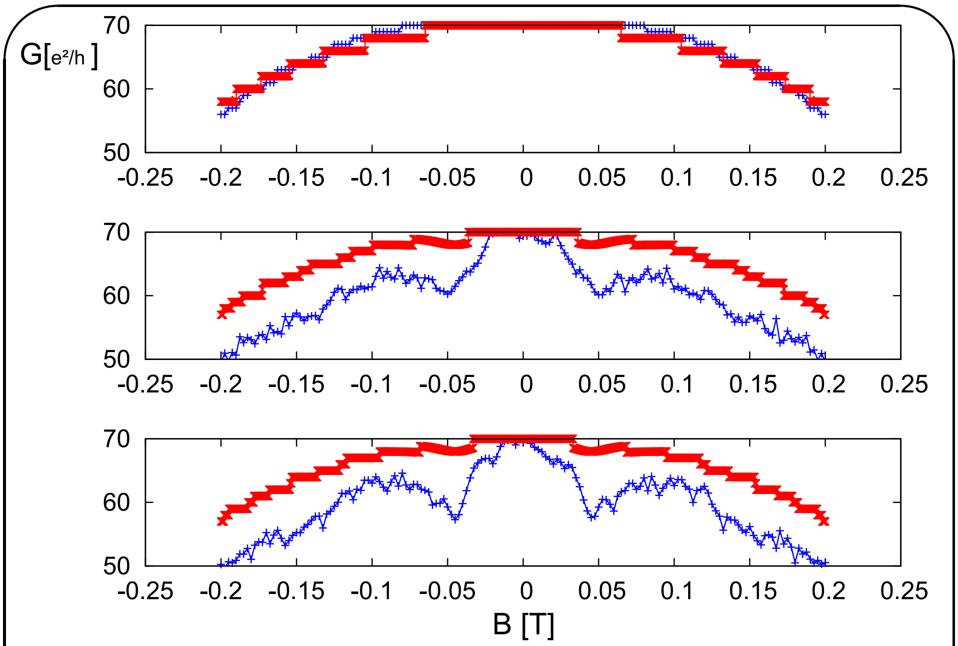

Figure 4.8: (numerical and analytical magnetoconductance) Adiabatic transition probability of a spin polarized waveguide with 70 open channels at zero external field. Orbital effects due to the external field B lead to the observed parabolic band banding. We compare the analytical prediction of Eq. (4.32) (red line) with the numerically obtained result (blue data points). The top panel corresponds to room temperature measurement, in which the giant Zeeman interaction is suppressed. The minima of the conductance at the critical field of $B_C = 45\ \mathrm{mT}$ appear at lower temperatures, such as 100 mK (middle panel) and are most pronounced at 25 mK (bottom panel). Present data have been reported in Ref. [2]. The calculated structure is a waveguide of 850 nm width and 4 repeated magnetic modulations of length $a = 1\mu\mathrm{m}$. We use $E_\mathrm{F} = 6.6\ \mathrm{meV}$ and an effective mass of $m_\star = 0.1\ m_\mathrm{e}$.

effects that arise due to the relatively large width of our implementation of the system.

There is an ongoing discussion on the impact of disorder on adiabatic processes involving spin transport [143]. In a one dimensional ring with angular dependent Zeeman splitting, Stern proposed in Ref. [144] that transport in a disordered ring remains adiabatic, if Berry's requirement to the adiabaticity parameter, $Q \gg 1$, is specialized to $Q \gg L/L_\mathrm{F}$, for a system of length L. In Ref. [143], Popp et al. present an alternative criterion that holds also for extended two-dimensional wires. Based on observation of Berry phase effects, Popp et al. state that $Q \gg \sqrt{\langle s \rangle}$ should be satisfied to establish adiabaticity. This formulation includes a relation to the number of scattering events $\langle s \rangle$. Although this criterion agrees well with Stern's earlier theory [144], we are not able to identify an according scaling behavior in our numerical transport experiments, since rescaling of Q would effect the width of the observed Landau-Zener transition but not the effective height of the peak-which is in contrast to Fig. 4.9. The calculations of Ref. [143] are performed in systems with inplane magnetic field components only. Contrasting to this situation, in our setup the orbital terms from out-of plane magnetic field contributions seem to be of increasing importance in the presence of disorder-as previously discussed [2]. Disorder introduces momentum scattering, which leads to the coupling of different channel numbers. For particles that are scattered into another channel, the effective adiabaticity parameter $Q_{n,\sigma}$ changes and our simplistic semiclassical picture breaks down [3] [2]. We illustrate this point in Fig. 4.9.

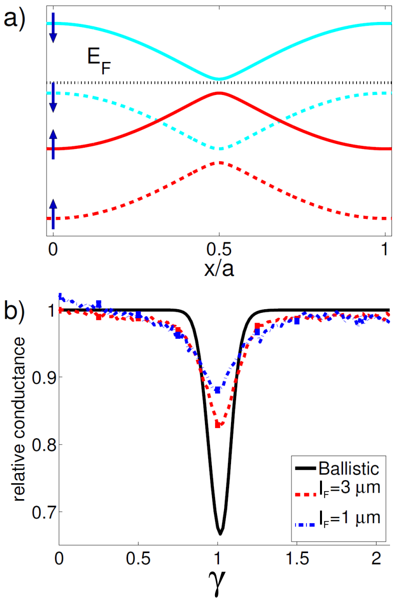

Figure 4.9: (disorder effect on diabatic transitions) (a) In a waveguide with many propagating modes, typically a number of orbital channels is spin polarized (solid curves) and the remaining channels are not polarized (dashed curves), since both Zeeman-split spin species have a kinetic energy below the Fermi energy E_{F}. The scattering by disorder allows orbital transitions from spin polarized to unpolarized channels, which perturbs adiabatic switching. (b) This is reflected in an enhancement of the conductance minimum at $\gamma = 1$ for diminished mean free paths l_{F} compared to the fully ballistic case (black curve). The waveguide consists of one magnetic modulation, is $a = 1\ \mu\mathrm{m}$ long and is operated at $E_{\mathrm{F}} = 8\ \mathrm{meV}$. The relative conductance shown is the ratio of the magnetoconductance including a modulated stray field with a finite stray field amplitude B_{s} and the magnetoconductance at B_{s}, under variation of the external field B. The figure is published in Ref. [2].

There are however many possibilities that allow to preserve the switching property of the diabatic transitions, i.e. being able to switch between zero and finite spin polarized current, despite the presence of significant momentum scatter-

---

[3] This can be further explained by the fact that a transition between different channels implies a discontinuity in the longitudinal velocity component $v_{n,\sigma}$, which enters into $Q_{n,\sigma}$.

ing,. An obvious example is given by (quasi-) one-dimensional wires, in which the same functionality is maintained, as the one-dimensional model device Datta and Das [21] proposed. This stability is due to transversal confinement creating the one-dimensional channel, which effectively fixes the transversal momentum component and thus the norm of the longitudinal velocity component entering our semiclassical model is conserved as well. A related momentum stabilization also leads to the suppression of Dyakonov-Perel spin relaxation in one-dimensional wires, as the spin precession axis is fixed [145]. This is confirmed by the numerical data presented in Fig. 4.10 a).

In addition, numerical results indicate that if all the conducting channels are spin polarized, operation as a spin transistor is also very robust against disorder. We show our results for a sample with 8 spin polarized channels and different values of the mean free path, including a shorter value of $750\ \mathrm{nm}$ in comparison to a modulation length of $1000\ \mathrm{nm}$ in Fig. 4.10 b).

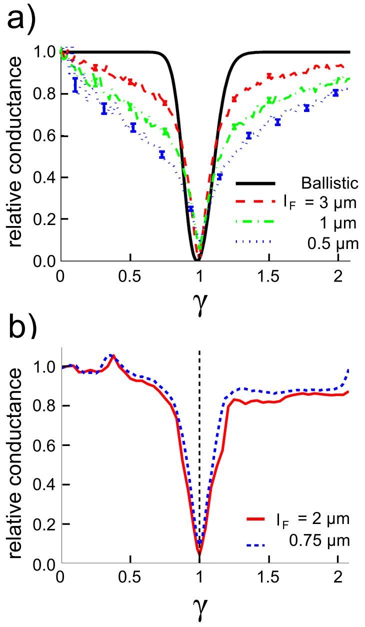

Figure 4.10: (diabatic switching in disordered transport) Disordered samples under variation of the normalized external field γ, in which it is possible to change between adiabatic transport of spin polarized currents at $\gamma = 0$ and blocked spin current at $\gamma = 1$. We consider $24\ \mathrm{nm}$ wide and $1\ \mu\mathrm{m}$ long samples with $g_{\mathrm{eff}} = 177$, $m_\star = 0.1\ m_e, B_{\mathrm{s}} = 0.12\ T$ and one magnetic modulation for different mean free paths l_{F} and calculate the relative conductance at (a) $E_{\mathrm{F}} = 6.6\ \mathrm{meV}$ and one spin polarized channel and at (b) $E_{\mathrm{F}} = 8\ \mathrm{meV}$ with 8 spin polarized channels at $\gamma = 1$. Although decreasing l_{F} destroys the typical Landau-Zener shape of the magnetoconductance, full blocking of spin polarized currents at $\gamma = 1$ is achieved in all examples. The figure is published in Ref. [2].

In the presence of a long range disorder potential, small angle scattering is dominant [126]. This type of scattering is characterized by a smooth correlation function and can be described well with semiclassical methods [126]. The fact that in Refs. [2] and [1] a decrease in the mean free path leads to an earlier breakdown of the signature of non-adiabatic spin evolution, may be explained by this. Note that the strength of the numerically implemented Anderson disorder enhances short ranged correlations [103]. A detailed study of a realistic model with a Gaussian disorder implementation could clarify this point but is beyond the scope of the present work.

4.5 Aspects on implementation in devices

Although the mechanism presented above allows for an easy and robust control of current spin polarization, it is a challenging task to translate our findings into technological devices that can be produced on a large scale.

- In our proposal we utilize the Zeeman field in order to generate an inhomogeneous effective magnetic moment. Giant Zeeman interaction is strongly temperature dependent. This implies that room temperature usage may not be achieved within our realization of the device. However, switching between non-adiabatic and adiabatic transport can be achieved by manipulating the parameter space of a Hamiltonian in a different way. For instance, the spatial inhomogeneity could be replaced by a temporal inhomogeneity. Note that the minimum requirements necessary to differentiate between the regime of diabatic and adiabatic transport are the large Q-factor on the one hand, and instantaneous eigenstates, that fulfill Berry's parallel transport requirement [138].

  Furthermore, experiments and theoretical studies suggest that the p-d exchange interaction in hole-type systems is more robust to increasing temperatures, than the s-d exchange interaction in Cd$($Mn$)$Te, which we currently use [62, 146]. Changing the device host material may thus be of advantage, as we show in the supplementary material to Ref. [1].

- Secondly, to apply our concept within a realistic device building block of small spatial extend, it would be helpful to switch between the diabatic and the adiabatic transport regime by changing external gate voltages rather than magnetic fields. Obviously the latter would be difficult to implement within a microstructure. A possible solution to this point is the application of spin-transfer-torque phenomena, in which magnetic moment within a material is altered by the flow of a (spin) current that can be electrically controlled [147]. Magnetic superstructures could for instance be realized by arrays of nanopillars, whose magnetization can be switched. Recent experimental findings indicate that such small magnetic memory elements can be controlled even by lateral currents [148] - which represents a significant step towards the realization of the proposed all electrical implementation of the device operation presented here.

Chapter 5

Spin relaxation in 2DEGs and 2DHGs with cubic SOI

In contrast to the example presented in the previous chapter, disorder usually has significant effects on the performance of a device, in which spin manipulation should be achieved [35].

In the present chapter, we will focus in particular on the quantum interference phenomena of weak localization (WL) and weak antilocalization (WAL), which are induced by disorder.

Our motivation is based on the fact, that recording WL and WAL phenomena under variation of experimental parameters can he used as a means to determine how well spin is preserved in a given setup [3, 4]. Our goal is ultimately to pinpoint conditions for spin preserving symmetries in various material types, using the relation of localization effects to spin relaxation. With this discussion we want to provide insight on concrete measurements [3] and suggest opportunities for future experiments [4] to access the spin degree of freedom in semiconductor based spintronics.

We investigate transport in samples with SOI contributions that scale cubically with the momentum. Such k-cubic terms in the SOI occur in the description of electrons confined to two dimensions - i.e. 2DEGs - in zinc blende crystal based quantum wells, and are even more relevant in the context of hole mediated charge transport in 2DHGs [1].

We use the following structure in the upcoming discussion:

- In order to motivate magnetoconductance measurements as probe for spin relaxation, we review the theory on WL and WAL phenomena.
- We afterwards review the main ideas of our contribution to Ref. [3], in

---

[1] In Chap. 2 we introduce the different systems including relevant works and references, that are not repeated here.

which we consider 2DEGs. Our main focus resides on the effect k-cubic SOI of Dresselhaus type on spin preserving symmetries.

- Furthermore, we apply the findings of Ref. [3] to 2DHGs which can be described by our model (2.40). In this class of materials, the leading order contribution to both Rashba [44] and Dresselhaus [45] SOI is known to scale cubically in the momentum. Although analytical as well as numerical modeling of these systems is challenging, we identify a spin preserving symmetry in this class of systems. Our main results from Ref. [4] are shown here.

5.1 Weak localization mechanism

Disorder, represented by impurity defects or lattice deformations, is present in typical realistic samples. Restricting ourselves to a mesoscopic conductor, we assume that scattering is elastic and is characterized by a transport time τ. To leading order the conductivity σ of a disordered sample with carrier density n_s, is determined by the Drude formula [52],

$$\sigma = \frac{\tau e^2 n_\mathrm{s}}{m_\star}. \tag{5.1}$$

The Drude formula is valid in the regime $k_\mathrm{F} L_\mathrm{F} \gg 1$ [85]. This condition for the Fermi wavenumber k_F and the mean free path L_F is the Yoffe-Regel criterion, which ensures that finite conductance is observed in a disordered system [98]. This can only be the case, if L_F is larger than the electronic lattice constant, which is proportional to k_F for electrons at the Fermi surface [98]. Only if this condition holds, also weak localization and antilocalization phenomena can be observed [85]. It contrasts the localized regime in a strong disorder potential [88] and is used in diagrammatic conductance calculations [149].

We obtain the result (5.1) from the Kubo formula for the conductivity [104], when we replace the disorder average of the two-particle Green's function by the independent averages of the separated Green's functions [52] [2].

The first approximation ignores correlations induced by the momentum scattering. This result oversimplifies the problem, which is indicated by the fact that in the diagrammatic result for Eq. (5.1), τ is incorrectly given by the elastic lifetime of a momentum state τ_el. The relevant timescale for the Drude formula should however be the transport time, which may deviate significantly from τ_el for scattering centers with anisotropic scattering cross section [52]. The mentioned discrepancy is corrected by considering correlations between the scattering

---

[2] The individual disorder average of a free particle Green's function can be calculated upon summation of geometric series of the dominant contributions to the Dyson equation [52]. This procedure leads to the broadening of the Green's function.

events. Of any conceivable realizations of Feynman diagrams that describe the scattering processes, only a few systematic combinations give rise to non-vanishing contributions [149]. These diagrams are of the type introduced by Langer and Neal [150]. The dependence of the conductivity on the transport time is correctly recovered after taking into account the ladder diagrams [52].

The second correction to the conductance is a manifestation of the maximally crossed diagrams, also referred to as the Cooperon diagrams [96, 108, 52]. A visual example of such a diagram is given in the top graphic of Fig. 5.1. This contribution to the conductance corresponds to weak localization or weak antilocalization - which are at the focus of the present chapter. A detailed presentation of the diagrammatic approach previously described can be found for example in the Refs. [52, 73, 149].

Here, we would like to discuss the weak localization phenomenon in an illustrative manner. For this purpose, we proceed with Bergmann's intuitive introduction of the underlying mechanism [90].

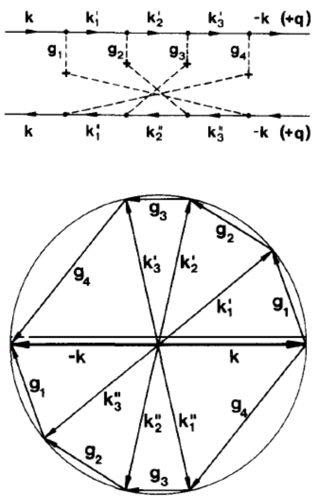

Figure 5.1: (corrections to the Drude conductance) Sketch from Ref. [90] indicating scattering processes in momentum space, that are related by time reversal symmetry. The top picture shows a diagram of the typical process. At the bottom the physical interpretation of the corresponding process in momentum space is depicted. Both pictures correspond to a particle with initial momentum $\boldsymbol{k}$, that is scattered into final momentum $-\boldsymbol{k}$. Wile the upper path corresponds to momentum exchange in the order $\boldsymbol{g}_1, \boldsymbol{g}_2, \boldsymbol{g}_3, \boldsymbol{g}_4$, the momentum change of the lower path is acquired in exactly reversed order, i.e. $\boldsymbol{g}_4, \boldsymbol{g}_3, \boldsymbol{g}_2, \boldsymbol{g}_1$. Both paths interfere constructively, contributing to an enhanced backscattering probability.

Let us focus on the momentum space paths that describe a particle that propagates in a disordered sample. In Fig. 5.1 we repeat the illustration of Ref. [90]. We consider paths [3] in which the particle has initial momentum $\boldsymbol{k}$, changes its momentum at each encounter with an impurity and eventually ends up in a state with opposite momentum $-\boldsymbol{k}$.

---

[3] By paths, strictly speaking we denote Feynman paths. We can construct the full propagator of a particle by summing all probability amplitudes of all these paths [151].

Provided time reversal symmetry is established in the experiment, each of these paths has a partner with exactly the same phase and amplitude. In the reversed partner path the interaction with each impurity takes place in reversed order and the particle ends up with final momentum $\boldsymbol{k}$

In a coherent system such path pairs have an enhanced probability relative to other occurring path combinations. To check this, we consider a process with amplitude A and another process with amplitude A'. The full probability of both processes is given by

$$|A + A'|^2 = |A|^2 + AA'^{\star} + A^{\star}A' + |A'|^2. \tag{5.2}$$

If A' and A are combined incoherently, the two products of different amplitude average out, giving rise to a total probability of $2|A|^2$. If the two paths possess identical phases, $A' = A$ consequently and the overall amplitude is given by $4|A|^2$ [90]. Enhanced backscattering probability leads to reduced transmission because of probability flux conservation. Weak localization hence decreases the overall conductivity. Since it requires phase coherence it is limited by the phase coherence length L_ϕ.

The corresponding conductance correction δG is given by

$$\delta G = -\frac{e^2}{\pi h} \ln \frac{L_\phi}{L_\mathrm{F}}, \tag{5.3}$$

in a two-dimensional conductor [108].

5.2 Position space approach to WL

Diagrammatically, the result (5.3) follows from momentum integration over the Cooperon kernel C, that contains the maximally crossed diagrams. In momentum space the Cooperon fulfills the relation,

$$\left[DQ^2 + \frac{1}{\tau_\phi}\right] C(\boldsymbol{Q}) \approx \frac{1}{\tau}, \tag{5.4}$$

with the diffusion constant D, the phase coherence time τ_ϕ and the composite momentum $\boldsymbol{Q}$ [52]. Interestingly, the position space representation of the solutions to Eq. (5.4) are solutions to the diffusion equation

$$\left[-D\boldsymbol{\Delta} + \frac{1}{\tau_\phi}\right] C(\boldsymbol{r} - \boldsymbol{r}') = \frac{1}{\tau}\delta(\boldsymbol{r} - \boldsymbol{r}'), \tag{5.5}$$

describing the time evolution of a diffusively propagating particle [52].

A Fourier transformation of the Cooperon thus yields the dependence of the conductance correction from WL, $\delta\sigma$, with the position space formulation of the Cooperon, $C(\boldsymbol{r}, \boldsymbol{r})$,

$$\delta\sigma \approx -\frac{2e^2 D\tau}{h} C(\boldsymbol{r}, \boldsymbol{r}). \tag{5.6}$$

The object $C(\boldsymbol{r},\boldsymbol{r})$ is the classical return probability of a diffusive particle. The WL conductance correction is proportional to the classical return probability - which is consistent with the finding in ballistic conductors or systems with smooth disorder, where a rigorous derivation of the conductance exists, based on Gutzwiller's semiclassical formulation of the Green's function and the application of ergodic sum rules [94, 92].

Note that $C = C(\boldsymbol{r},\boldsymbol{r}',E)$ is defined on a surface of constant energy E . Its Fourier transform in the time domain $W = W(\boldsymbol{r},\boldsymbol{r}';t_f,t_i)$ is described by the time dependent equation [108],

$$\left[\frac{\partial}{\partial t_f} - D\boldsymbol{\Delta} + \frac{1}{\tau_\phi}\right] W(\boldsymbol{r}-\boldsymbol{r}';t_f,t_i) = \delta(t_f-t_i)\delta(\boldsymbol{r}-\boldsymbol{r}'). \tag{5.7}$$

In their semiclassical approach, Chakravarty and Schmid establish the connection of the probability W with the conductance via the equation

$$\delta G = -\frac{4e^2 Da\tau}{h}\int \mathrm{d}t_0 W_{t_0}\chi(t_0). \tag{5.8}$$

which holds under the assumption that $t_0 \gg \hbar/E_\mathrm{F}$ for a thin film with thickness a and implies a cutoff function that limits the integration ranges to physically reasonable values for the time [108]. In Ref. [108], the function

$$\chi(t) = e^{-\frac{t}{\tau_\phi}} - e^{-\frac{t}{\tau}}, \tag{5.9}$$

is used, consistent with an upper limit that should be established by the phase coherence time and a lower cutoff realized by the fact that scattering should occur.

5.3 WL signature in magnetoconductance traces

Measuring WL represents a means to experimentally determine L_ϕ [152]. Identifying a behavior consistent with Eq. (5.3) does however not necessarily point to a localization phenomenon. This is due to the fact, that electron-electron interactions lead to a conductance correction of the same order of magnitude as (5.3), that also scales logarithmically with a temperature dependent timescale [99]. Consequently both effects are hard to distinguish from their temperature dependence alone.

Introducing a magnetic field to the setup however allows us to separate WL from other effects, since, in contrast to electronic interactions, WL has a characteristic dependence on the magnetic field [52, 108].

This is because of the connection with time reversal symmetry, which can be destroyed by exposing the conductor to a magnetic field B directed out of the plane to which transport is restricted.

Due to the presence of the field, both paths accumulate a phase difference from the magnetic vector potential that is included in their amplitude as an Aharonov-Bohm phase [153, 151]. This leads to a breakdown of weak localization. The reduction of to the conductance, δG, is usually obtained by taking the difference of the conductance of zero and a finite magnetic field,

$$\delta G(B) = G(B) - G(0). \tag{5.10}$$

An analytical expression for the explicit magnetic field dependence can be found by including the magnetic vector potential $\boldsymbol{A}(\boldsymbol{r})$ in the Fourier transformed Cooperon equation (5.7), which amounts to the expression,

$$\left[\frac{\partial}{\partial t_f} - D\left(\nabla - \frac{2i\boldsymbol{A}(\boldsymbol{r})}{\hbar}\right)^2 + \frac{1}{\tau_\phi}\right] W(\boldsymbol{r}-\boldsymbol{r}', t_f - t_i) = \frac{1}{a}\delta(t_f - t_i)\delta(\boldsymbol{r}-\boldsymbol{r}'), \tag{5.11}$$

where the factor 2 in the minimal coupling term arises from the fact that the derivative is performed on the coordinate $\boldsymbol{Q} = \boldsymbol{k} + \boldsymbol{k}'$, which is a composite of the single-particle momenta $\boldsymbol{k}$ and $\boldsymbol{k}'$. The constant a, which is assumed be significantly smaller than L_ϕ, is the thickness of the confinement in out-of-plane direction, since we consider transport in a two-dimensional medium.

Chakravarty and Schmid use the Landau gauge $\boldsymbol{A} = Bx\hat{\boldsymbol{y}}$, in which the solution of Eq. (5.11) can be formulated as

$$W_{t_0} = \frac{1}{a}\sum_n \int \frac{\mathrm{d}k}{2\pi}\psi_n\left(x' - \frac{\hbar k}{2eB}\right)\psi_n\left(x - \frac{\hbar k}{2eB}\right)\exp\left[ik(y-y') - \omega_n t_0 - \frac{t_0}{\tau_\phi}\right], \tag{5.12}$$

with the normalized eigenfunctions of the one dimensional harmonic oscillator ψ_n, corresponding to the eigenenergies $\hbar\omega_n = (2n+1)2eBD/\hbar$ [108]. The expression resulting from the momentum integration is given by

$$W_{t_0} = \frac{2eB}{ha}\sum_n \exp\left[-2\frac{eBD}{\hbar}(2n+1)t_0 - \frac{t}{t_0}\right], \tag{5.13}$$

which is inserted into Eq. (5.8) to yield the magnetic field dependence,

$$\delta G(B) = -\frac{e^2}{\pi h}\left[\psi\left(\frac{1}{2} + \frac{\hbar}{4eBD\tau}\right) - \psi\left(\frac{1}{2} + \frac{\hbar}{4eBD\tau_\phi}\right)\right], \tag{5.14}$$

with the Digamma functions ψ [154, 52, 108] [4]. Eq. (5.14) defines the characteristic line shape that predicts a minimum in the conductance - or a maximum in the resistance - at zero magnetic field, which decreases with increasing magnetic field. The phenomenon is hence called “negative magnetoconductance”, or equivalently, “positive magnetoresistance“. We present a typical result of a RGF transport simulation in a disordered sample in Fig. 5.2, which shows a

---

[4] For simplicity we give the conductance formulas for quadratically shaped samples, such that it coincides with the respective conductivity.

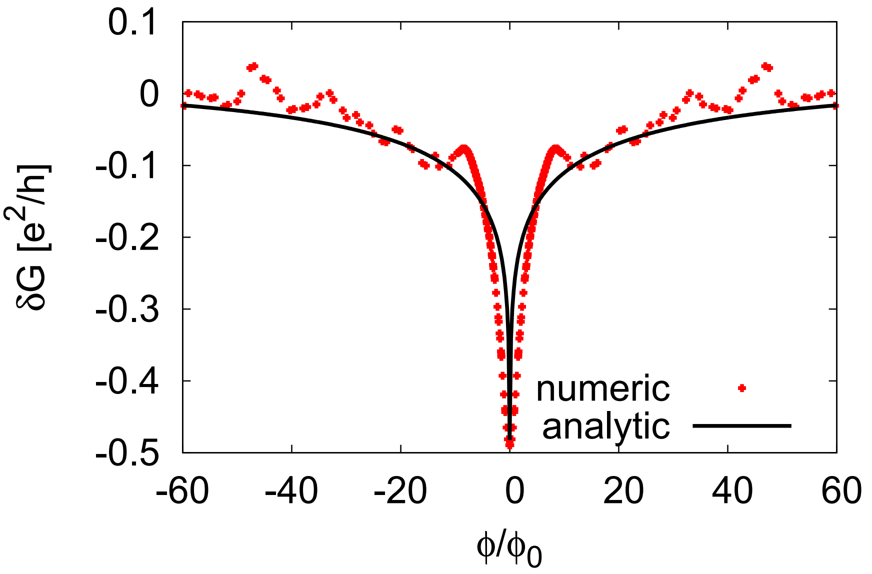

Figure 5.2: (WL signal) Typical conductance trace of a disordered sample, plotted with respect to the number of flux quanta ϕ/ϕ_0. The characteristic signature of WL is the minimum at zero magentic field. The numerical data result from averaging over 1000 disorder configurations in a system with $E_{\mathrm{F}} = 19$ meV, 100 nm width and 1μ m length, with L_{F} of 17 nm. (red points). We compare the RGF results with the analytical formula (5.14) based on the same system parameters (black curve), where we estimate L_ϕ by the value of L. The agreement between the two datasets is remarkable since no fitting is involved.

good agreement with Eq. (5.14) under the premise that we assume $L_\phi \approx L$. Strictly speaking L_ϕ would be infinite in our numerical calculations conducted at temperatures of $\Theta = 0$ K. Taking into account errors from the discretization, we estimate L_ϕ by the system length L and obtain τ_ϕ from it by the relation $L_\phi = v_{\mathrm{F}}\tau_\phi$. Since the sample does not have the shape of a square, we also need to multiply Eq. (5.14) with the factor W/L to obtain the conductance, where W is the system width.

So far in our discussion we have been ignoring effects of the spin degree of freedom on WL. We show in the next paragraph, that spin can induce a characteristically different magnetoconductance behavior, the weak antilocalization effect.

5.4 Weak antilocalization

Weak antilocalization (WAL) theory reveals the intrinsic relation of spin relaxation rates with measured magnetoconductance behavior.

Let us repeat the main message of the previous section - WL is reduced transmission due to the constructive interference of backscattered paths - that is destroyed by magnetic fields.

Extending diagrammatic frameworks for the calculation of the conductance correction, Hikami et al. predicted correctly that in materials with significant SOI, spin gets randomized by scattering, which leads to a destructive interference of backscattered paths - and hence - to an increase in conductance in the time reversal symmetric case [91].

Interestingly, a semiclassical calculation presented in Ref. [108], based on Eqs. (5.8) and (5.11), reproduces the diagrammatic result for the magnetoconductance in Ref. [91] exactly.

The main philosophy of the calculation is to consider all classical quantities of the previous discussion unchanged, and replace the return probability W_{t_0} in Eq. (5.8) by the quasi probability

$$\tilde{W}_{t_0} := W_{t_0} \langle\langle \sum_{\sigma} \sum_{r,r_-} \langle\sigma|\, \mathrm{D}_r \mathrm{D}^\dagger_{r_-}\, |\sigma\rangle \rangle\rangle_{\mathrm{Imp}}, \tag{5.15}$$

where $\langle\langle \ldots \rangle\rangle_{\mathrm{Imp}}$ denotes the average over impurity positions, r and r_- the classical configurations space paths that are related by time inversion and return to the initial position after time t_0. The objects $\mathrm{D}_r, \mathrm{D}_{r_-}$ are the corresponding spin propagators introduced in Eq. (3.56) [108]. Equation (5.15) is derived in the context of a disordered system. However, in the semiclassical approach to ballistic mesoscopic billiards, spin is included in a similar fashion and the conductance is proportional to an integral over the classical return probability multiplied with a spin modulation factor [94, 95].

We assume that the effective Zeeman field $\boldsymbol{\mu}(\boldsymbol{p}_r, \boldsymbol{q}_r)$ is a Gaussian distributed random quantity with the property

$$\langle\langle \left[\int_{t_0/2}^{t_0/2} \boldsymbol{\mu}(\boldsymbol{p}_r, \boldsymbol{q}_r) \cdot \boldsymbol{\sigma} \right]^2 \rangle\rangle_{\mathrm{Imp}} = \frac{t_0}{\tau_{\mathrm{so}}} \tag{5.16}$$

which introduces the phenomenological spin-orbit scattering rate τ_{so}.

The average over the products of the spin propagators can be simplified by expanding the dimensionality of the problem to the product space of spin and time-reversed spin operator. Upon inserting the basis states of a two-spin problem, Chakravarty and Schmid find that the singlet state $1/\sqrt{2}\,(|\uparrow\downarrow\rangle - |\downarrow\uparrow\rangle)$ lacks time dependence and is subtracted from the probability, while each of the triplet states contributes positively and decays exponentially [108]. This leads to the quasi probability,

$$\tilde{W}_{t_0} := W_{t_0}\frac{1}{2}\left[3\exp(-\frac{4t_0}{3\tau_{\rm so}}) - 1\right]. \tag{5.17}$$

According to Eq. (5.8) above expression is proportional to the conductance correction, which is negative for the case without spin. If the spin relaxation rate $1/\tau_{\rm so}$ is large, the spin is fully randomized and the triplet contribution is exponentially suppressed. The remaining term of the singlet has a negative sign- corresponding to a positive magnetoconductance. In the limit $1/\tau_{\rm so} \to 0$, corresponding to negligible randomization of the spin, one of the triplet terms cancels out the singlet term and a negative magnetoconductance correction of twice the magnitude of the WAL correction is measured. This relation of WL and WAL magnitude has been confirmed within random matrix theory [155].

A similar calculation can be performed in the presence of localized magnetic moments which are uncorrelated in space and time. The effect of the latter enters the spin flip rate $1/\tau_{sf}$. Combined with the previous result Hikami et al.'s formula

$$\delta G = -\frac{e^2}{2\pi h}\left[2\psi\left(\frac{1}{2}+\frac{1}{2\omega_0\tau}\right) - 3\psi\left(\frac{1}{2}+\frac{1}{2\omega_0\tau_{\rm tp}}\right) + \psi\left(\frac{1}{2}+\frac{1}{2\omega_0\tau_{\rm sg}}\right)\right], \tag{5.18}$$

is recovered [91].

As previously, we assume a quadratic sample. Here $\omega_0 = 2eBD/\hbar$ and the timescales due to spin orbit scattering $\tau_{\rm so}$ and scattering from local spins $\tau_{\rm sf}$ enter in the expressions

$$\frac{1}{\tau_{\rm tp}} = \frac{4}{3\tau_{\rm so}} + \frac{2}{3\tau_{\rm sf}} + \frac{1}{\tau_\phi} \quad \text{and} \quad \frac{1}{\tau_{\rm sg}} = \frac{2}{\tau_{\rm sf}} + \frac{1}{\tau_\phi}. \tag{5.19}$$

5.5 WAL in a 2DEG with k-cubic SOI

We investigate the realization of symmetries that preserve spin information. The latter are of major importance to spintronic devices, which are typically based on manipulating and reading spin information in a reliable manner.

Experimental verification by Koralek et al. of long lived spin states in ungated GaAs/AlGaAs quantum wells by optical detection methods represents a remarkable breakthrough in the context of spintronic research [39]. These long lived spin states are associated with the realization of the so called persistent spin helix (PSH) symmetry, that confines spin evolution to a particular topology [25, 38].

In the previous paragraph we have illustrated how spin relaxation is detectable in WAL signals. We showed how to arrive at Eq. (5.18) based on a phenomenological introduction of spin relaxation.

There exist however various analytical approaches to two-dimensional structures, in which a more accurate microscopic derivation of the relevant spin relaxation times are shown. These include the works of Pikus and Pikus [41], Knap et. al [42] and the alternative approach of Kettemann and Wenk [80, 81]. Mentioned works for electronic systems are based on the SOI structure, that is typical for zinc blende structure materials,

$$\boldsymbol{\mu}_{\mathrm{2DEG}}(\boldsymbol{k}) \cdot \boldsymbol{\sigma} = \boldsymbol{\mu}^{1}_{\mathrm{2DEG}}(\boldsymbol{k}) \cdot \boldsymbol{\sigma} + \boldsymbol{\mu}^{3}_{\mathrm{2DEG}}(\boldsymbol{k}) \cdot \boldsymbol{\sigma} \tag{2.25}$$

with Bychkov-Rashba and Dresselhaus contributions depending linearly on the momentum,

$$\boldsymbol{\mu}^{1}_{\mathrm{2DEG}} = \alpha \boldsymbol{k} \times \hat{\boldsymbol{z}} + \beta \left(k_x \hat{\boldsymbol{x}} - k_y \hat{\boldsymbol{y}}\right), \tag{2.27}$$

and the cubic Dresselhaus contribution,

$$\boldsymbol{\mu}^{3}_{\mathrm{2DEG}} = \gamma \left(-k_x k_y^2 \hat{\boldsymbol{x}} + k_y k_x^2 \hat{\boldsymbol{y}}\right). \tag{2.28}$$

5.5.1 Origins of spin relaxation

In the systems defined by above model, the Dyakonov-Perel mechanism (DPM) [156] typically represents the microscopic origin of spin relaxation [42].

In our discussion, DPM randomizes spin in the presence of momentum scattering [156]. Principally also electron-phonon and electron-electron interaction may lead to spin relaxation within the DPM [36]. These effects are however neglected here, since we ignore electronic interactions and consider the idealized limit of zero temperatures.

Since the spin precession axis $\boldsymbol{\mu}_{\mathrm{2DEG}}(\boldsymbol{k})$ depends on $\boldsymbol{k}$, each change of the momentum leads to a change of the spin precession axis and thus to randomization of spin polarization. The DPM is characterized by the linear relation between of the spin relaxation rate and elastic scattering time [42]. Within the Dyakonov-Perel picture, a larger scattering rate hence leads to a decrease in spin relaxation, which can be interpreted as an effect of motional narrowing [157].

Although DMP is the dominant source of spin relaxation relevant to our model, we include a brief summary of other types of spin relaxation.

- The Elliot-Yafet mechanism describes spin flip processes due to spin dependent scattering at impurities [158, 159]. In contrast to the DPM, the corresponding spin relaxation rate increases with increasing scattering rate [36].

- Within the Bir-Aronov-Pikus mechanism, spin relaxation is caused by exchange interaction of electrons and holes [160].

- We touch the subject of spin relaxation by magnetic impurities in the derivation of Eqs. (5.18) and (5.19). The corresponding scattering rate is proportional to the density of magnetic scatterers [36].
- For completeness, the hyperfine interaction of the nuclei in the crystal lattice leads to a inhomogeneous Zeeman field and therefore induces spin relaxation [35]

While k-cubic Dresselhaus terms have a minor effect on the optical measurements of Koralek et al. [39], they can be of increased importance for larger carrier densities or temperatures [3]. We are additionally motivated to contribute a theoretical discussion on k-cubic SOI by the fact that only a small fraction of the theoretical works on spin relaxation considers k-cubic SOI [101, 161, 162, 157].

5.5.2 Experimental and numerical magnetoconductance

Ref. [3] includes a detailed analysis of strain free InGaAs/InAlAs quantum wells with significant k-cubic contributions. Both optical and transport measurements are performed in the same samples. The optical techniques include the determination of the ratios of Rashba and Dresselhaus SOI by the circular photogalvanic effect (CPGE) and spin galvanic effect (SGE) [67]. While the optical methods are sensitive to the first harmonics of the SOI induced anisotropy in momentum space, we find that magnetoconductance measurements show an increased sensitivity on higher harmonics of the SOI anisotropy in this respect [3].

As opposed to optical measurement techniques, transport experiments as a probe to spin lifetimes has the major benefit that the latter can still be applied in gated samples, which may no longer be accessible to optical detection [64]. Note that the data presented in Ref. [3] represent the rare occasion in which SOI parameters are extracted by optical and transport measurements that are applied to the same sample. In fact, three entirely different experimental methods allow for a detailed comparison of the different techniques and an accurate description of the system type under investigation.

The constants in Eq. (2.27) are the linear Bychkov-Rashba [30, 31] coefficient α, and the linear Dresselhaus [32] coefficient β. The ratio of these coefficients, determines the relative strengths of the structural inversion asymmetry (SIA) induced SOI and the bulk inversion asymmetry (BIA) induced SOI respectively. The value of α/β can be determined by all of the applied measurement schemes, magnetotransport, CPGE and SGE. The term (2.28), which is proportional to the cubic Dresselhaus coefficient γ, is the k-cubic contribution of the BIA induced SOI. In a large number of previous experiments this term is typically neglected, since at small carrier densities it is usually dominated by the k-linear SOI [3].

In the absence of k-cubic SOI there is a particularly interesting regime of linear BIA and SIA parameters,

$$\alpha = \pm\beta, \tag{5.20}$$

in which spin relaxation is suppressed and WL instead of WAL is observed in a system with finite SOI and momentum scattering [42, 25]. Above criterion establishes a fundamental symmetry in the Hamiltonian, denoted persistent spin helix (PSH)-symmetry [38], and will occur repeatedly in the upcoming discussion.

In spin precession based spintronic devices, such as the Datta-Das proposal [21], large SOI - as the mechanism that drives device operation - is in advantage. On the other hand large SOI - as an origin of spin relaxation - is also problematic. Thus it would be of benefit to realize systems with large SOI and in the mean time suppress spin relaxation. This is, in brief, the reason why the PSH is of major interest to the spintronics community.

The strength of the SOI, in particular the contribution of BIA, can be influenced by choice of material. However, selecting a material constant that enhances k-linear BIA, also leads to an increased k-cubic BIA. This becomes clear when considering the definition of the linear Dresselhaus parameter [42],

$$\beta = \gamma \left\langle k_z^2 \right\rangle \approx \gamma \frac{\pi^2}{d_{QW}^2}, \tag{5.21}$$

which indicates a linear dependence on the cubic BIA parameter γ. The fabrication of a heterostructure sample with a specific quantum well width d_{QW} allows to influence the value of $\left\langle k_z^2 \right\rangle \approx \pi^2/d_{QW}^2$ [5]. Consequently the relative importance of linear and cubic contributions of the BIA induced SOI can be influenced by choice of the quantum well width, but can not be changed after the growth process. We therefore consider the overall BIA parameters fixed, while SIA induced Rashba SOI can still be altered by changing the voltage of an external top gate [33].

Note that the present discussion is neglecting electron-electron interactions and electron-impurity interactions, that have been considered in a discussion of the semiclassical spin diffusion equation in Ref. [157]. The authors of Ref. [157] arrived at the conclusion that the damping of the spin lifetimes in the PSH parameter regime is mainly due to SU(2)-symmetry breaking terms of the k-cubic Dresselhaus SOI or the electron-impurity interaction. Since in the experimental demonstration of the PSH [39] the electron-impurity interactions were of minor importance [157], we limit our discussion to effect cubic Dresselhaus SOI.

The transport measurements of Ref. [3] indicate a transition between WAL - associated with significant spin relaxation - and WL - associated with the ab-

---

[5] Here we assume a 2DEG forming in a symmetric hard wall confinement in which only the ground state is occupied.

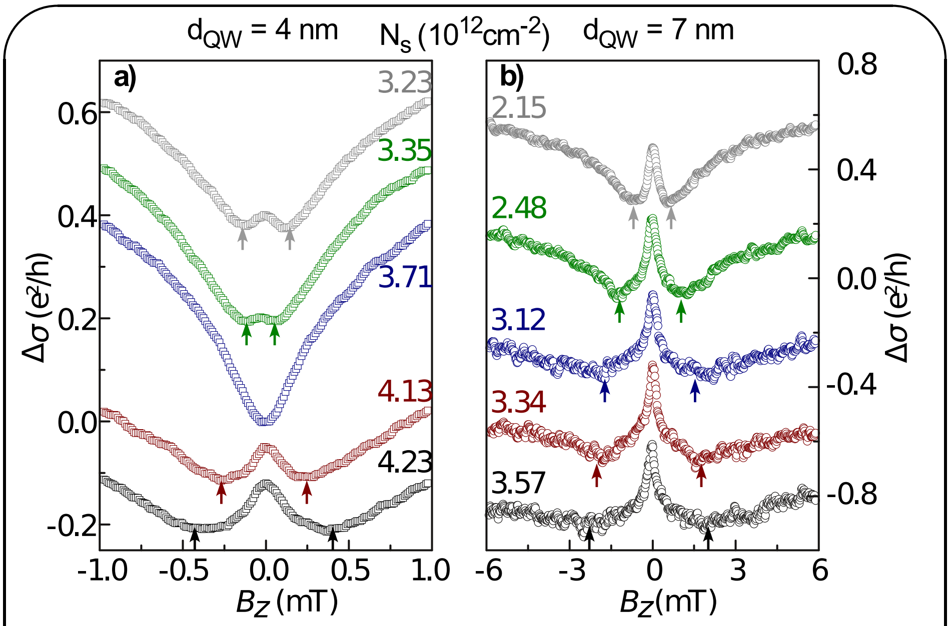

Figure 5.3: (2DEG: experimental WL and WAL line shapes) Plot of experimental magnetoconductance measurements, $\Delta\sigma(B) = \sigma(0) - \sigma(B)$, from Ref. [3], which shows of a 2DEG realized in a symmetric quantum well with depth $d_{QW} = 4\,\mathrm{nm}$ (a) and $d_{QW} = 7\,\mathrm{nm}$ (b) for different gate voltages that determine the respective charge carrier densities N_s. Changing the gate voltage leads to a change of the Rashba SOI. If the k-cubic corrections to the Dresselhaus SOI are small, the observation of WL indicates long lived spin states for special values of the Rashba coefficient (a). If the cubic corrections increase and/or the BIA and SIA SOI are not of equal magnitude, only WAL is measured, corresponding to a full randomization of spin information (b). The curves are vertically shifted by arbitrary values for increased visibility.

sence of spin relaxation - and back to WAL - under variation of the Rashba parameter for fixed Dresselhaus parameter.

This behavior can be seen in Fig. 5.3 from Ref. [3], which shows the results for a $\mathrm{In}_{0.53}\mathrm{Ga}_{0.47}\mathrm{As}/\mathrm{In}_{0.52}\mathrm{Al}_{0.48}\mathrm{As}$ quantum well (QW) of thickness $d_{QW} = 4\,\mathrm{nm}$ in (a) and another $7\,\mathrm{nm}$ thick QW in (b). The sample with the larger value of d_{QW} shows a larger dependence on the k-cubic SOI. This is indicated by the absence of WL in the measured magnetoconductance traces under variation of the external gate voltage and thereby the Rashba SOI strength. In other words, the observation of WAL in all curves depicted in Fig. 5.3 indicates spin relaxation, irrespective of the values of the Rashba SOI, since spin is always randomized by the Dresselhaus SOI in the system.

Note that in the experimental figure the charge carrier density N_s is given instead of the gate voltage value. The dependence between N_s and the gate voltage allows us however to estimate the corresponding Rashba parameters, since in a 2DEG the Rashba parameter α typically depends linearly on the gate voltage V_g [3].

In the sample with smaller d_{QW}, the linear Dresselhaus SOI dominates the cubic contribution. This behavior is expected from Eq. (5.21). The influence of cubic terms is visible as a shift of the parameters α/β where, according to Eq. (5.20), WL is observed in absence of cubic SOI, which would be at values of $\alpha/\beta = \pm 1$. In this parameter regime the cubic Dresselhaus SOI has the effect of a small, but not negligible perturbation, shifting the effective linear parameter β to a different value $\tilde{\beta}$ in Eq. (5.20). Consequently WL should be measured at a different value of α - and therefore at another gate voltage.

The design of the 4 nm sample was optimized in such a way, that in the ungated sample the condition $\alpha/\tilde{\beta} = 1$ is fulfilled. This is confirmed by optical measurements of the ungated sample. The SGE method yields a value of $\alpha/\tilde{\beta} = 0.98 \pm 0.08$ for the 4 nm sample at 5 K and $\alpha/\tilde{\beta} = 1.08 \pm 0.08$ at room temperature [3]. The CPGE result of $\alpha/\tilde{\beta} = 1.04 \pm 0.07$ at room temperature agrees very well with these findings [3].

The experimental data discussed here have been obtained in the groups of Sergey Ganichev and Dieter Weiss in Regensburg and the experimental group of Junsaku Nitta in Sendai.

At this point we still have to clarify how the value of $\tilde{\beta}$ is defined. Spin-galvanic and circular photogalvanic currents depend only on the first order harmonics in the Fourier expansion of the non-equilibrium electron distribution function [163, 164]. A Fourier decomposition of the SOI vector fields shows, that the contribution to the first harmonics, i.e. terms proportional to $\sin\varphi$ or $\cos\varphi$ of the polar momentum angle φ, includes not only linear SOI but also parts of the cubic SOI. Our experimental as well as theoretical findings indicate, that the magnetoconductance depends on higher order harmonics. In the experiment this feature is expressed by a WL signature at finite bias. This indicates, that the value $\tilde{\beta}$ relevant for optical experiments differs from the value found in transport measurements. We will now continue with a detailed analysis of the shift in the value of $\tilde{\beta}$ in transport experiments relative to optical measurements.

In Fig. 5.4 we illustrate this shift in a corresponding numerical model setup, for which we calculate the impurity averaged magnetoconductance correction δG, using the RGF approach from Ref. [47] and Anderson's disorder model introduced in Chap. 3. Furthermore we used periodic boundary conditions in transversal direction to imitate the bulk like character of the experimental samples, compared to which, a numerical unit cell is significantly narrower. If we fix the value of $E_{\mathrm{F}} = 19.5\ \mathrm{meV}$ and the effective mass to $m_\star = m_{\mathrm{e}}$, our setup is a disordered wire that is 80 nm wide in transversal and 150 nm long in longitudinal direction. The mean free path L_{F} of 17 nm is shorter than the periodically repeated transversal unit cell length, such that boundary effects and effects of the periodicity can be neglected. We fix the value of the linear BIA parameter $\beta = 23.1\ \mathrm{meV}$Å. This value is associated with a Dresselhaus spin precession length L_{so}^{β} of 33.3 nm. The spin precession length corresponding to linear BIA is defined by

$$L_{\mathrm{so}}^{\beta} = \frac{\hbar}{m\beta}, \tag{5.22}$$

which is the length scale of the spin precession for a Hamiltonian that only includes the kinetic term and the linear Dresselhaus-term $\beta\,(k_x\hat{\boldsymbol{x}} - k_y\hat{\boldsymbol{y}})$. L_{so}^{α} from SIA is found by replacing β by α in Eq. (5.22) [122]. A motivation for the expression (5.22) can also be found in the approximation of the spin propagator, presented in appendix A.7.

In systems with different types of SOI, it is usually not possible to find a constant expression for the spin precession length [117]. This can be explained by the anisotropy of the spin-orbit splitting for arbitrary combinations of the parameters α, β and γ.

By establishing a finite β in all sweeps with respect to the other SOI parameters, we attempt to ensure that the spin processes at least on a length scale of L_{so}^{β}, that is smaller than the wire width - in the present case the width of a periodically repeated unit cell in transversal direction. We use periodic boundary conditions because we want to model the two-dimensional bulk with our numerical setup. A spin precession length smaller that the width of the sample allows us to exclude the type of spin preservation discussed in Refs. [69, 80, 81, 145, 165], that occurs in quantum wires that are narrower than the relevant L_{so} and is confirmed by the observation of a positive conductance correction remote from the PSH parameter regime, as indicated by the characteristic WAL line shapes depicted in Fig. 5.4.

We choose L_{F} smaller than L_{so}^{β} to establish sufficient momentum relaxation for the spin to be randomized. At both ends of the wire the SOI is switched off adiabatically in order to avoid backscattering at effective potential discontinuities at the interface of lead and cavity.

5.5.3 Parameter regime of the WAL-WL-WAL transition

Motivated by the experimental and numerical findings, we will now address the question: For which combinations of SOI parameters do we expect a WL signal in a sample with finite SOI? This is of interest since such a signal, in contrast to a WAL magnetoconductance, points to the absence of spin relaxation.

The first interpretation in this context was given by Knap et al., who consider the Hamiltonian (2.25), in their diagrammatic calculation of the conductance

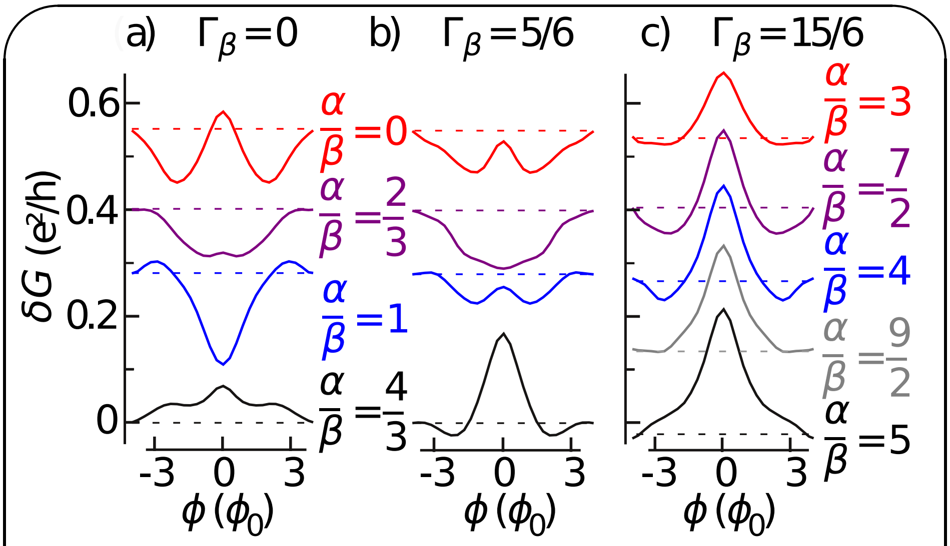

Figure 5.4: (2DEG: numerical WL and WAL line shapes) Figure from Ref. [3] which shows our numerically obtained disorder averaged magnetoconductance correction δG for various SOI ratios α/β from the interval $[0-5]$. The magnetic field is expressed in terms of the effective flux ϕ in the system normalized by the flux quantum ϕ_0. The strength of the cubic SOI is zero in a), takes intermediate values in b) and is further increased in c). We quantify its value with the parameter $\Gamma_\beta := k_\mathrm{F}^2\gamma/\beta$ for fixed β in all of the plots shown. Main result of our calculations is the observation of a transition from WAL to WL signal for $\Gamma_\beta = 5/6$ in b) at a shifted ratio $\alpha/\beta = \frac{2}{3}$, with respect to the realization of the exact spin preserving symmetry for $\Gamma_\beta = 0$ at a ratio of $\alpha/\beta = 1$ (a). Remote from values of $\alpha/\beta = \pm 1$ we only observe WAL (c). Plot b) and c) correspond to the experimental SOI parameter ratios of Fig. 5.3 a) and b) respectively. In a-c) all but the lowest curves are vertically shifted by arbitrary values for increased visibility.

correction. [42]. These authors arrive at spin relaxation rates that are proportional to momentum relaxation timescales, consistent with the Dyakonov-Perel spin relaxation [156]. Explicitly for the rates $1/\tau_{ij}$ that enter the equation for the average projection of the spin s in direction i,

$$\frac{\partial s_i}{\partial t} = -\frac{s_j}{\tau_{ij}}, \tag{5.23}$$

they identify the relaxation rates,

$$\frac{1}{\tau_{xx}} = \frac{1}{2\tau_{zz}} = 2\left(\mu_1^2\tau_1 + \mu_3^2\tau_3\right). \tag{5.24}$$

The scattering times are determined from the distribution function

$$\frac{1}{\tau_n} = \int \mathrm{d}\varphi\; W(\varphi)(1-\cos(n\varphi)), \tag{5.25}$$

with the probability $W(\varphi)$ of scattering by an angle φ [42]. The quantities μ_1 and μ_3 denote the Fourier coefficients corresponding to the first and third harmonics of the total spin-orbit field $\boldsymbol{\mu}_{\mathrm{2DEG}}(\boldsymbol{k})$, which is decomposed according to

$$\boldsymbol{\mu}_{\mathrm{2DEG}}^{1,\mathrm{R}} = \alpha k\,(\hat{x}\sin\varphi - \hat{y}\cos\varphi)\,, \tag{5.26}$$

$$\boldsymbol{\mu}_{\mathrm{2DEG}}^{1,\mathrm{D}} = -\gamma k(\langle k_z^2\rangle - \frac{1}{4}k^2)\,(\hat{x}\cos\varphi - \hat{y}\sin\varphi)\,, \tag{5.27}$$

$$\boldsymbol{\mu}_{\mathrm{2DEG}}^{3,\mathrm{D}} == -\frac{\gamma}{4}k^3\,(\hat{x}\cos 3\varphi + \hat{y}\sin 3\varphi)\,, \tag{5.28}$$

where the inplane momentum $\boldsymbol{k}$ is parameterized as

$$\boldsymbol{k} = k\cos\varphi\hat{\boldsymbol{x}} + k\sin\varphi\hat{\boldsymbol{y}}, \tag{5.29}$$

and we distinguish between the linear Rashba contribution $\boldsymbol{\mu}_{\mathrm{2DEG}}^{1,R}$ and the first harmonic of the Dresselhaus term $\boldsymbol{\mu}_{\mathrm{2DEG}}^{1,\mathrm{D}}$, which includes the fill k-linear Dresselhaus contribution and parts of the k-cubic terms. The full Fourier coefficients are hence related to the amplitudes by $\mu_1 := \sqrt{(\boldsymbol{\mu}_{\mathrm{2DEG}}^{1,\mathrm{R}})^2 + (\boldsymbol{\mu}_{\mathrm{2DEG}}^{1,\mathrm{D}})^2}$ and $\mu_3 := \sqrt{(\boldsymbol{\mu}_{\mathrm{2DEG}}^{3,\mathrm{D}})^2}$.

Knap et al. [42] approximate the integration kernel of the Cooperon in terms up to second order in τ/τ_ϕ, the group velocity and the spin orbit field. The matrix structure of the problem makes it however difficult to obtain closed expressions for the conductance correction. In Ref. [42], a summation formula is obtained that represents a analytical solution in the presence of cubic BIA, but is only valid, if one of the linear contributions to the SOI, either of BIA or of SIA type, can be neglected. The solution of Knap consists of a summation formula that is not included here. It reproduces an earlier result of Pikus and Pikus for cubic SOI and no linear SOI [41]. However, a solution for arbitrary combinations of SIA and BIA with linear and cubic momentum scaling is only achieved numerically. An important advance is this context was made by Glazov and Golub, who present a semi-analytical formalism to calculate the conductance correction for arbitrary superpositions of the different components of the SOI in Ref. [101].

In summary, we are however not aware of any closed analytical expression with which the experimental magnetoconductance measurements of Ref. [3] could be compared. Therefore, we do not pursue a diagrammatic approach here. We compare the experimental results with numerical results we obtain from the RGF algorithm and interpret our findings in the context of heuristic symmetry based arguments.

For the beginning, Eq. (5.27) suggests to treat the term $\boldsymbol{\mu}_{\mathrm{2DEG}}^{3\mathrm{D}}$ as a small perturbation and to consider instead of β, the rescaled linear Dresselhaus parameter $\tilde{\beta}$, defined by

$$\tilde{\beta} := \gamma(\langle k_z^2\rangle - \frac{1}{4}k^2) = \beta - \frac{1}{4}\gamma k^2, \tag{5.30}$$

where typically the approximation $k^2 \approx k_{\mathrm{F}}^2$ provides a reasonable estimate. Note that the given Fourier decomposition does not distinguish between k-linear and k-cubic terms. In particular contributions of the k-cubic terms to the linear harmonics μ_1 are of interest to the present discussion, since they are responsible for the observed shift in the parameter regime where a WL line shape is expected, despite the presence of finite SOI.

The rescaling of the BIA parameter $\tilde{\beta}$ according to Eq. (5.30) is in good agreement with the $\alpha/\tilde{\beta}$ values extracted from the data of the CPGE and SGE measurements [3]. This is explained by the fact that the currents in the optical experiments also depend only on the first harmonics of the SOI [164, 163].

The magnetoconductance traces however yield different results for the effective α/β ratios at which WL instead of WAL is observed.

To quantify the deviation from the prediction of Eq. (5.30), we perform a systematic analysis of magnetotransport in our disordered model system. We calculate magnetoconductance traces under variation of the β/α value for fixed nonzero α, shown in Fig. 5.5. For each curve the disorder averages are performed over 100 configurations. To show only the dependence of the conductance correction $\delta G(\phi)$ on the magnetic flux ϕ, we plot the difference

$$\langle G(\phi) - G(\phi_c) \rangle_{\mathrm{Imp}} = \delta G(\phi) - \delta G(\phi_c). \tag{5.31}$$

With $\phi_c = 6\ \phi_0$ we choose the reference flux ϕ_c sufficiently large to fully break time reversal symmetry, but smaller than values which would give rise to the onset of orbital effects. We fix the Rashba spin precession length at $L_{\mathrm{so}}^{\alpha} = 33.3\ \mathrm{nm}$ and sweep the parameter β, representing the second axis in our plots. The rest of the system parameters coincide the setup underlying Fig. 5.4. To estimate the effect of the cubic SOI, we fix γ as independent parameter in each of the calculations in Fig. (5.5), while we sweep β to obtain two parameter plots. Thus the parameters of Figs. (5.5) a-e) can be interpreted as results for different QW-thicknesses.

Note that proposed sweep of the BIA induced SOI is hardly experimental feasible. A sweep of the SIA parameter α for fixed β would be more realistic, since it can principally be realized by tuning of an external top gate [33]. However we calculate the conductance under variation of β for the sake of visibility of the PSH symmetry shift. We include a numerical sweep of α for fixed β in Fig. 5.8 for completeness. In contrast to the alternative routine, the shift approaches the origin of the α/β axis for increasing value of the cubic SOI. This makes it hard to identify the effective shift. Visible values are however in reasonable agreement with the theoretical estimate of the shift, including the described sign of the shift in parameter space.

It is helpful to introduce a dimensionless quantity that expresses the relative

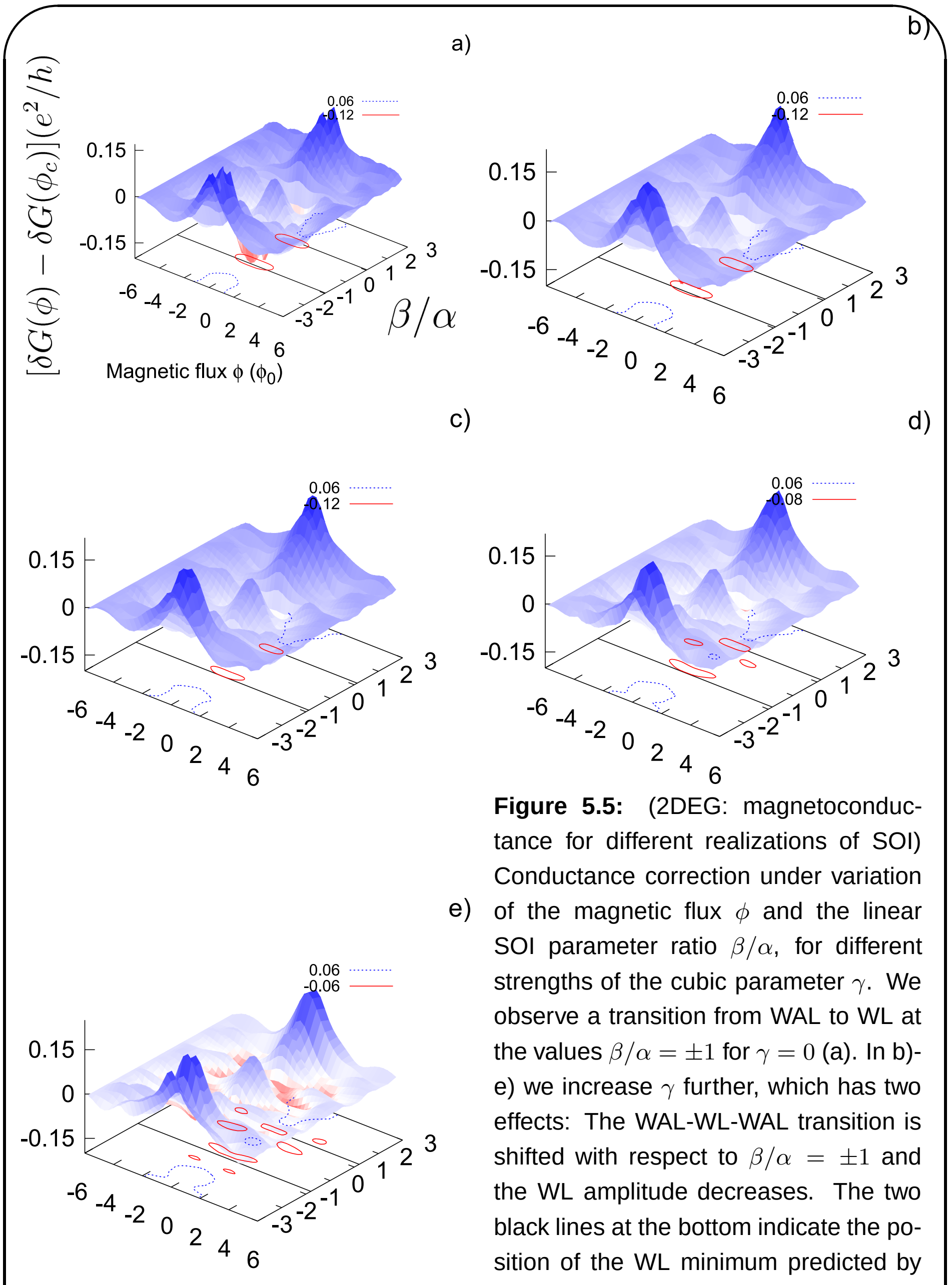

Figure 5.5: (2DEG: magnetoconductance for different realizations of SOI) Conductance correction under variation of the magnetic flux ϕ and the linear SOI parameter ratio β/α, for different strengths of the cubic parameter γ. We observe a transition from WAL to WL at the values $\beta/\alpha=\pm1$ for $\gamma=0$ (a). In b)-e) we increase γ further, which has two effects: The WAL-WL-WAL transition is shifted with respect to $\beta/\alpha=\pm1$ and the WL amplitude decreases. The two black lines at the bottom indicate the position of the WL minimum predicted by Eq. (5.33), which deviates from the numerical results for increasing γ.

strength of fixed cubic SOI and the fixed linear SOI. For this purpose we define

$$\Gamma_\alpha := \frac{k_\mathrm{F}^2\gamma}{\alpha}, \tag{5.32}$$

and, equivalently, Γ_β, for which we substitute α by β in Eq. (5.32). From the

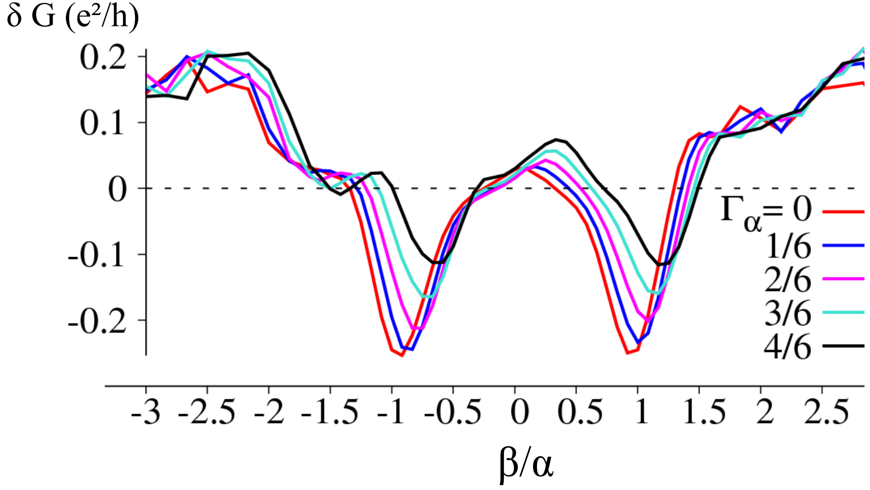

Figure 5.6: (2DEG: sweep of β/α at fixed α for different cubic SOI) Disorder averaged magnetoconductance correction of a rectangular scattering region with a length (L) to width (W) aspect ratio of 150:80 that is periodically repeated in transversal direction. The number of conducting channels per spin $k_\mathrm{F} W/\pi$ is 18, mean free path $L_\mathrm{F} \simeq W/2.29$ and fixed linear Rashba spin precession length $(L^\alpha_\mathrm{so})^{-1} = W/2.42$, while we sweep the parameter β/α for different values of cubic Dresselhaus interaction $\Gamma_\alpha = \gamma k_F^2/\alpha$ and observe a crossover from positive conductance corrections (WAL) to negative ones (WL). Here we change γ and leave k_F constant. The corrections result from subtracting the conductance G in the presence of an out of plane magnetic flux of $\phi_c/\phi_0 \simeq 6$ from the transmission in the time reversal symmetric situation, i.e., $\phi = 0$. This figure is published in Ref. [3].

PSH criterion $\tilde{\beta}/\alpha = \pm 1$ and Eq. (5.30), we would expect WL for the parameters

$$\frac{\beta}{\alpha} = \pm 1 + \frac{1}{4}\Gamma_\alpha, \tag{5.33}$$

which means that the ratios $\beta/\alpha =: \eta_\pm$ of the WAL-WL-WAL transition points,

$$\eta_\pm := \pm 1 + \frac{1}{4}\Gamma_\alpha, \tag{5.34}$$

are shifted along the β/α-axis with increasing cubic SOI and increasing carrier density. The shift is given by $0.25\,\Gamma_\alpha$. This is visualized for the different values of Γ_α, where we show the results for $\Gamma_\alpha = 0$ in Fig. 5.5 a), $\Gamma_\alpha = 1/6$ (b), $\Gamma_\alpha = 2/6$ (c), $\Gamma_\alpha = 3/6$ (d) and $\Gamma_\alpha = 4/6$ in e) respectively. We include the symmetry points predicted by Eq. (5.33) as two black parallel lines on the bottom of each figure. Although the formula captures the trend correctly, it fails to predict the quantitative value of the observed shift.

We confirm that the shift of the parameter regime leading to WL is significantly influenced by the third harmonics of the cubic SOI. This is achieved within a numerical simulation of a model system, in which we artificially switch of the third harmonics. The respective shift is exactly given by Eq. (5.33).

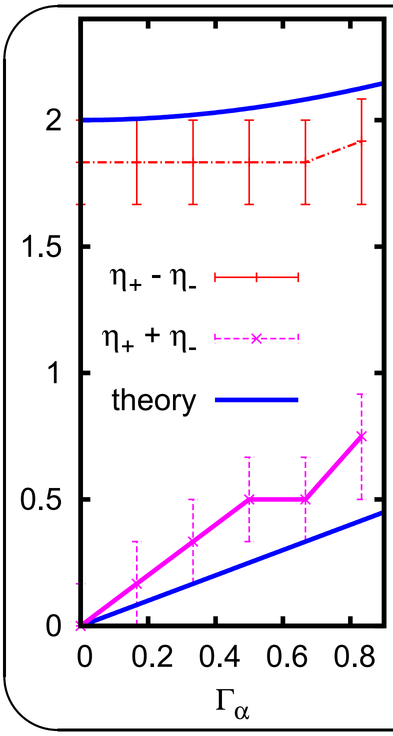

Figure 5.7: (2DEG: numerical and analytical WAL-WL-WAL transition) We extract the position of the numerical WL minima $\eta_\pm$ from Fig. 5.6 and plot $\bar{\eta}_+ - \bar{\eta}_-$ (red datapoints) and $\bar{\eta}_+ + \bar{\eta}_-$ (magenta datapoints) with respect to the rescaled cubic Dresselhaus SOI strength $\Gamma_\alpha = \frac{\gamma k^2}{\alpha}$. The predictions from Eq. (5.57) (blue lines) are compared with the results. The errorbars indicate the inaccuracy due to the finite gridsize of the values of $\bar{\eta}$. The numerical simulations show deviations from both arguments. The naive condition (5.34) agrees well with the data for small values of Γ_α. In fact Eqs. (5.57) and (5.34) produce the identical lower blue line. The trend of increasing $\bar{\eta}_+ + \bar{\eta}_-$ is however only captured by Eq. 5.57.

From the found values we we extract from the magnetoconductance traces the amplitude of the conductance correction, $\delta G := \delta G(0) - \delta G(\phi_c)$ and obtain the Fig. 5.6, which is also published in Ref. [3]. We use the corresponding data, to extract the positions of the minima η_+ and η_-, and compare them with the theory (5.34). The lower blue line in Fig. 5.7 corresponds exactly to the theoretical prediction of Eq. (5.34), the curve $\eta_+ + \eta_- = \frac{1}{2}\Gamma_\alpha$, while $\eta_+ - \eta_-$, which is given by a constant value of 2, is not included in the plot. Comparison with the numerical values, given by the magenta line for the extracted $\eta_+ + \eta_-$ and the red line for $\eta_+ - \eta_-$ shows a clear deviation of the numerical result from Eq. (5.34). A linear shift of the BIA according to $\beta/\alpha \mp 1 \sim 0.4\,\Gamma_\alpha$ fits the numerical data, which deviates significantly from the value $0.25\,\Gamma_\alpha$ [3].

In Ref. [64] a rescaling resembling Eq. (5.30) is put forward for effectively (quasi)-one-dimensional wires. Based on a naive argument an effective $\tilde{\beta}$ parameter in the presence of cubic SOI is introduced, which is given by

$$\tilde{\beta} = \beta - \frac{1}{3}\gamma k_{\mathrm{F}}^2. \tag{5.35}$$

This result lies between the value we obtain and the value associated with considering the first harmonics of $\boldsymbol{\mu}_{\mathrm{2DEG}}$ only. Mentioned rescaling property of Ref. [64] was investigated in the context of transport experiments in (quasi-)

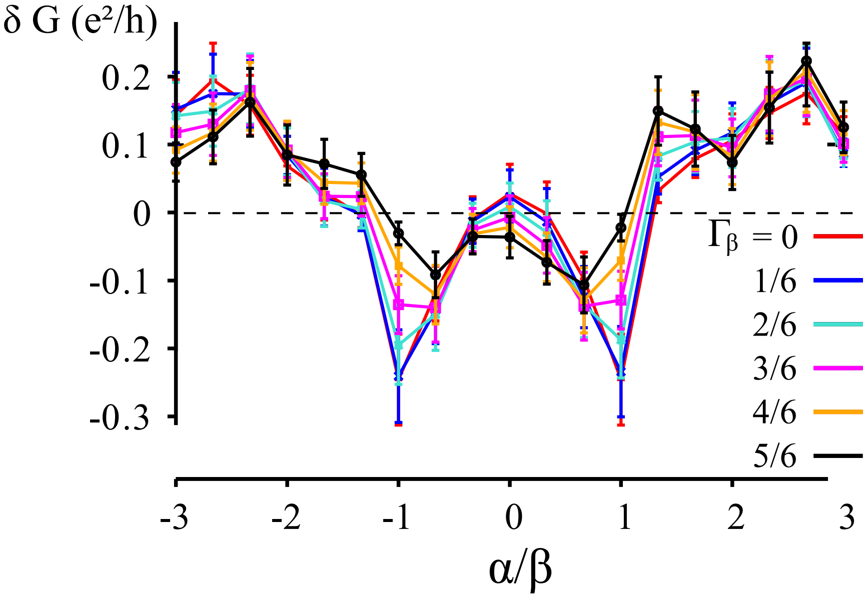

Figure 5.8: (2DEG: sweep of α/β at fixed β) Conductance correction traces with system parameters identical to the ones used in Fig. 5.6, here with fixed linear Dresselhaus spin precession length $k_\beta^{-1} = W/2.42$. We sweep the parameter α for different values of cubic Dresselhaus interaction $\Gamma_\beta = \gamma k_F^2/\beta$ and observe a crossover from positive conductance corrections (WAL) to negative ones (WL). The error bars indicate the standard deviation of the disorder average (100 configurations).

one dimensional wires with width W larger than $L_{\rm so}$ in the presence of an inplane Zeeman field [165]. In such systems the narrow transversal confinement gives rise to a U(1) symmetry of the Hamiltonian, which manifests itself in a WL signal [165]. An angular sweep of the inplane magnetic field however allows to switch between different realizations of spin preserving symmetries, that manifest themselves in a different amplitude of the WL signal [64]. The anisotropy of this WL amplitude [165], or analogously, of the universal conductance fluctuations [69], can be used to determine the ratio α/β experimentally.

Note that we obtain our quantitative result for a disordered wire with leads that support $N = 18$ channels per spin polarization, where N is defined by $N = \llcorner k_{\rm F} W/\pi \lrcorner$. More importantly, we choose $L_{\rm so} < W$, such that we observe WAL for $\alpha/\beta \neq \pm 1$. These two facts distinguish our setup from the one dimensional case and explain the deviation of our numerical finding from Eq. (5.35).

Furthermore, the deviation from the oversimplified approximation (5.34) increases for increased values of Γ_α. In the following chapter we will introduce a symmetry-based argument, which allows us to the derive both of the theoretical curves in Fig. 5.7. For the difference $\eta_+ - \eta_-$ our approach coincides with Eq. (5.34) and thus also fails to correctly describe the numerical result on this level. However, the upper blue line in Fig. 5.7 includes the slight increase of $\eta_+ + \eta_-$ with increasing Γ_α.

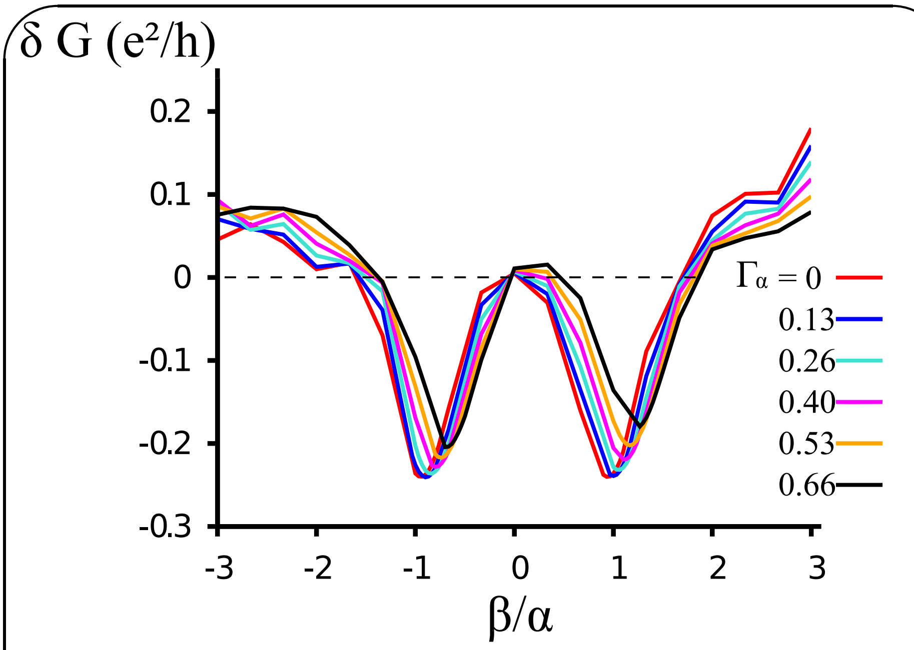

Figure 5.9: (2DEG: sweep of β/α at fixed α for different E_F) Averaged magnetoconductance correction of the previously investigated disordered sample, now for a smaller energy $E_\mathrm{F} = 15.6\ \mathrm{meV}$. The smaller we choose the value of E_F, the smaller the rescaled cubic parameter Γ_α gets. This is consistent with the observed shifts of the WAL-WL-WAL transition from the zero cubic SOI symmetry points at $\beta/\alpha = \pm 1$ (red curve).

Furthermore, we perform numerical calculations to investigate the energy dependence of the parametric shift of the WAL-WL-WAL transitions. According to Eq. (5.33), the WAL-WL-WAL transition follows the carrier density dependence of the quantity $\Gamma_\alpha = \gamma k_\mathrm{F}^2 \alpha$, for fixed γ and α. We show the result for $E_\mathrm{F} = 15.6\ \mathrm{meV}$ and otherwise unchanged system parameters in Fig. 5.9. In comparison to Fig. 5.6, here we observe a smaller difference of the WAL-WL-WAL transition points although the cubic Dresselhaus parameter γ is changed by identical values. This is consistent with the energy dependence of Eq. (5.33). This observation is in line our previous statement, that the influence of the cubic Dresselhaus term depends on E_F, or equivalently, the carrier density.

In the following we consider symmetries of the Hamiltonian for particular combinations of the SOI parameters α, β and γ. We interpret the effect of these symmetries on transport and spin relaxation.

5.6 Perspective on spin preserving symmetries

Symmetry considerations are a simple but effective method of predicting spin lifetimes in systems with spin-orbit coupling, described by a Hamiltonian H. Random matrix theory (RMT) is one possibility to predict properties of systems with given H, based on properties of Gaussian distributed random ensembles of matrices that belong to the same symmetry class [155]. For systems with k-linear SOI and Zeeman interaction, an extended analysis is given in the work of Aleiner and Fal'ko [166]. The properties of Gaussian ensembles are related to Gaussian circular ensembles, relevant for transport of chaotic systems [155] and thus allow statements on whether the conductance correction manifests itself as weak localization of or weak antilocalization [6].

Here we investigate the special case of a U(1) symmetry, based on the findings given in Ref. [25]. Key to this discussion is the discovery of conserved quantities. We have identified a nontrivial conserved quantity Σ, if it fulfills

$$[\Sigma, \mathrm{H}] = 0. \tag{5.36}$$

It is well known that an object that obeys permutation relation (5.36) allows for the introduction of a common eigenbasis of H and Σ, with which the Hamiltonian can be cast in block diagonal form [116].

For demonstration we assume to have an operator Σ with non-degenerate eigenstates $|\sigma\rangle$, for which

$$\Sigma\,|\sigma\rangle = \epsilon_\sigma\,|\sigma\rangle \tag{5.37}$$

holds. Now we multiply Eq. (5.36) from the left side with the eigenbra $\langle\sigma'|$ and the right side with the ket $|\sigma\rangle$ to obtain

$$0 = \langle\sigma'|\,\mathrm{H}\Sigma\,|\sigma\rangle - \langle\sigma'|\,\Sigma\mathrm{H}\,|\sigma\rangle = (\epsilon_\sigma - \epsilon_{\sigma'})\,\langle\sigma'|\,\mathrm{H}\,|\sigma\rangle\,. \tag{5.38}$$

To ensure that the right hand side of Eq. (5.38) is zero for arbitrary energies, the condition

$$\langle\sigma'|\,\mathrm{H}\,|\sigma\rangle \sim \delta_{\sigma\sigma'} \tag{5.39}$$

---

[6] Roughly speaking, while in the presence of a magnetic field the symmetry class of a chaotic system is given by the Gaussian unitary ensemble, in the time reversal symmetric case without spin-orbit coupling, the system is modeled by the Gaussian orthogonal ensemble, for which RMT predicts WL. In the time reversal symmetric situation with changing spin, which corresponds to the Gaussian symplectic ensemble, RMT predicts WAL [166]. In reality there are however a larger variety of situations, depending on the orientation and relative strength the effective magnetic moment that interacts with the spin. By introducing a gauge field with matrix structure, Aleiner und Fal'ko present a table that contains this information in Ref. [166]

must hold. This also illustrates how a block-structure is imposed on an Hamiltonian by the identification of a conserved quantity.
Up to sign and magnitude of the effective mass in the kinetic energy term, the structure of the Hamiltonian,

$$\mathrm{H} = \mathrm{H}_{\mathrm{kin}}\sigma_0 + \boldsymbol{\mu}\cdot\boldsymbol{\sigma}, \tag{2.25}$$

is identical for 2DEGs and 2DHGs considered in the present work. The effective moment $\boldsymbol{\mu}$ which couples to the spin degree of freedom, includes the SOI which is oriented in the xy-plane for the systems relevant to chapter. We assume further that Σ is constant and express it as superposition of the 2×2 unit matrix $\mathbb{1}_{2\times 2}$ and the Pauli matrices,

$$\Sigma = s_0\mathbb{1}_{2\times 2} + s_x\sigma_x + s_y\sigma_y + s_z\sigma_z = s_0\mathbb{1}_{2\times 2} + \boldsymbol{s}\cdot\boldsymbol{\sigma}. \tag{5.40}$$

Using the relations

$$[\sigma_i, \sigma_j] = 2i\sum_k \epsilon_{ijk}\sigma_k, \tag{5.41}$$

we obtain

$$[\Sigma, \boldsymbol{\mu}\cdot\boldsymbol{\sigma}] = 2i\boldsymbol{\sigma}\left(\boldsymbol{s}\times\boldsymbol{\mu}\right). \tag{5.42}$$

Thus Σ is conserved if $\boldsymbol{s} \parallel \boldsymbol{\mu}$ for arbitrary $\boldsymbol{\mu}$, which can only be fulfilled by a constant Σ, if $\boldsymbol{\mu}$ maintains a constant orientation,

$$0 \overset{!}{=} \frac{\partial}{\partial\varphi}\Theta = \left.\frac{\boldsymbol{\mu}\times(\partial_\varphi\boldsymbol{\mu})}{\boldsymbol{\mu}^2}\right|_z . \tag{5.43}$$

Conistent with Ref. [25], spin is preserved for a fixed spin precession axis $\boldsymbol{\mu}$, prohibiting Dyakonov-Perel spin relaxation [156], and momentum independent spinors, which suppresses Elliot-Yafet spin relaxation [158].

5.7 Connection of symmetries to transport

In Chap. 3 we show how to connect transport properties to the Green's function G. From Eq. (3.10) we infer a block diagonal representation of G with respect to the basis $\{|\sigma\rangle\}$, since

$$\mathrm{G}^{-1} = E - \mathrm{H} + i\eta \quad\rightarrow\quad \left[\mathrm{G}^{-1}, \Sigma\right] = 0, \tag{5.44}$$

follows from the relation (5.36). Assuming that an inverse exists, we get from

$$\mathrm{G}^{-1}\Sigma = \Sigma\mathrm{G}^{-1} \quad \text{to} \quad \Sigma\mathrm{G} = \mathrm{G}\Sigma, \tag{5.45}$$

and thus

$$[\mathrm{G}, \Sigma] = 0. \tag{5.46}$$

Analogous to the previous argument (5.39) follows

$$\langle\sigma'|\,\mathrm{G}\,|\sigma\rangle \sim \delta_{\sigma\sigma'}. \tag{5.47}$$

If we consider a typical Hamiltonian of a particle with spin, G becomes diagonal in the new basis. Let us apply this knowledge to transport of a two-dimensional system, if we find an operator Σ with eigenstates $\{|\sigma\rangle\}$ that are constant in momentum space.

5.7.1 Spin preservation in 2DEGs

In a 2DEG defined by Eqs. (2.25), (2.27) and (2.28), for the parameters $(\gamma = 0, \frac{\alpha}{\beta} = \pm 1)$, one finds the respective conserved quantities

$$\Sigma_{\pm} = \sigma_x \pm \sigma_y, \tag{5.48}$$

corresponding to the eigenstates

$$|\sigma\rangle = (1, \sigma\exp[\pm i\pi/4])^{\dagger}\ \text{[25]}. \tag{5.49}$$

The realization of this SOI parameter regime is persistent spin helix (PSH) symmetry [3, 25, 38].

To show the unique character of this symmetry, we specifically return to the electron SOI $\boldsymbol{\mu}_{\mathrm{2DEG}}$ from Eq. (2.26). The effective spin-orbit field is oriented in the xy-plane and depends on the inplane momentum $\boldsymbol{k}$, as sketched in Fig. 5.10.

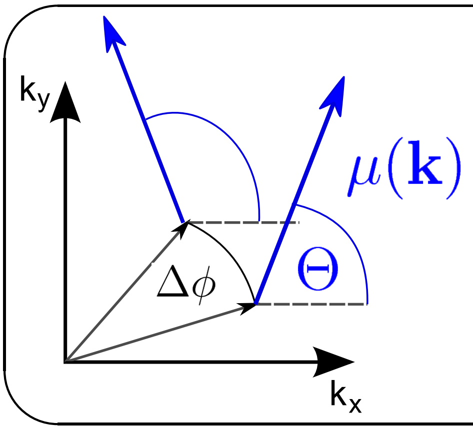

Figure 5.10: (SOI field orientation) Sketch of the effective SOI field $\boldsymbol{\mu}(\boldsymbol{k})$, which depends on the momentum $\boldsymbol{k}$. A change of the momentum direction $\Delta\phi$ by scattering leads to a change of the orientation Θ of $\boldsymbol{\mu}$ and thus randomizes the spin.

From the requirement that full spin orbit field

$$\boldsymbol{\mu}_{\mathrm{2DEG}} = \alpha\boldsymbol{k} \times \hat{\boldsymbol{z}} + \beta\left(k_x\hat{\boldsymbol{x}} - k_y\hat{\boldsymbol{y}}\right) + \gamma\left(-k_x k_y^2\hat{\boldsymbol{x}} + k_y k_x^2\hat{\boldsymbol{y}}\right), \tag{5.50}$$

has to be fixed in order to assert spin preservation, and by using $\partial_\varphi k_x = -k_y$ and $\partial_\varphi k_y = k_x$, we obtain

$$\partial_\varphi\boldsymbol{\mu}_{\mathrm{2DEG}} = \alpha\boldsymbol{k} + \left[-\beta k_y + \gamma(k_y^3 - 2k_x^2 k_y)\right]\hat{\boldsymbol{x}} + \left[-\beta k_x + \gamma(k_x^3 - 2k_y^2 k_x)\right]\hat{\boldsymbol{y}}. \tag{5.51}$$

Inserting above expressions into Eq. (5.43) leads to the condition,

$$0 \overset{!}{=} (\alpha^2 - \beta^2)k^2 - 2\alpha\gamma k_x k_y k^2 + \beta\gamma(k_x^2 - k_y^2)^2 + \gamma^2 k_x^2 k_y^2 k^2, \tag{5.52}$$

which is fulfilled if the Fourier decomposition of above equation vanishes within all harmonics in φ, given by

$$\left[(\alpha^2 - \beta^2)k^2 + \frac{1}{2}\gamma\beta k^4 + \frac{1}{8}\gamma^2 k^6\right] - \left[\alpha\gamma k^2\right]\sin 2\varphi + \left[\frac{1}{2}\gamma\beta k^4 - \frac{1}{8}\gamma^2 k^6\right]\cos 4\varphi, \tag{5.53}$$

from which we obtain the conditions

$$(\alpha^2 - \beta^2) + \frac{1}{2}\gamma k^2\left(\beta + \frac{1}{4}\gamma k^2\right) \overset{!}{=} 0, \tag{5.54}$$

$$\alpha\gamma \overset{!}{=} 0 \quad \text{and} \tag{5.55}$$

$$\left(\beta - \frac{1}{4}\gamma k^2\right) \overset{!}{=} 0. \tag{5.56}$$

For $\gamma = 0$ we recover the exact persistent spin helix symmetry found in the 2DEG at $\alpha = \pm\beta$ [25, 38]. Note that for the given Hamiltonian, there is no other combination of parameters that establishes an exact U(1) symmetry, since for $\gamma \neq 0$ Eq. (5.55) demands $\alpha = 0$ and Eqs. (5.54) and (5.56) can only be fulfilled either when $k = 0$ or $\gamma = 0$, which contradicts the initial requirement. For finite γ it is impossible to fulfill Eqs. (5.54) and (5.56) simultaneously. Knap et al. [42] however argue, based on the Fourier decomposition of the Cooperon, similar to the procedure used above, that the lowest harmonics in φ dominate the conductance correction of the system due to the angular distribution resulting from elastic scattering. Following this reasoning we consider the zeroth harmonic of the momentum, from which we find the approximate energy dependent symmetry

$$\beta = \frac{1}{4}\gamma k^2 \pm \sqrt{\alpha^2 + \frac{3}{16}\gamma^2 k^4}. \tag{5.57}$$

The previously shown results on transport under variation of β at fixed α agree well with Eq. (5.57), which we demonstrate in Fig. 5.7, where we show the theoretical values of $\beta/\alpha = \eta_\pm$ under variation of Γ_α as blue lines.
Now lets consider the effect of a PSH symmetry on transport.

5.7.2 Decomposition of the Landauer formula

As presented in Ref. [4], we decompose the total dimensionless conductance in the Landauer-Büttiker framework [105, 107] into a spin preserving transmission T_D and a complementary contribution T_OD,

$$\frac{h}{e^2}G = \sum_{n,m;\sigma=\sigma'} \left|t_{n,m}^{\sigma,\sigma'}\right|^2 + \sum_{n,m;\sigma\neq\sigma'} \left|t_{n,m}^{\sigma,\sigma'}\right|^2 =: T_\mathrm{D} + T_\mathrm{OD}, \tag{5.58}$$

where $\sigma, \sigma' = \pm 1$ are the quantum numbers of the previously introduced spin states, while n, m are integers that define the transverse channel of the in- and outgoing states due to a hard-wall confinement defining the edges of the leads, as shown in Chap. 3.

In terms of the structure provided by Eq. (5.58), T_{OD} vanishes if the spin orbit field $\boldsymbol{\mu}$ has a particular structure that allows the construction of the matrix Σ. This property suppresses spin scattering even in the presence of disorder [25]. When we evaluate the trace over the spin in Eq. (5.58) in the eigenbasis of the conserved quantity, or, equivalently, if we consider the in-plane spin orientation fixed along $\theta = \pm\pi/4$, we find that

$$T_{\mathrm{OD}} \propto \sum_{\sigma \neq \sigma'} |\langle \sigma | \sigma' \rangle|^2 = \sum_{\sigma \neq \sigma'} \delta_{\sigma,\sigma'} = 0 \tag{5.59}$$

is suppressed and T_{D} decomposes into two independent channels which give rise to a WL signal instead of WAL [42]. This is consistent with our numerical results presented previously.

5.7.3 Spin preservation in 2DHGs

The argument of the present section can also be applied to the 2DHG model (2.40) for the heavy hole sub-band, that includes perturbative coupling to the light hole sub-band in the presence of bulk and structural inversion asymmetry.

In mentioned context we identify the same conserved quantity as in the 2DEG, i.e. $\Sigma_{\pm} = \sigma_x \pm \sigma_y$, identical to Eq. (5.48).

In the hole model with neglect k-linear contributions,

$$\begin{aligned} \boldsymbol{\mu}_{\mathrm{2DHG}} =& \lambda_{\mathrm{D}} \left\{ -\bar{\gamma} k_{\mathrm{F}}^2 \boldsymbol{k} + \delta [k_x^3 \hat{\boldsymbol{x}} + k_y^3 \hat{\boldsymbol{y}} - 3 k_x k_y (k_y \hat{\boldsymbol{x}} + k_x \hat{\boldsymbol{y}})] \right\} \\ &+ \lambda_{\mathrm{R}} \left\{ \delta k_{\mathrm{F}}^2 (k_y \hat{\boldsymbol{x}} + k_x \hat{\boldsymbol{y}}) + \bar{\gamma} [-k_y^3 \hat{\boldsymbol{x}} - k_x^3 \hat{\boldsymbol{y}} + 3 k_x k_y \boldsymbol{k}] \right\}, \end{aligned} \tag{5.60}$$

we calculate in analogy to the 2DEG the conditions for a fixed spin precession axis and identify an exact symmetry if the system parameters fulfill the relations $\lambda_{\mathrm{R}}/\lambda_{\mathrm{D}} = \pm 1$ and $\bar{\gamma} = -\delta$, i.e., $\gamma_3 = 0$ simultaneously [4]. In these cases the direction of

$$\begin{aligned} \boldsymbol{\mu}_{\mathrm{2DHG}} \propto & [-k_{\mathrm{F}}^2 (k_x \pm k_y) \pm 3 k_x k_y (k_x \pm k_y) \\ & - k_x^3 \mp k_y^3](\hat{\boldsymbol{x}} \pm \hat{\boldsymbol{y}}), \end{aligned} \tag{5.61}$$

is fixed to the orientation of polar angles of $\pm\frac{\pi}{4}$.

We illustrate the fixed spin-orbit field $\boldsymbol{\mu}_{\mathrm{2DHG}}$ in Fig. 5.11 for the sub-bands of both spin polarizations [7] [4]. By engineering the quantum well width and choosing the electrical gate field appropriately one can reach $\lambda_{\mathrm{R}}/\lambda_{\mathrm{D}} = \pm 1$. However,

---

[7] In fact the structure of Eq. (2.40) implies an additional symmetry for $\bar{\gamma} = \delta$, which is however outside the range of validity of the perturbative derivation of the HH-model. The fact that $\gamma_2 = 0$ would be required shows this

in contrast to 2DEGs, in addition to this requirement, $\bar{\gamma} = -\delta$ must be fulfilled as well. Latter condition depends on Luttinger's parameters $\bar{\gamma} = (\gamma_3 + \gamma_2)/2$ and $\delta = (\gamma_3 - \gamma_2)/2$, which are intrinsic material properties.

A regime of enhanced spin lifetime established by the exact PSH condition is thus not easily accessible in arbitrary materials, There exists however the possibility to influence the effective values of γ_3, as indicated by Table C.9 in Ref. [53]. Another option to realize persistent spin evolution in holes consists of the utilization of strain [167].

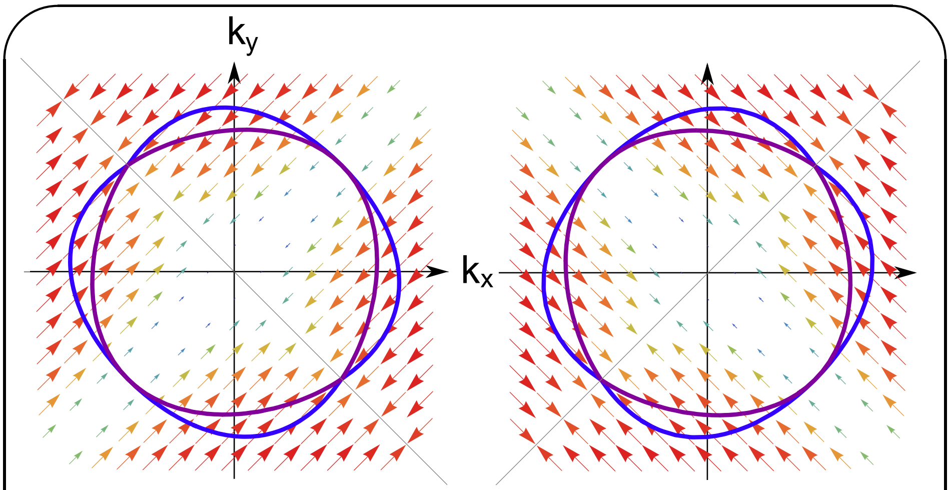

Figure 5.11: (effective spin-orbit field for heavy-hole PSH) Fermi surface for the different spin directions (violet and blue contour) and the corresponding direction of the effective spin-orbit field, μ_{2DHG}, illustrated by arrows. The SOI parameters establish a PSH for holes with uniaxial spin orientation corresponding to $\lambda_{\mathrm{R}}/\lambda_{\mathrm{D}} = +1$ (left) and $\lambda_{\mathrm{R}}/\lambda_{\mathrm{D}} = -1$ (right). In both cases the Luttinger parameters are $\bar{\gamma} = -\delta$, i.e., $\gamma_3 = 0$. This figure is published in Ref. [4].

In contrast to the role the k-cubic SOI plays in 2DEGs, namely that it prohibits the existence of an exact spin preserving symmetry, an exact PSH can, in theory, be achieved in 2DHGs. From our naive perspective, latter point suggests that large spin relaxation times corresponding to the PSH should be visible in HH gases, despite the presence of k-cubic SOI that is not merely a perturbation, but that represents the dominant term in the SOI Hamiltonian.

Numerical results consistent with our hypothesis. We illustrate this for the symmetry point at $\lambda_{\mathrm{R}}/\lambda_{\mathrm{D}} = -1$ and $\gamma_3 = 0$. In Fig. 5.12 a) we clearly see that upon variation of the ratio of Rashba and Dresselhaus SOI, η, we observe WAL for $\eta \neq -1$, which diminishes in amplitude when we approach the value $\eta = -1$, until we record a negative conductance correction. This trend is summarized in the the dependence of the conductance correction amplitude on the parameter η in Fig. 5.12 b), which indicates a smooth transition between the WAL

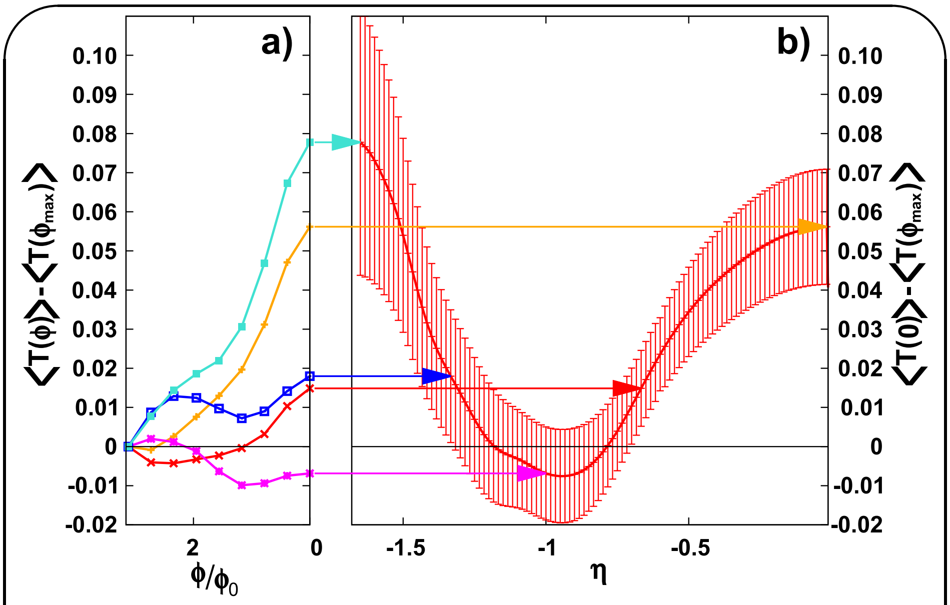

Figure 5.12: (2DHG: Magneto-transport analysis) Signatures of spin preserving symmetries in weak localization of a two-dimensional hole gas. (a) Disorder-averaged dimensionless magnetoconductance correction $\langle T(\phi)\rangle - \langle T(\phi_{\max})\rangle$ as a function of flux ϕ (in units of $\phi_0 = h/e$; $\phi_{\max}/\phi_0 = 3.1$) for spin-orbit coupling ratios $\eta = \lambda_{\mathrm{R}}/\lambda_{\mathrm{D}} = -1.65, -0.017, -1.33, -0.67, -1$ (from top to bottom). Here we use the transmission T, which is related to the conductance by $G = \frac{e^2}{h}T$.
(b) Conductance correction $\langle T(0)\rangle - \langle T(\phi_{\max})\rangle$ as a function of η. Negative magnetoconductance reflects suppression of spin relaxation close to $\eta = -1$. System parameters: Disorder average over 1000 impurity configurations for a scattering region of aspect ratio (length L to width W) 200:80 unit cells with periodic boundary conditions in transverse direction. Quantum transmission computed for $k_{\mathrm{F}}W/\pi = 13$ hole states per spin supported in the leads, elastic mean free path $l = 0.04W$, $\gamma_3 = 0$, and fixed Dresselhaus spin precession length $k_{\mathrm{D}}W \approx 1$. This figure is published in Ref. [4].

regime of spin relaxation and the WL regime without spin relaxation. Note that the magnetoconductance is used again to gain information on spin relaxation in two-dimensional HH systems, in analogy to our previous discussion on electronic systems. In the shown magnetotransport analysis we use the dimensionless conductance $G/(e^2/h)$, or transmission T in the respective axis labels.

In prior approaches based on the transport equations for spin and charge, only the cubic Dresselhaus term has been taken into account for hole gases, showing potentially a spin propagating mode that is however fragile in the presence of Coulomb interactions [168]. It could be an interesting aspect to perform further studies on the identification of spin modes in the hole gas, taking into account both k-cubic Rashba and Dresselhaus spin-orbit interactions [4]. Furthermore the application of the analytical diagrammatic theory of Refs. [80, 81] to transport in heavy-hole quantum wells described by the Hamiltonian (2.40) indicates parameter regimes of long lived spin states, in materials in which an exact PSH symmetry can not be achieved [4]. The respective calculation is beyond the scope of this work, but can be interesting to motivate optical experiments on hole gas samples, similar to the publications [39] and [40] on 2DEGs, since the spectral analysis of the Cooperon suggests long lived spin states at finite momentum excitations, that can be measured by optical techniques.

5.8 Spin transport analysis

In addition to considering the indirect influence of the PSH symmetry on the WL-WAL transition, it seems natural to search for a manifestation of a symmetry in T_D, Eq. (5.58), since its effects could be determined by magnetic polarization of the leads, allowing for spin transistor operation even in the presence of disorder [25]. Numerically we confirm the validity of the latter approach by calculating the normalized quantity $T_\mathrm{D}/(T_\mathrm{D}+T_\mathrm{OD})$. In Fig. 5.13 we show the results for 2DEGs and in Fig. 5.14 for HH-gases.

5.8.1 Numerical results

In 2DEGs, using identical system parameters as in Fig. 5.6, we observe for all realized values of the cubic spin-orbit interaction a clear cut peak in the diagonal transmission close to the shifted symmetry point in the parameter space, associated with the PSH symmetry. The numerical results are summarized in Fig. 5.15 a) and are fitted to a qualitative Landau-Zener model in Fig. 5.15 b), which we introduce in the following. The colored arrows in Fig. 5.15 a) mark the positions of the transmission maxima indicated by our analytical model, which agree remarkably well with the numerical peak positions. Note that although a fitting procedure is necessary to match the line shapes of the analytical approach to the numerical data, the position of the peaks is fixed by the chosen parameters for the different contributions to the SOI. Consequently the present approach is a reliable method to identify the position of enhanced spin lifetimes in a non-localization measurement. Individual disorder configurations have the same structure as the averages shown here, which indicates that the nature of the measured effect is not an interference phenomenon, such as WL or WAL, but a direct influence on the Drude conductance.

In 2DHGs the transmission as a function of $\eta := \lambda_\mathrm{R}/\lambda_\mathrm{D}$ in the basis corresponding to the $+\pi/4$ spin orientation, shows a maximum even if the exact PSH type symmetry is not realized. In the given example we chose the Luttinger parameters $\gamma_2 = 1$ and $\gamma_3 = 0.25$ which correspond to such a non-ideal setup. For parameters far from $\eta = 1$ the spin transmission is equally distributed among the diagonal and off-diagonal channels. The corresponding data is shown in Fig. 5.14. The length scale associated with spin precession is defined as

$$k_\mathrm{D}^{-1} = \left(\lambda_D k_\mathrm{F}^2\right)^{-1}. \tag{5.62}$$

Note that numerical limitations due to the discretization of the grid we are limited to a system width that is slightly larger than k_D^{-1}. This does however not lead to a dimensional suppression of WAL [81, 80, 145], because k_D^{-1} would only coincide with the spin precession length if it originated from only one SOI

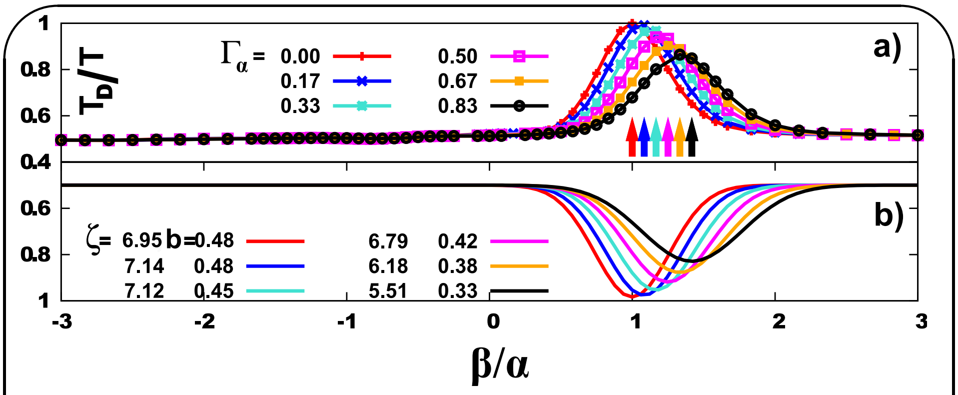

Figure 5.13: (2DEG: spin diagonal transmission) (a) Ratio of disorder averaged diagonal transmission over total transmission $\langle T_\mathrm{D}\rangle \,/\, \langle T\rangle = \langle T_\mathrm{D}\rangle \,/\, \langle T_\mathrm{D} + T_\mathrm{OD}\rangle$ which is found numerically for different values of the cubic SOI Γ_α and otherwise identical system parameters as in Fig. 5.6. (b) Analytical results from fitting our analytical Landau-Zener to the numerical data. The parameters of the fits include ζ, which renormalizes the momentum scattering time and b, which accounts for the decreased amplitude of the transmission compared to the Landau-Zener formula. The colored arrows in a) mark the peak positions predicted by our qualitative model, which are not subject to any fitting degree of freedom and are in excellent agreement with the numerical data.

contribution in the Hamiltonian. The Hamiltonian (2.40) however contains several terms proportional to k_D, such that we can assume that the actual spin precession length is significantly smaller.

5.8.2 Qualitative model

When $|\eta|$ approaches unity, T_D qualitatively corresponds to the probability of diabatic Landau-Zener transitions in momentum space, that take place between the instantaneous eigenstates

$$|\pm\boldsymbol{\mu}\rangle = \begin{pmatrix} 1 \\ \pm\exp[i\arctan\left(\mu_y/\mu_x\right), \end{pmatrix} \tag{5.63}$$

of the spin-orbit contribution, using Berry's parametrization [169]. The eigenenergies corresponding to these states are given by

$$\boldsymbol{\mu}\cdot\boldsymbol{\sigma}\,|\pm\boldsymbol{\mu}\rangle = \pm E_\sigma(\boldsymbol{\mu})\,|\pm\boldsymbol{\mu}\rangle\,, \tag{5.64}$$

with

$$E_\sigma(\boldsymbol{\mu}_\mathrm{2DEG}) = \sigma\tilde{Q}_\mathrm{2DEG}\left[1+\eta^2+\eta(2-\Gamma_\beta)\sin 2\varphi+\frac{\Gamma_\beta}{2}\left(\frac{\Gamma_\beta}{4}-1\right)(1-\cos 4\varphi)\right]^{\frac{1}{2}}. \tag{5.65}$$

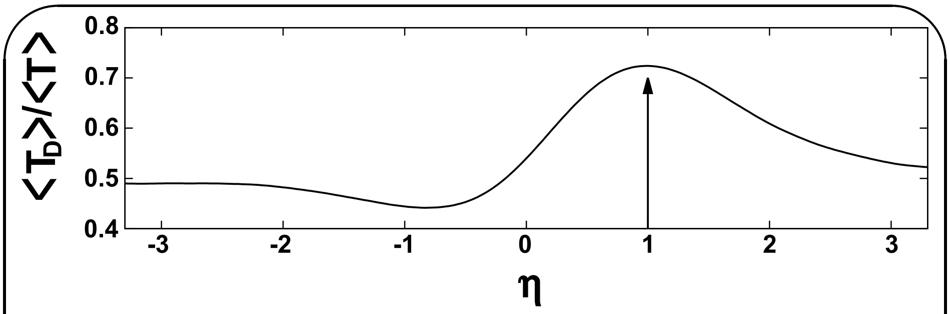

Figure 5.14: (2DHG: Spin diagonal transmission) Ratio of disorder averaged diagonal transmission over total transmission $\langle T_{\mathrm{D}}\rangle \,/\, \langle T\rangle = \langle T_{\mathrm{D}}\rangle \,/\, \langle T_{\mathrm{D}} + T_{\mathrm{OD}}\rangle$ as a function of η for a scattering region with 150:80 aspect ratio for fixed Dresselhaus spin precession length $k_{\mathrm{D}}^{-1} = 1.3\ W$ and Luttinger parameters $\gamma_2 = 1$ and $\gamma_3 = 0.25$ for which no exact spin preserving symmetry can be established. The peak of $\langle T_{\mathrm{D}}\rangle \,/\, \langle T\rangle$ at $\eta = 1$, coincides with the maximum of the diabatic transition probability of Eq. (5.73) (indicated by the arrow). Average Transmission shown includes 1000 disorder configurations. With respect to the eigenbasis of $\eta = -1$, we obtain a curve that coincides with the mirror image of the shown plot, that displays a maximum at $\eta = -1$. These results are published in Ref. [4].

Here we consider a 2DEG with with fixed β and introduced the effective adiabaticity parameter

$$\tilde{Q}_{\mathrm{2DEG}} = |k\beta| \,, \tag{5.66}$$

$\sigma \in \{\pm 1\}$, $\Gamma_\beta = k_{\mathrm{F}}^2\gamma/\beta$ and the ratio $\eta := \alpha/\beta$. As before, the inplane momentum orientation is given by $\varphi = \arctan\left(\frac{k_y}{k_x}\right)$. If we fix α and change β, as in Fig. 5.13, we use the alternative definition

$$E_\sigma(\boldsymbol{\mu}_{\mathrm{2DEG}}) = \sigma \bar{Q}_{\mathrm{2DEG}} \left[1 + \bar{\eta}^2 + (2\bar{\eta} - \Gamma_\alpha)\sin 2\varphi + \frac{\Gamma_\alpha}{2}\left(\frac{\Gamma_\alpha}{4} - \bar{\eta}\right)(1 - \cos 4\varphi)\right]^{\frac{1}{2}} , \tag{5.67}$$

with

$$\bar{Q}_{\mathrm{2DEG}} = |k\alpha| \,, \tag{5.68}$$

$\Gamma_\alpha = k_{\mathrm{F}}^2\gamma/\alpha$ and $\bar{\eta} := \beta/\alpha$.

For a 2DHG we find the dispersion

$$E_\sigma(\boldsymbol{\mu}_{\mathrm{2DHG}}) = \sigma \tilde{Q}_{\mathrm{2DHG}} \left[1 + 2\eta \sin 2\varphi + \eta^2\right]^{\frac{1}{2}} \tag{5.69}$$

with the adiabaticity parameter

$$\tilde{Q}_{\mathrm{2DHG}} = \frac{1}{4c_{\mathrm{D}}} \, |k|^3 \, (2 + 3c_{\mathrm{D}})\lambda_{\mathrm{D}}, \tag{5.70}$$

the ratios of the Luttinger parameters $c_{\mathrm{D}} = (2\gamma_3 - \gamma_2)/\gamma_2$ and $c_{\mathrm{R}} = -(2\gamma_3 + \gamma_2)/\gamma_2$, and the ratio of cubic Rashba parameter λ_{R} (2.43) and cubic Dresselhaus parameter λ_{D} (2.42), $\eta = \lambda_{\mathrm{R}}/\lambda_{\mathrm{D}}$.

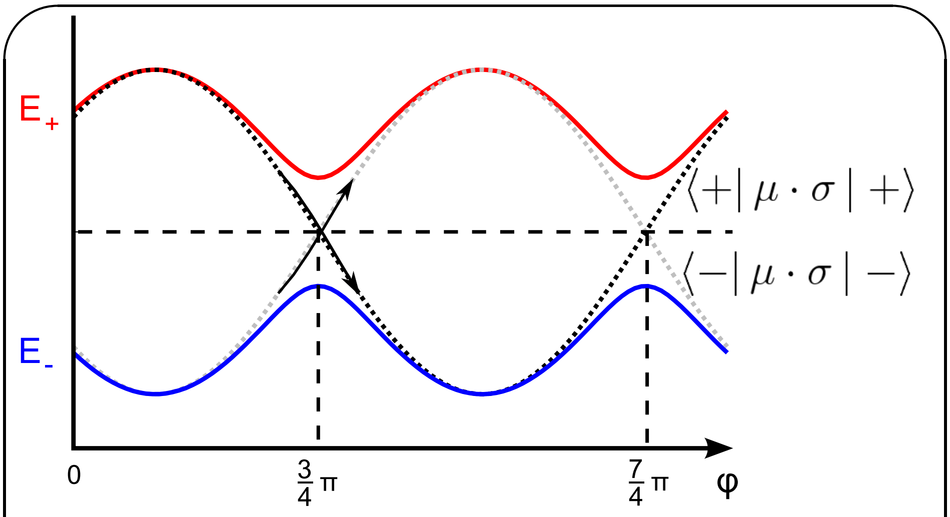

Figure 5.15: (2DEG: Landau-Zener transitions in momentum space) Anisotropy of the instantaneous eigenenergies of the spin-orbit Hamiltonian $\boldsymbol{\mu}\cdot\boldsymbol{\sigma}$ (solid curves) in a 2DEG with linear Rashba (α) The dotted curves correspond to the matrix elements $\langle\pm|\,\boldsymbol{\mu}\cdot\boldsymbol{\sigma}\,|\pm\rangle$ in with respect to the PSH eigenbasis $\{|\pm\rangle\}$ along the crossings at which azimutal momentum direction $\varphi = \frac{3}{4}\pi$ and $\varphi = \frac{7}{4}\pi$ diabatic transitions (black arrows) are induced, that reflect in the diagonal transmission T_{D}.

Note that the extrema in the dispersion of the 2DEG and the 2DHG SOI are found at the angles $\phi = \frac{(2n+1)\pi}{4}$ for $n \in \{0, 1, 2, 3\}$. We will be focusing on the minima of the dispersion, since these represent the anticrossings in momentum space, at which Landau-Zener [48, 49] tunneling occurs. Depending on the SOI parameters, we have to identify the nature of the extrema. For example in the 2DHG we find the minima in the dispersion are at the critical angles $\varphi_{c,1} = \frac{3\pi}{4}$ and $\varphi_{c,2} = \frac{7\pi}{4}$ for positive η and at $\varphi_{c,1} = \frac{\pi}{4}$ and $\varphi_{c,2} = \frac{5\pi}{4}$ for negative η. Although there are more cases in a 2DEG with cubic SOI, the physical situation is similar. For example in Fig. 5.15 we show typical 2DEG spin splitting (red and blue curve), which is minimal at the angles $\varphi_{c,1} = \frac{3\pi}{4}$ and $\varphi_{c,2} = \frac{7\pi}{4}$ for $\eta = 0.5$ and zero cubic SOI. For $\beta/\alpha = \pm 1$ and zero cubic SOI, the instantaneous eigenenergies collapse to the dotted lines, which cross at the critical angles. These lines are defined by the matrix element $\langle\pm|\,\boldsymbol{\mu}\cdot\boldsymbol{\sigma}\,|\pm\rangle$, calculated with respect to the PSH eigenstates. This corresponds to a 100% diabatic transition probability since the instantaneous bands touch and the local structure of the eigenstates fulfills Berry's parallel transport requirement [138]. For $\beta/\alpha = \pm 1$ and finite cubic SOI, a gap is re-introduced between the energy levels. The position of the minima with respect to φ remains unchanged.

The momentum direction is changed by disorder scattering such that the spin evolution is subject to inhomogeneities of the effective spin-orbit field $\boldsymbol{\mu}$.

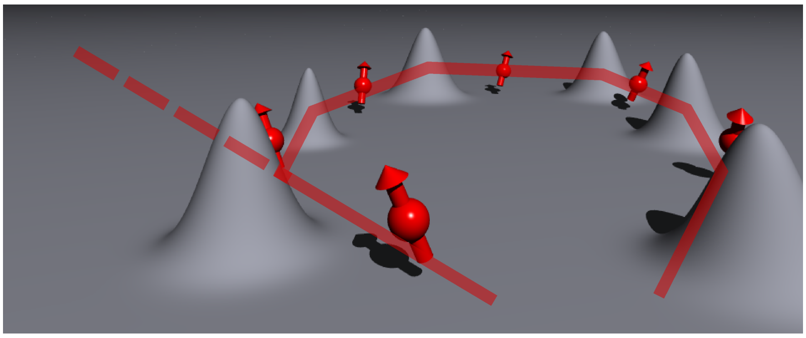

Figure 5.16: (illustration of small angle scattering) Weak scattering in a smooth disorder potential changes the momentum direction of a particle only by small values.

In the following we assume weak elastic scattering, such that we may model the change in the polar angle of the momentum $\delta\varphi$ in a time interval δt by the equation

$$\delta\varphi = \frac{\pi}{2\tau\zeta}\delta t, \tag{5.71}$$

where we introduce the phenomenological parameter ζ by hand. $\zeta = 1$ corresponds to a momentum change due to isotropic scattering and τ is the elastic momentum relaxation time.

Above equation introduces time dependence in the description of the momentum $\boldsymbol{k}(t) \approx k(\cos\varphi(t)\hat{\boldsymbol{x}} + \sin\varphi(t)\hat{\boldsymbol{y}})$ and provides the motivation to consider the evolution of a spinor initially polarized in the PSH eigenstates $|\pm\rangle$, defined in Eq. (5.49).

In 2DEGs as in 2DHGs the PSH eigenstates $|\pm\rangle$ match the eigenstates of the SOI Hamiltonian $|\pm\boldsymbol{\mu}\rangle$ from Eq. (5.63), for zero SOI. In our numerical setups we support a smooth transition between these states at the lead-cavity intersection by defining a region close to the leads, in which the SOI parameters are slowly increased from zero to their final values.

Consequently the spinors $|\pm\boldsymbol{\mu}\rangle$ of the scattered wavefunction pass by an avoided crossing when the angle has changed to values that coincide with the minima in the anisotropic spin splitting.

In short, we assume that the orbital dynamics is adiabatic, while the spinor may evolve non-adiabatically. We show a schematic of the corresponding configuration space picture in Fig. 5.16, which illustrates scattering processes with incremental momentum changes.

At the minima of the anisotropic spin splitting $2\,|E_\sigma(\boldsymbol{\mu})|$, transitions of the type $|\pm\boldsymbol{\mu}\rangle \rightarrow |\mp\boldsymbol{\mu}\rangle$ occur with the Landau-Zener transition probability P_D [48, 49], given by the expression

$$P_{\mathrm{D}} = \exp\left[-\frac{2\pi\epsilon_{12}^2}{\left(\hbar\left|\partial_t\left(\epsilon_1(t)-\epsilon_2(t)\right)\right|\right)}\right]. \tag{5.72}$$

The value of P_{D} is calculated from the minimal spin splitting, $2\epsilon_{12}$ at the critical angles ϕ_c and the slope of the splitting, $\epsilon_1(t)-\epsilon_2(t)$, between the fully diabatically coupled basis states $|+\rangle$ and $|-\rangle$.
For p-type systems we find a probability of

$$\ln(P_{\mathrm{D}})_{\mathrm{2DHG}} = -Q_{\mathrm{2DHG}}\left|\bar{\gamma}+\delta\right|\left(1-|\eta|\right)^2, \tag{5.73}$$

with the effective adiabaticity parameter of the hole gas,

$$Q_{\mathrm{2DHG}} := \zeta L_{\mathrm{F}}|k_{\mathrm{D}}|. \tag{5.74}$$

that depends on the elastic mean free path L_{F}. Equation (5.73) is derived under the assumption that $\bar{\gamma} \neq -\delta$. Eq. (5.73) does therefore not cover the description of T_{D} for parameters where the PSH symmetry is established. It is nevertheless applicable to realistic material parameters if $\gamma_3 \neq 0$ and, consequently, $\bar{\gamma} \neq \delta$, which is verified by a numerical transport analysis shown in Fig.5.14.
For fixed nonzero α, in 2DEGs we obtain

$$\ln(P_{\mathrm{D}})_{\mathrm{2DEG}} = -Q_{\mathrm{2DEG}}\frac{\left[\left|\bar{\eta}-\frac{\Gamma_\alpha}{2}\right| - \mathrm{sgn}\left(\bar{\eta}-\frac{\Gamma_\alpha}{2}\right)\right]^2}{\left|\mathrm{sgn}\left(\bar{\eta}-\frac{\Gamma_\alpha}{2}\right)+\frac{\Gamma_\alpha}{2}\right|}, \tag{5.75}$$

with the effective adiabaticity parameter,

$$Q_{\mathrm{2DEG}} := \zeta L_{\mathrm{F}}|L_{\mathrm{so}}^{\alpha}|^{-1}. \tag{5.76}$$

Thus the width of the Landau-Zener signature in the transmission is influenced by the Rashba spin precession length L_{so}^{α} and the ratio of cubic and linear SOI $\Gamma_\beta = k_{\mathrm{F}}^2\gamma/\beta$, consistent with Fig. 5.13. For 2DEGs we compare the numerical results for $\langle T_{\mathrm{D}}\rangle$ / $\langle T\rangle$ with the function

$$\frac{1}{2}+\frac{b}{2}P_{\mathrm{D}}(\eta), \tag{5.77}$$

with an additional phenomenological parameter b, that is 1 in the absence of cubic SOI and decreases for larger cubic SOI, because the PSH states no longer match exactly the instantaneous eigenstates. Although that we fit the data against the two parameters ζ and b, it is still remarkable that the position of the maxima of our simple analytical model, plotted in Fig. 5.13 b), coincides to a great detail with the numerically obtained positions shown in Fig. 5.13 a). To illustrate this point, we include arrows in Fig. 5.13 a) that point to the analytical maxima of the Landau-Zener curves. The Landau-Zener transitions enhance the value of T_{D} while completely suppressing T_{OD} for $P_{\mathrm{D}} = 1$.

Note that in Eq. (5.73) the parameter η defines the ratio of externally controllable Rashba SOI and the intrinsic, material dependent Dresselhaus SOI, in Eq. (5.75), the parameter $\bar{\eta}$ defines the inverse of the ratio of the respective contributions to the SOI.

Based on a qualitative reasoning similar to the argument presented here, we demonstrate in appendix D, given an arbitrary inplane spin-orbit field in two dimensions, a simple interpretation of the magnetoconductance correction in the context of topological properties of the band structure. The naive approach is consistent with the numerical findings for 2DEGs as well as 2DHGs and predicts correctly the observation of WAL in the presence of arbitrary SOI and WL in the PSH regime. However our approach fails to reproduce the WL observed in 2DEGs for the approximate symmetry at shifted ratios of $\tilde{\beta}/\alpha$. However, this is due to the fact that the our simple picture assumes fully adiabatic transport, while the case made in the present chapter assumed exactly the opposite to show the signatures in the Drude conductance. Interestingly, in the 2DEG the diabatic transitions take place in the same parameter regime as the PSH symmetry is established. Therefore, although the topological arguments assigns a WAL-typical Berry phase of π to the backscattered paths, their contribution gets small compared to the paths that are subject to diabatic transmissions and therefore loose the corresponding Berry phase.

In summary, in the present chapter we have shown an alternative way to detect parameter regimes of enhanced spin lifetimes in electron and hole gases, by measuring spin resolved conductances under variation of the the Rashba SOI. We have demonstrated that peaks in the spin diagonal transmission can be observed in 2DEGs for values of the SOI parameters, that are close to the regime of the WAL-WL-WAL transition point in the conductance correction, which correspond to enhanced spin lifetimes. In particular in hole gases, where the cubic structure of the SOI principally enhances spin relaxation rates that enter the formalism of the mesoscopic conductance corrections [78], the method presented here can be of particular use, since the corresponding signal can be measured in the conductance itself and is visible in regimes, where no WL signal does occur.

Chapter 6

Conclusions and Perspectives

We have presented various concepts which allow control over spin transport in semiconductor based devices.

6.1 Adiabaticity mediated spin transport

In Chap. 4 we introduced a novel concept that allows for reliable manipulation and switching of spin currents by exploiting properties of magnetic semiconductors in the presence of modulated magnetic field textures.
A semiclassical approach to the Landauer-Büttiker framework describes the experimentally found signatures of diabatic Landau-Zener transitions of the electronic spin evolution. The giant Zeeman interaction in the considered material allows experimental control over the spin degree of freedom.
This motivated our proposal for a diabatically switched spin-transistor. The functionality of our concept is supported by the experiment [1]. Although the operation of the device is robust against disorder [2], the Curie temperature T_C of the magnetic semiconductor still represents a significant limitation.
Realization of our concept in a hole-gas system, such as p-type (In,Mn)As or (Ga,Mn)As, is promising because of the p-d exchange interaction, that is reflected in increased effective g-factors and the persistence of the giant-Zeeman interaction to larger temperatures [62]. In zinc blende type materials theory suggests that room temperature values for T_C are within reach [146]. Particularly (Ga,Mn)As is an interesting compound in this respect, indicated by a measured value of $T_C = 110K$ in the 90's [170], and $T_C = 173K$ recently [171]. In this context we are confident that our findings represent an advance with respect to the ultimate goal of realizing stable room-temperature spintronics.

We like to emphasize that our concept can be generalized beyond the proposed realization in modulated dilute magnetic semiconductors. In fact Landau-Zener transitions have previously been detected in a variety of physical systems, including ultracold atoms [172], cold molecules [173] and solid-state qubits [174, 175], which typically represent time dependent problems.

The idea of tuning Landau-Zener transitions to perform logical operations in a quantum mechanical device is perceived outside the field of spintronics, including a recent example of experiments on Bose-Einstein condensates (BEC) with gauge-field induced effective spin-orbit coupling, in which tunable Landau-Zener are used to induce switching and basic “atomtronic” device operation [176]. While in our example of Ref. [1] the driving force of the diabatic transitions is the longitudinal voltage drop that induces a current, in Ref. [176] the driving forces are realized by the gravitational pull and the driving potential, which accelerate the BEC.

Alternative mechanisms of tuning adiabaticity could be discovered by construction of explicitly time dependent invariants, according to the theory of Lewis and Riesenfeld [177], since the semiclassical picture allows a mapping from related time dependent dynamical problems [178, 179], to a problem with spatial inhomogeneities.

6.2 Controlling spin relaxation in 2DEGs and 2DHGs

In Chap. 5 we analyzed the effect of k-cubic spin-orbit interaction on spin relaxation, on transport experiments in 2DEGs. We focused in particular on the persistent spin helix regime [38], in which Bychkov-Rashba and Dresselhaus spin-orbit interaction are of equal strength and fix the spin precession axis. This regime is particularly interesting in the context of non-ballistic spin transistor operation, since even in disordered systems the spin is protected against the Dyakonov-Perel and the Elliot-Yafet spin relaxation [25].

Our main result is the observation of the weak localization in the presence of k-cubic spin-orbit interaction at shifted parameters of Rashba and Dresselhaus SOI, with respect to the parameters at which the exact spin preserving symmetry, associated with the persistent spin helix, arises. We explain the deviation of the respective shift observed in magnetotransport relative to the shift identified in optical experiments. An analysis of weak localization effects indicates, that spin randomization is also suppressed if the persistent spin helix conditions can only be fulfilled approximately, due to the presence of k-cubic spin-orbit interaction.

We presented a simple symmetry based argument for 2DEGs that supports this finding.

Furthermore, we repeated the analysis on spin relaxation for 2DEGs in the context of an effective model for hole gases in narrow quantum wells, which we developed in Chap. 2. We extended existing models by taking into account the Bychkov-Rashba and Dresselhaus spin-orbit interaction, which scale cubically in the momentum and considering terms beyond the axial approximation.

We were able to identify an exact symmetry corresponding to enhanced spin lifetimes in two dimensional hole gases (2DHGs). For the realization of this symmetry, we showed that non-axially symmetric terms in the Hamiltonian are crucial. We found that the analogue to the electronic persistent spin helix symmetry in hole gases is established if Bychkov-Rashba and Dresselhaus terms are of equal magnitude and in addition, the Luttinger parameters of the crystal lattice fulfill an additional requirement. This additional restriction make it difficult to identify extended spin life times in weak localization measurements in 2DHGs.

We suggested detection of the parameter regime attributed to enhanced spin lifetimes in the spin diagonal part of the Drude conductance, which leads to visible signals even if the exact symmetry requirement is not fulfilled.

Our considerations represent the static limit, although excitations enter in the description of the Cooperon spectrum, on which a spin dynamic transport equation can be mapped [117]. However optical experiments, as the measurements performed by Koralek et. al [39], propose further insight. Mentioned measurements are based on Bernevig et. al's theoretical identification of a persistent spin state of finite wavevector excitations [38] which can be measured in terms of absorption maxima in spectroscopy. Even if exact symmetry associated with a PSH spin state seem difficult to access in realistic materials, approximate symmetries should be recognizable in such absorption spectra.

The findings on the effect of k-cubic contributions in 2DEGs could also be of relevance to an ongoing collaborative project with Nitta's group, which represents the first proof of concept for an all electrical detection method of the ratio of Rashba and Dresselhaus spin-orbit interaction in narrow wires. The underlying theory is presented in Ref. [165]. The anisotropy of dimensionally induced weak localization in wires subject to an inplane magnetic field is used to determine the respective material properties. Experimental findings agree remarkably well to numerical findings to which we contributed. The mentioned work will be submitted for publication.

Appendix

Appendix A

Derivation of the Semiclassical Spin Propagator

In the following we adapt the calculation outlined in Ref. [108] for the momentum dependent spin-orbit interaction in a 2DEG. Our goal is to derive the semiclassical approximation to the spin dependent propagator. To achieve this, we remind ourselves that the exact propagator

$$K^{\sigma,\sigma'}(\boldsymbol{r},\boldsymbol{r}',t) := \langle\sigma|\,\langle\boldsymbol{r}|\exp\left[-\frac{i}{\hbar}\mathrm{H}t\right]|\mathbf{r}'\rangle\,|\sigma'\rangle \tag{A.1}$$

of any time independent Hamiltonian H of the form

$$\mathrm{H} = \left[\frac{p^2}{2m} + V(\boldsymbol{r})\right]\mathbb{1} + [\boldsymbol{\mu}_r(\boldsymbol{r}) + \boldsymbol{\mu}_p(\boldsymbol{p})]\cdot\boldsymbol{\sigma}, \tag{A.2}$$

can be obtained from Feynman's path integral [151]. The latter can be constructed via the Trotterization technique,

$$\begin{aligned}
&K^{\sigma,\sigma'}(\boldsymbol{r},\boldsymbol{r}',t) = \lim_{N\to\infty}\langle\sigma|\,\langle\boldsymbol{r}|\exp\left\{-\frac{\lambda}{N}\mathrm{H}\right\}^N|\boldsymbol{r}'\rangle\,|\sigma'\rangle \\
&= \lim_{N\to\infty}\langle\sigma|\,\langle\boldsymbol{r}|\left\{\exp\left[-\frac{\lambda}{N}\left(\frac{p^2}{2m}\mathbb{1} + \boldsymbol{\mu}_p(\boldsymbol{p})\cdot\boldsymbol{\sigma}\right)\right]\exp\left[-\frac{\lambda}{N}\left(V(\boldsymbol{r})\mathbb{1} + \boldsymbol{\mu}_r(\boldsymbol{r})\cdot\boldsymbol{\sigma}\right)\right]\right. \\
&\left.\times\ \exp\left[\mathrm{O}\left(\frac{\lambda^2}{N^2}\right)\right]\right\}^N|\boldsymbol{r}'\rangle\,|\sigma'\rangle\,,
\end{aligned} \tag{A.3}$$

which is based on the introducing of the complex time parameter $\lambda = it/\hbar$ and the application of Glauber's formula,

$$\exp[\lambda(A+B)] = \exp[\lambda A]\exp[\lambda B]\exp[-\frac{\lambda^2}{2}[A,B]], \tag{A.4}$$

assuming that higher order commutators vanish. The path integral is obtained from inserting the identity written in terms of the complete position and momentum basis states between the factorized exponentials. The result of this manipulation is, up to linear order in the small parameter λ/N, given by

$$\begin{aligned}
&\langle\sigma| \lim_{N\to\infty}\int\left[\prod_{i=1}^{N-1}\mathrm{d}\boldsymbol{r}_i\prod_{j=1}^{N}\mathrm{d}\boldsymbol{p}_j\right](2\pi\hbar)^{-dN}\prod_{l=1}^{N}\left\{\exp\left[-i\frac{(\boldsymbol{r}_l-\boldsymbol{r}_{l-1})\,\boldsymbol{p}_l}{\hbar}\right]\right.\\
&\left.\exp\left[-\frac{\lambda}{N}\left(\frac{p_l^2}{2m}+V(\boldsymbol{r}_l)\right)\right]\exp\left[-\frac{\lambda}{N}\left(\boldsymbol{\mu}_p(\boldsymbol{p}_l)\boldsymbol{\sigma}\right)\right]\exp\left[-\frac{\lambda}{N}\left(\boldsymbol{\mu}_r(\boldsymbol{r}_l)\boldsymbol{\sigma}\right)\right]\right\}|\sigma'\rangle=\\
&\lim_{N\to\infty}\int\left[\prod_{i}^{N-1}\mathrm{d}\boldsymbol{r}_i\prod_{j}^{N}\mathrm{d}\boldsymbol{p}_j\right](2\pi\hbar)^{-dN}\prod_{l=1}^{N}\left\{\exp\left[\sum_{l=1}^{N}-\frac{i}{\hbar}\left(\boldsymbol{r}_l-\boldsymbol{r}_{l-1}\right)\boldsymbol{p}_l-\right.\right.\\
&\left.\left.\frac{\lambda}{N}\left(\frac{p_l^2}{2m}+V(\boldsymbol{r}_l)\right)\right]\right\}\times\langle\sigma|\,\mathrm{Texp}\left\{-\frac{\lambda}{N}\sum_{l=1}^{N}\left[\boldsymbol{\mu}_p(\boldsymbol{p}_l)+\boldsymbol{\mu}_r(\boldsymbol{r}_l)\right]\cdot\boldsymbol{\sigma}\right\}|\sigma'\rangle\,, \quad \text{(A.5)}
\end{aligned}$$

for spatial dimension d. Final and initial coordinates $\boldsymbol{r}'$ and $\boldsymbol{r}$ are included in above notation, where $\boldsymbol{r}_N := \boldsymbol{r}'$ and $\boldsymbol{r}_0 := \boldsymbol{r}$. The spin information is contained within the term in the last line of Eq. (A.5), which is commonly defined as the discretized version of the spin evolution kernel [114],

$$\mathrm{D} = \mathrm{Texp}\left[-\frac{\lambda}{N}\sum_{l=1}^{N}\left[\boldsymbol{\mu}_p(\boldsymbol{p}_l)+\boldsymbol{\mu}_r(\boldsymbol{r}_l)\right]\cdot\boldsymbol{\sigma}\right], \quad \text{(A.6)}$$

or spin propagator, which, in the limit $N\to\infty$ can alternatively be defined by the equation [108],

$$\mathrm{i}\hbar\frac{\partial}{\partial t}\mathrm{D} = \left[\boldsymbol{\mu}_p(\boldsymbol{p})+\boldsymbol{\mu}_r(\boldsymbol{r})\right]\mathrm{D}, \quad \text{(A.7)}$$

provided that the phase space coordinates are determined by a particular classical trajectory of the classical analogue of the spin independent remaining terms in the Hamiltonian.

This can be deduced as first order perturbative result within a semiclassical expansion of the exact propagator, giving the correct result if the trajectory in phase space fulfills the Hamilton Jacobi equation [114]. Alternatively we can continue from the preceding calculation in the way, illustrated for a two-dimensional spin-orbit Hamiltonian including Rashba SOI,

$$\mathrm{H}_{\mathrm{R},1} = \alpha\left(k_y\sigma_x - k_x\sigma_y\right), \quad \text{(A.8)}$$

and linear Dresselhaus SOI

$$\mathrm{H}_{\mathrm{D},1} = \beta\left(k_x\sigma_x - k_y\sigma_y\right), \quad \text{(A.9)}$$

which correspond here to the k-linear effective magnetic moment $\boldsymbol{\mu}_p(\boldsymbol{p}) = \boldsymbol{\mu}^1_{\mathrm{2DEG}}$ with

$$\boldsymbol{\mu}^1_{\mathrm{2DEG}}(\hbar\boldsymbol{k}) = \alpha\boldsymbol{k}\times\hat{\boldsymbol{z}} + \beta\left(k_x\hat{\boldsymbol{x}} - k_y\hat{\boldsymbol{y}}\right). \quad \text{((2.27))}$$

To obtain a semiclassical approximation of expression (A.5) we carry out the integrals over phase space coordinates. We start with the momentum integrals which can be evaluated exactly by inserting Eq. (2.27) in Eq. (A.5) and separate the integrations over the p_x and p_y momentum coordinate respectively. Although Rashba and Dresselhaus SOI can be treated simultaneously, we present the calculation for the Rashba term only, for the sake of readability. The p_x components in the exponent enter integrals of the type,

$$\begin{aligned}
&\int \mathrm{d}p_{x,l} \exp\left[-\frac{\lambda}{N}\frac{p_{x,l}^2}{2m} - \left(\frac{i}{\hbar}\Delta_{x,l} - \frac{\lambda}{N}\alpha\sigma_y\right)p_{x,l}\right] = \\
&\sqrt{\frac{2mN}{\lambda}}\int \mathrm{d}p \exp\left\{-\left[p^2 + p\sqrt{\frac{2mN}{\lambda}}\left(\frac{i}{\hbar}\Delta_{x,l} - \frac{\lambda}{N}\alpha\sigma_y\right)\right]\right\} = \\
&\sqrt{\frac{2\pi mN}{\lambda}}\exp\left\{-\frac{mN}{2\lambda}\left[\left(\frac{-\Delta_{x,l}^2}{\hbar^2} + \frac{\lambda^2}{N^2}\alpha^2 - \frac{2i\Delta_{x,l}\lambda\alpha}{\hbar N}\sigma_y\right)\right]\right\}, \qquad \text{(A.10)}
\end{aligned}$$

and while the p_y terms are given by,

$$\begin{aligned}
&\int \mathrm{d}p_{y,l} \exp\left[-\frac{\lambda}{N}\frac{p_{y,l}^2}{2m} - \left(\frac{i}{\hbar}\Delta_{y,l} + \frac{\lambda}{N}\alpha\sigma_x\right)p_{y,l}\right] = \\
&\sqrt{\frac{2\pi mN}{\lambda}}\exp\left\{-\frac{mN}{2\lambda}\left[\left(\frac{-\Delta_{y,l}^2}{\hbar^2} + \frac{\lambda^2}{N^2}\alpha^2 + \frac{2i\Delta_{y,l}\lambda\alpha}{\hbar N}\sigma_y\right)\right]\right\}, \qquad \text{(A.11)}
\end{aligned}$$

which is, up to a trivial phase shift, combined to the contribution to the propagator at time l,

$$\int \mathrm{d}^2 p_l \, \mathrm{M}_l = \frac{2\pi m\hbar}{i\epsilon}\exp\left[\frac{m}{2\hbar i\epsilon}\left(\boldsymbol{r}_l - \boldsymbol{r}_{l-1}\right)^2 - \frac{im\alpha}{\hbar}\boldsymbol{\sigma}\cdot\left(\boldsymbol{r}_l - \boldsymbol{r}_{l-1}\right)\times\hat{\boldsymbol{z}}\right], \quad \text{(A.12)}$$

where we introduced the infinitesimal timestep $\epsilon := -i\lambda\hbar/N$, in order to illustrate that in the limit $\epsilon \to 0$ the first term in the exponential converges to the classical action along a straight line segment between the positions $\boldsymbol{r}_l$ and $\boldsymbol{r}_{l-1}$. Since we consider only SOI linear in the wavenumber, all occurring momentum integrals can be carried out exactly - principally also for spatially varying SOI parameters. After integration of the remaining position integrals within the stationary phase approximation (SPA), the result is no longer exact and therefore denoted as semiclassical approximation. The integrations are replaced by summation over the points of stationary phase, which coincide with the classically allowed trajectories that minimize the respective action of all possible paths [113]. For simplicity we assume constant SOI parameters and neglect influences of the spin structure on the stationary phase points. After Fourier transformation with respect to time, we obtain the semiclassical Green's function for a constant energy, which is given as in Ref. [122], in terms of a summation over classical trajectories r that connect the points $\boldsymbol{r}'$ and $\boldsymbol{r}$ at energy

E,

$$G(\boldsymbol{r},\boldsymbol{r}',E)^{\sigma\sigma'} = \sum_{r:\boldsymbol{r}'\to\boldsymbol{r}} A_r e^{i\frac{S_r}{\hbar}} \mathrm{D}_r = \sum_{r} A_r e^{i\frac{S_r}{\hbar}} \prod_{l\in r} \mathrm{K}_l, \tag{A.13}$$

where A_r denotes, up to constants, the purely classical stability amplitude of the respective trajectory, S_r the corresponding classical action, and $\prod_{l\in r}\mathrm{K}_l$ the factorized spin propagator for paths that consist of a sequence of straight line segments, that are determined by the boundary conditions and the disorder distribution of the considered system. The expression originates directly from Eq. (A.12), which leads to the definition

$$\mathrm{K}_l := \exp\left[i(L^{\alpha}_{\mathrm{so}})^{-1}\hat{\boldsymbol{z}} \times \boldsymbol{\Delta}_l \cdot \boldsymbol{\sigma}\right], \tag{A.14}$$

for the presence of only Rashba SOI. The definition of the well known spin precession length

$$L^{\alpha}_{\mathrm{so}} := \frac{\hbar}{m\alpha} \tag{A.15}$$

is found from combination of all constants in equation (A.12), which obviously represents the relevant length scale for the spin evolution corresponding to a particle that evolves in space along a line segment

$$\boldsymbol{\Delta}_l := (\boldsymbol{r}_l - \boldsymbol{r}_{l-1}). \tag{A.16}$$

Repeating above procedure for both, Rashba and linear Dresselhaus contribution, we arrive at the infinitesimal spin propagator

$$\mathrm{K}_l : \exp\left\{i\left[(L^{\alpha}_{\mathrm{so}})^{-1}\hat{\boldsymbol{z}} \times \boldsymbol{\Delta}_l + (L^{\beta}_{\mathrm{so}})^{-1}\left(\Delta_{l,x}\hat{\boldsymbol{x}} - \Delta_{l,y}\hat{\boldsymbol{y}}\right)\right] \cdot \boldsymbol{\sigma}\right\}, \tag{A.17}$$

with the Dresselhaus spin precession length scale

$$L^{\beta}_{\mathrm{so}} := \frac{\hbar}{m\beta}. \tag{A.18}$$

The semiclassical expression (A.17) can be used to demonstrate the impact of the persistent spin helix symmetry [25, 38] on spin evolution, which is determined by the objects K_l. If one of the conditions $L^{\beta}_{\mathrm{so}} = \pm L^{\alpha}_{\mathrm{so}} =: L_{\mathrm{so}}$ holds, the vector coupling to the spin does not change its direction. The spin precession gets independent on the individual path and is fully determined by the initial and final point of the given trajectory, as described in Ref. [25]. In the respective cases the spin precession angle is given by

$$L^{-1}_{\mathrm{so}}(\Delta_x \pm \Delta_y). \tag{A.19}$$

From the semiclassical perspective presented here, k-cubic contributions to the SOI complicate the calculation considerably, since a transformation, as presented above, with which the momentum integration can be recast into Gaussian integrals, is no longer possible in this case. For this reason we used the results of diagrammatic perturbation theory to approach localization phenomena in electronic and hole systems in the presence of k-cubic SOI in Chap. 5 - although the semiclassical picture has been used successfully in the description of systems with k-linear SOI in the past [95].

Appendix B

Transmission amplitude of a ballistic waveguide

The transmission of a ballistic waveguide structure represents an example for which the semiclassical approximation coincides with the exact quantum mechanical result.

To illustrate this point, we first show how one arrives at the spinless transmission amplitude t_{nm} using exact quantum mechanical formalisms. We will use the spectral formulation of the retarded Green's function, as derived in Ref. [52].

$$G_R(\boldsymbol{r}, \boldsymbol{r}', E_\mathrm{F}) = \sum_n \frac{\Psi_n(\boldsymbol{r})\Psi_n^\star(\boldsymbol{r}')}{E_\mathrm{F} - E_n + i0_+}, \tag{B.1}$$

is the mentioned expression, with the system's eigenbasis $\{\Psi_n\}$ and the corresponding spectrum E_n. In an infinitely long waveguide with hard walls in $\hat{y}$-direction, Eq. (B.1) is specified in terms of the lead's eigenbasis ϕ_n defined in Eq. (3.17) and evaluated at the lead edges at $x = 0$ and $x' = L$. We proceed by inserting the spectral representation of the Green's function into the Fisher-Lee relation for the transmission amplitude (3.14) and obtain

$$\begin{aligned} t_{nm} = -i\hbar\sqrt{v_n v_m} \int_0^W \int_0^W \mathrm{d}y\mathrm{d}y' \phi_n(y)\phi_m(y') \\ \sum_l \frac{\int \mathrm{d}k}{2\pi i} \frac{2m}{\hbar^2} \frac{\phi_l(y)\phi_l(y')}{k_\mathrm{F}^2 - (n\pi/W)^2 - k^2 + i0_+}. \end{aligned} \tag{B.2}$$

The expression above can be simplified by exploiting the orthogonality of the lead eigenfunctions. One notices immediately that the latter establishes a diagonal transmission matrix $t_{nm} \sim \delta_{nm}$ which implies conservation of transversal momentum amplitude. After performing the remaining integral over k with the residue theorem [112], we arrive at the final result (3.61),

$$t_{nm} = i\delta_{nm} \exp{(ik_\mathrm{F} L \cos\theta_n)}, \tag{B.3}$$

where we defined the transversal momentum component as

$$\cos\theta_n = \sqrt{1 - \left(\frac{n\pi}{k_\mathrm{F} W}\right)^2}. \tag{B.4}$$

We remind ourselves that the integer n is smaller or equal to the number of conducting channels N. Therefore the possible angles θ_n are restricted to the interval $[-\pi/2, \pi/2]$, in which $\cos\theta_n \geq 0$ holds. Thus we arrive at the phase a wavepacket acquires, that has the longitudinal momentum component $k_\mathrm{F}\cos\theta_n$ and traverses the distance L.

Although reaching the result (3.61) by semiclassical methods is slightly more involved, we find it valuable to present the explicit calculation here. It shows that the semiclassical approximation is able to reproduce exact results in the context of integrable structures. The applicability in the context of chaotic mesoscopic transport is by now widely established and checked against random matrix theory and even numerical calculations [180, 92, 94]. The ergodicity property of chaotic structures allows for the use of classical sum rules [181, 94]. With the help of these sum rules simple and closed analytical expressions can be found, that describe transport properties of these systems. The latter include the correct description of interference phenomena, such as weak localization [182, 94] or antilocalization [95]. The following discussion motivates a straightforward connection of quantum mechanical features and the more intuitive underlying classical dynamics of a problem, which in this case is based on an integrable waveguide structure. Integrable systems lack of chaotic self-averaging and are therefore more susceptible to additional non-universal quantum corrections, such as the occurence of diffractive paths, interference phenomena may arise due to edges [183, 184, 185] or delta like potential spikes [120].

Weak disorder, as encountered in Betthausen's experiments [1] that we present in Chap. 4, can be introduced in the picture of a waveguide in terms of delta like impurities. Vattay and coworkers have investigated this problem in Ref. [120]. They arrived at the conclusion that the presence of impurities gives rise to non-classical diffractive paths which modify the transmission power spectrum. If the number of such impurities is sufficiently small, the overall transmission amplitude is however still dominated by the ballistic paths described here, since the diffractive paths decay more rapidly [120]. In the following we will consider the non-classical paths as a small correction and illustrate the semiclassical method of an essentially ballistic waveguide.

In contrast to the full quantum mechanical ansatz, we insert the semiclassical Green's function (3.60) into the Fisher Lee relation, which leads to the expression

$$t_{nm} = -i\hbar\delta_{nm}\frac{v_n}{W}\int_0^W\int_0^W \mathrm{d}y\mathrm{d}y'\Big\{\Big(\cos\left[\frac{n\pi}{W}(y-y')\right] - \cos\left[\frac{n\pi}{W}(y+y'))\right]\Big]\Big)$$
$$\times\sum_r \frac{me^{-i\frac{3\pi}{4}}}{\hbar^2\sqrt{2\pi}}\frac{(-1)^{c_r}e^{ik_{\mathrm{F}}l_r}}{\sqrt{k_{\mathrm{F}}l_r}}\Big\}, \tag{B.5}$$

where l_r is the length of the classical path r, the integer c_r counts the number of collisions with the walls and the phase factor $e^{-i\frac{3\pi}{4}}$ is due to the caustic at the origin of each trajectory [120]. As can be seen in the extended zone scheme presented in Fig. 3.5, the path length is connected to the incident angle θ via the relation

$$l_r\cos\theta = L. \tag{B.6}$$

We anticipated conservation of angular momentum. It can be inferred from a glance at the waveguide geometry. Paths not obeying this symmetry correspond to rapidly oscillating phases of the terms that enter the summation, and therefore average to zero in the semiclassical formalism. This observation is also the main motivation for what is called the diagonal approximation in the channel number in similar contexts [93]. It is helpful to express the transversal lead coordinates as

$$Q = y + y' \quad \text{and} \quad q = y' - y, \tag{B.7}$$

respectively. This transformation allows us to uniquely define the classically deterministic connection between initial and final coordinates at fixed θ,

$$\begin{aligned} L\tan\theta &= q + n_rW && \text{for} \quad n_r = 2k \quad \text{and} \\ L\tan\theta &= -Q + (n_r+1)W && \text{for} \quad n_r = 2k+1, \end{aligned} \tag{B.8}$$

where $k = 0, 1, 2, ...$ We express the summation over trajectories as summation over the number of reflections n_r and the Liouville measure, that fulfills the conditions (B.8),

$$\sum_r \rightarrow \sum_{n_r=0}^{\infty}\int_{\theta_r}^{\theta_{r+1}} \mathrm{d}\theta\delta(\theta - \theta(q, Q, n_r)). \tag{B.9}$$

We then split the summation into even or odd times reflected trajectories, from hereon denoted even or odd paths. For even (odd) paths one position integral in (B.5) is eliminated by the delta function, while the remaining integral yields the integration range $2W$. This can be seen from (B.8), since even (odd) paths only depend explicitly on $q(Q)$. We remind ourselves that the connection between the q coordinate and the θ is related by the Jacobian,

$$\delta\left(\theta - \theta(q)\right) = \left|\frac{\partial\theta}{\partial q}\right|^{-1}\delta\left(q_\theta - q\right), \tag{B.10}$$

where

$$\left|\frac{\partial\theta}{\partial q}\right|^{-1} = \frac{L}{\cos^2\theta}. \tag{B.11}$$

The Jacobian of the transformation of Q into θ for the odd trajectory type is identical. In our ansatz (B.5), the cosine terms from the lead eigenstates are multiplied to the even (odd) contributions of the Green's function. The only combinations of these terms, that are not zero after integration, are those, in which the cosine term and the respective parity are multiplied, which depend on the same coordinate. Integration over an unmodified cosine term trivially vanishes. This leaves us with

$$\begin{aligned} t_{nm} = -\delta_{nm} e^{-i\frac{\pi}{4}} \sqrt{\frac{k_{\mathrm{F}}L}{2\pi}} \sum_{k=0}^{\infty} \Bigg\{ \int_{\theta_{2k}}^{\theta_{2k+1}} \mathrm{d}\theta (\cos\theta)^{-\frac{3}{2}} \cos\left[\frac{n\pi}{W}\left(L\tan\theta - 2kW\right)\right] e^{i\frac{k_{\mathrm{F}}L}{\cos\theta}} \\ + \int_{\theta_{2k+1}}^{\theta_{2k+2}} \mathrm{d}\theta (\cos\theta)^{-\frac{3}{2}} \cos\left[\frac{n\pi}{W}\left(-L\tan\theta + (2k+2)W\right)\right] e^{i\frac{k_{\mathrm{F}}L}{\cos\theta}} \Bigg\}. \end{aligned} \tag{B.12}$$

Due to the symmetry of the cosine both integrations can be combined and written as

$$-\delta_{nm}\frac{e^{-i\frac{\pi}{4}}}{2}\sqrt{\frac{k_{\mathrm{F}}L}{2\pi}}\cos\theta_n \sum_{\sigma=\pm1}\int \mathrm{d}\theta(\cos\theta)^{-\frac{3}{2}} \exp\left[ik_{\mathrm{F}}L\left(\sigma\frac{n\pi}{k_{\mathrm{F}}W}\tan\theta + \frac{1}{\cos\theta}\right)\right], \tag{B.13}$$

to which we apply the stationary phase approximation (SPA) in order to solve the integral. The stationary phase points are, as usually [93, 94], in agreement with the classically expected incident angles

$$\frac{-n\pi}{k_{\mathrm{F}}W}\sigma = \sin\theta. \tag{B.14}$$

Up to a sign, the thus determined angles θ coincide exactly with the angles θ_n of the flux normalization prefactors. This shows nicely how size quantization of a waveguide effects the classically considered paths in terms of quantization of incident angles. For completeness, the SPA of a slowly varying function $g(x)$ and rapidly oscillating continuous $f(x)/\hbar$, is defined as [186]

$$\int g(x)e^{\frac{i}{\hbar}f(x)} \simeq \sum_{\{x_i:f'(x_i)=0\}} \sqrt{\frac{2\pi\hbar}{|f''(x_i)|}}g(x_i)\exp\left[\frac{i}{\hbar}f(x_i) + \frac{i\pi}{4}\operatorname{sgn}\left(f''(x_i)\right)\right]. \tag{B.15}$$

The stationary phase points x_i, here represented in terms of the coordinate θ, should be isolated and sufficiently far away from the integration boundaries. Under these conditions and in the semiclassical limit $\hbar \to 0$, the relationship is exact. After applying Eq. (B.15) straightforwardly to our problem, we simplify the remaining trigonometric expressions to reproduce exactly the quantum mechanical result (3.61). Although seemingly trivial, we are unaware of a semiclassical derivation of this closed expression,

Appendix C

Adiabatic Theorem of Quantum Mechanics

Prior to the discussions on effects requiring adiabaticity or describing its breakdown we want to include a brief overview on the Adiabatic Theorem of Quantum Mechanics introduced in 1928 by Born and Fock [129]. Say we consider a change of parameters within the Hamiltonian of a quantum mechanical system $H = H(\tau)$, where the rate of change τ can be defined as the product of a small parameter ϵ and the time parameter $t \in [0, 1/\epsilon]$. Suppose we have access to a unitary matrix $S(t)$ with the property

$$SHS^{-1} = H_D = \mathrm{diag}\left(\mathrm{E_1}, .., \mathrm{E_N}\right), \tag{C.1}$$

such that the time dependent Schrödinger equation of the problem

$$H\left|\Psi\right\rangle = i\hbar\frac{\mathrm{d}}{\mathrm{d}t}\left|\Psi\right\rangle \tag{C.2}$$

can be formulated in terms of rotated vectors in Hilbert space $\left|\Psi'\right\rangle := S\left|\Psi\right\rangle$ in the form

$$H_D\left|\Psi'\right\rangle = i\hbar S\left(\frac{\mathrm{d}}{\mathrm{d}t}S^{-1}\right)\left|\Psi'\right\rangle + i\hbar\frac{\mathrm{d}}{\mathrm{d}t}\left|\Psi'\right\rangle, \tag{C.3}$$

which for an initial state $\left|\Psi'(0)\right\rangle$ has the solution

$$\left|\Psi'(t)\right\rangle = \mathrm{Texp}\left\{-\frac{\mathrm{i}}{\hbar}\left[\int_0^{\mathrm{t}}\mathrm{H_D} - \mathrm{i}\hbar\epsilon\mathrm{S}\left(\frac{\mathrm{d}}{\mathrm{d}\tau}\mathrm{S}^{-1}\right)\right]\right\}\left|\Psi'(0)\right\rangle. \tag{C.4}$$

From equation Eq. (C.4), if we choose the initial state as an Eigenstate of H_{D} we observe, that for infinitesimally slow parameter changes at $\epsilon \to 0$, that the second term in the exponential can be dropped. Consequently under variation of t the system remains in its Eigenstate multiplied by a phase factor.

Appendix D

The Geometric Phase

D.1 Introduction to the Berry phase

In the following we present Berry's argument leading to the geometric phase [138]. This phase is a property of the wavefunction $|\Psi(t)\rangle$ of a quantum mechanical system described by the Hamiltonian $H\left[\boldsymbol{R}(t)\right]$ subject to a vector $\boldsymbol{R}(t)$ in parameter space that undergoes an adiabatic change on the timescale t.
Berry found his result starting from the time dependent Schrödinger equation

$$H\left[\boldsymbol{R}(t)\right]|\Psi(t)\rangle = i\hbar\frac{\mathrm{d}}{\mathrm{d}t}|\Psi(t)\rangle\,, \tag{D.1}$$

under the assumption that for Eq. (D.1) there exists a set of instantaneous orthonormal eigensolutions $|n[\boldsymbol{R}])\rangle$, fulfilling

$$H\left[\boldsymbol{R}\right]|n[\boldsymbol{R}]\rangle = E_n\left[\boldsymbol{R}\right]|n[\boldsymbol{R}]\rangle\,. \tag{D.2}$$

With the ansatz

$$|\Psi(t)\rangle = \exp\left[-\frac{i}{\hbar}\int_0^t \mathrm{d}t' E_n\left[\boldsymbol{R}(t')\right]\right]\exp\left[i\gamma_n(t)\right]|n[\boldsymbol{R}(t)]\rangle\,, \tag{D.3}$$

which relies on adiabatic evolution of the system. Upon inserting Eq. (D.3) into Eq. (D.1) one obtains

$$E_n\left[\boldsymbol{R}(t)\right] = E_n\left[\boldsymbol{R}(t)\right] - \hbar\frac{\mathrm{d}}{\mathrm{d}t}\gamma_n(t) + i\hbar\left\langle n[\boldsymbol{R}(t)]\right|\nabla_{\boldsymbol{R}}\left|n[\boldsymbol{R}(t)]\right\rangle\frac{\mathrm{d}}{\mathrm{d}t}\boldsymbol{R}, \tag{D.4}$$

from which follows the condition

$$\frac{\mathrm{d}}{\mathrm{d}t}\gamma_n(t) = i\left\langle n[\boldsymbol{R}(t)]\right|\nabla_{\boldsymbol{R}}\left|n[\boldsymbol{R}(t)]\right\rangle\frac{\mathrm{d}}{\mathrm{d}t}\boldsymbol{R}, \tag{D.5}$$

which is for a closed loop C in the parameter space

$$\gamma_n(t) = i\oint_C \mathrm{d}\boldsymbol{R}\left\langle n[\boldsymbol{R}]\right|\nabla_{\boldsymbol{R}}\left|n[\boldsymbol{R}]\right\rangle\,. \tag{D.6}$$

Berry pointed out that evaluation of expression (D.6) may depend on the particular choice of the basis and pressed further to a more convenient formulation by applying Stokes theorem to a Hamiltonian of the structure

$$\mathrm{H} = \boldsymbol{\mu} \cdot \boldsymbol{\sigma} \text{ [138]..} \tag{D.7}$$

which gives rise to the basis independent formulation of Berry's geometric phase

$$\gamma_\sigma(C) = -\sigma \int\int_C \frac{\mathrm{d}\boldsymbol{s}\boldsymbol{\mu}}{2\mu^3}. \tag{D.8}$$

Latter equation is, up to constants, equivalent to the flux of a magnetic monopole with strength 1/2, penetrating the surface defined by the curve C or, from another perspective, the solid angle enclosed by C in the parameter space defined by the effective magnetic field $\boldsymbol{\mu}$ [138].

In our following considerations we take $\boldsymbol{\mu}$ oriented in the xy-plane, since this is the case for our SOI Hamiltonians for 2DEGs and the 2DHG model (2.40). Therefore, the expression (D.8) reduces to

$$\begin{aligned}
\gamma_\sigma(C) &= -\frac{1}{2}\sigma \int_0^{2\pi} \mathrm{d}\varphi \frac{1}{\mu^2(C)} \left[\left(\frac{\partial}{\partial\varphi}\mu_y(C)\right)\mu_x(C) - \left(\frac{\partial}{\partial\varphi}\mu_x(C)\right)\mu_y(C)\right] \\
&= -\frac{1}{2}\int_0^{2\pi} \mathrm{d}\varphi \frac{1}{\mu^2}\left(\boldsymbol{\mu} \times \frac{\partial}{\partial\varphi}\boldsymbol{\mu}\right)_z = -\frac{1}{2}\int_0^{2\pi} \mathrm{d}\varphi \frac{\partial}{\partial\varphi}\Theta_C(\varphi) \\
&= -1/2\left(\Theta_C(2\pi) - \Theta_C(0) + 2\pi n_C\right) = -\pi n_C
\end{aligned} \tag{D.9}$$

with the winding number n_C, which is a topological invariant of the curve C.

D.2 Connection to the mesoscopic conductance correction

The Berry phase or its non-adiabatic generalization, the Aharonov-Anandan phase [187] manifests itself in classical mechanics as the Hannay angle [188, 189] and in quantum mechanical ring geometries [190].

Analogous to these cases, the wavefunction of an electron or hole spin precessing around a non-constant vector $\boldsymbol{\mu}(t)$, acquires a geometric phase [138]. In the adiabatic limit a state initialized as instantaneous eigenstate with respect to the $\boldsymbol{\mu}(t)$-quantization axis, remains in the same eigenstate [129]. For a cyclic sweep in parameter space, that is when $\boldsymbol{\mu}$ returns exactly to its initial configuration, in addition to a dynamical phase, Berry found that the wavefunction acquires a nontrivial phase that depends on the geometry of the trajectory [138]. Therefore this additional Berry phase term, introduced as geometrical phase [138], is also denoted topological phase [191, 192, 193].

In condensed matter physics, the topological phase is also of major importance in the theoretical description of the Hall conductance σ_{xy} in various systems, including topological insulators, which possess promising physical properties [193]. One of these properties is the presence of edge channels with well defined chirality, that are protected due to quantization properties of topological invariants of the band structure [193]. The theory that establishes this connection is based on the Berry phase.

Effects of the Berry phase in the longitudinal conductance σ_{xx}, are found in ring geometries, that are subject to external magnetic fields and/or SOI [190, 144].Berry phase related effects in these systems are typically well described by two paths that traverse different sections of the ring geometry and interfere at the ends. The most prominent examples of these effects include the Aharonov-Bohm effect, which describes periodic oscillations of the conductance in the presence of an enclosed flux line [153]. Another example are the Aharonov-Casher oscillations of the conductance, that are periodic in an externally applied gate voltage which tunes the Rashba SOI [191].

In the following we focus on a band structure topology based interpretation of weak-localization and antilocalization phenomena.

In analogy to the conductance of cylinders [192], we will qualitatively describe its effect on the sign of the conductance correction by

$$\delta G \sim \exp\left[-i\gamma_\sigma\right]. \tag{D.10}$$

This picture is motivated by the semiclassical picture [108], in which the conductance correction is given by the interference of two time-reversal symmetry related paths, which are combined to a loop in momentum space.

In this picture the amplitude of the Cooperon contribution is proportional to the overlap of the state $|\chi_\sigma\rangle_+$ and its time reversal symmetry related partner $|\chi_\sigma\rangle_-$. $|\chi_\sigma\rangle_+$ is a state $|\chi_\sigma(\mathbf{k})\rangle$ with initial momentum $\mathbf{k}$ which is scattered by impurities until it reaches a momentum anti-aligned with the initial one $-\mathbf{k}$. This change in momentum is usually mapped to an adiabatic change within the parameter space, leading after evolution of the state $|\chi_\sigma\rangle_+ = \exp\left[i\Phi_+\right]|\chi_\sigma(-\mathbf{k})\rangle$ with a Berry phase contribution $\Phi_{\sigma,+}$. $|\chi_\sigma\rangle_-$ is obtained by starting from momentum $-\mathbf{k}$ and arriving at positive $\mathbf{k}$ in exactly reversed order of the scattering processes with Berry phase $\Phi_{\sigma,-}$.

Hence the corresponding phase term should be proportional to Berry phase of this process and determine the sign of the conductance correction - in other words - whether weak localization or antilocalization is measured.

Let us check this simplified picture in the well known context defined by a 2DEG with spin-orbit interaction. All we have to do for this purpose is to calculate the winding number of the curve the effective spin-orbit field $\boldsymbol{\mu}(\boldsymbol{k})$ describes in parameter space during a sweep of the polar angle φ from 0 to 2π.

For convenience we map the inplane effective field of the 2DEG, Eq. (2.26), onto its complex parametrization,

$$\tilde{\tilde{z}}_{\mathrm{2DEG}} = k\left[-i\alpha e^{i\varphi} + \left(\beta - \frac{\tilde{\Gamma}}{4}\right)e^{-i\varphi} + \frac{\tilde{\Gamma}}{4}e^{i3\varphi}\right], \tag{D.11}$$

with $\tilde{\Gamma} = \gamma k^2$. Restricting the material dependent β-parameter to values other than zero, introducing the dimensionless parameters $\Gamma = \tilde{\Gamma}/\beta$ and the ratio of Rashba and Dresselhaus interaction strength $\eta = \alpha/\beta$, and rescaling the norm of $\tilde{\tilde{z}}$, one obtains the equivalent curve

$$\begin{aligned}\tilde{z}_{\mathrm{2DEG}} &= -i\eta e^{i\varphi} + \left(1 - \frac{\Gamma}{4}\right)e^{-i\varphi} + \frac{\Gamma}{4}e^{i3\varphi} \qquad \text{(D.12)}\\ &= -i\eta z + (1 - \frac{\Gamma}{4})z^{-1} + \frac{\Gamma}{4}z^3, \qquad \text{(D.13)}\end{aligned}$$

in terms of the unit circle $z = e^{i\varphi}$ and $\varphi \in [0, 2\pi[$. Analogous to the result (D.13), we obtain a complex parametrization of the effective field describing the lowest heavy hole state in a confinement (2.40),

$$\tilde{\tilde{z}}_{\mathrm{2DHG}} = \frac{k^3}{4\lambda_1}\left[(2c_1+3)e^{i\varphi} + \eta(2c_2+3)ie^{-i\varphi} + 4(1-c_1)e^{-i3\varphi} + 4\eta(1-c_2)ie^{i3\varphi}\right], \tag{D.14}$$

here again with the ratio of extrinsic over intrinsic spin-orbit interaction $\eta = \lambda_2/\lambda_1$

$$\tilde{z}_{\mathrm{2DHG}} = (2c_1+3)z + \eta(2c_2+3)iz^{-1} + 4(1-c_1)z^{-3} + 4\eta(1-c_2)iz^3. \tag{D.15}$$

Since a wavenumber sweep over the Fermi contour can be approximated by an angular sweep [194], the winding number n_C can be obtained from Cauchy's formula

$$n_C = \frac{1}{2\pi i}\oint \frac{\mathrm{d}\tilde{z}}{\tilde{z}}. \tag{D.16}$$

For illustrative purposes we consider the electronic case D.13 without cubic Dresselhaus interactions (i.e. $\Gamma = 0$) and evaluate D.16 to arrive at

$$\begin{aligned}\frac{1}{2\pi i}\oint_C \frac{\mathrm{d}z}{\tilde{z}}\frac{\partial\tilde{z}}{\partial z} &= \frac{1}{2\pi i}\oint_C \mathrm{d}z\frac{-i\eta - z^{-2}}{-i\eta z + z^{-1}} = \frac{1}{2\pi i}\oint_C \frac{\mathrm{d}z}{z}\frac{\eta z^2 - i}{\eta z^2 + i} \qquad \text{(D.17)}\\ \left\{x := \sqrt{|\eta|}\right\} &= \frac{1}{2\pi i}\oint_{C'} \frac{\mathrm{d}x}{x}\frac{x^2 - i\mathrm{sgn}(\eta)}{x^2 + i\mathrm{sgn}(\eta)}, \qquad \text{(D.18)}\end{aligned}$$

where C' is a simple curve with an angle dependent radius

$$r_{C'}(\varphi) = \frac{\sqrt{\eta^2 + 1 + 2\eta\sin 2\varphi}}{\sqrt{|\eta|}}. \tag{D.19}$$

The radius D.19 determines whether the poles of radius 1 entering the integrand in D.18 contribute to the integral or not. We know that each pole contributes an integer number, being the winding number of the closed curve around it. Furthermore, the poles are symmetric with respect to a shift of π, as is $r_{C'}(\varphi)$. From this follows that all poles except the one at $x_0 = 0$ appear pairwise, changing the winding number by an even number. Consequently, the pole at $x_0 = 0$ determines, whether the winding number is even or odd. Here it contributes by a value of 1, which leads to an odd winding number and immediately explains the general observation of WAL in systems with spin-orbit interaction. However, at $\eta = \pm 1$ the radius in the direction $\varphi_\pm$ of the poles

$$r^2_{C'}(\varphi_\pm) = \frac{(\eta - \mathrm{sgn}(\eta))^2}{|\eta|} \tag{D.20}$$

is zero, which becomes clear after a close look at (D.13). In this case the parametrization yields a line $z = \mp e^{i\varphi} + e^{-i\varphi}$ with obviously zero n_C. This explains the observation of WL in the PSH regime.

The argument presented here holds analogous for the 2DHG, in which our approach predicts WAL for any combination of SOI parameters, except for combinations of parameters, that establish the PSH symmetry regime.

Bibliography

[1] C. Betthausen, T. Dollinger, H. Saarikoski, V. Kolkovsky, G. Karczewski, T. Wojtowicz, K. Richter, and D. Weiss, *Spin-Transistor Action via Tunable Landau-Zener Transitions*, Science **337** (2012), 324.

[2] H. Saarikoski, T. Dollinger, and K. Richter, *Spin transmission control in helical magnetic fields*, Phys. Rev. B **86** (2012), 165407.

[3] M. Kohda, V. Lechner, Y. Kunihashi, T. Dollinger, P. Olbrich, C. Schönhuber, I. Caspers, V. V. Bel'kov, L. E. Golub, D. Weiss, K. Richter, J. Nitta, and S. D. Ganichev, *Gate-controlled persistent spin helix state in (In,Ga)As quantum wells*, Phys. Rev. B **86** (2012), 081306.

[4] T. Dollinger, A. Scholz, P. Wenk, R. Winkler, J. Schliemann, and K. Richter, *Signatures of spin-preserving symmetries in two-dimensional hole gases*, 2013, arXiv:1304.7747 [cond-mat.mes-hall].

[5] D. D. Awschalom and M. E. Flatté, *Challenges for semiconductor spintronics*, Nat. Phys. **3** (2007), 153.

[6] Nobelprize.org, *All Nobel prizes in physics*, 2013, http://www.nobelprize.org.

[7] J. Fabian, A. Matos-Abiague, C. Ertler, P. Stano, and I. Zutic, *Semiconductor spintronics*, Acta Phys.Slov. **57** (2007), 565.

[8] B. Behin-Aein, D. Datta, S. Salahuddin, and S. Datta, *Proposal for an all-spin logic device with built-in memory*, Nat. Nano **5** (2010), 1748.

[9] P. W. Shor, *Polynomial-time algorithms for prime factorization and discrete logarithms on a quantum computer*, SIAM J. Comp. **26** (1997), 1484.

[10] L. K. Grover, *From Schrödinger's equation to the quantum search algorithm*, American Journal of Physics **69** (2001), 769.

[11] G. Moore, *Cramming more components onto integrated circuits*, Electronics **38** (1965), 114.

[12] S. Lloyd, *Ultimate physical limits to computation*, Nature **406** (2000), 1047.

[13] V. Mourik, K. Zuo, S. M. Frolov, S. R. Plissard, E. P. A. Bakkers, and L. Kouwenhoven, *Signatures of Majorana fermions in hybrid superconductor-semiconductor nanowire devices*, Science **336** (2012), 1003.

[14] J. Fabian, *Solid-state physics: Spin's lifetime extended*, Nature **458** (2009), 580.

[15] M. N. Baibich, J. M. Broto, A. Fert, F. Nguyen Van Dau, F. Petroff, P. Etienne, G. Creuzet, A. Friederich, and J. Chazelas, *Giant magnetoresistance of (001)Fe/(001)Cr magnetic superlattices*, Phys. Rev. Lett. **61** (1988), 2472.

[16] G. Binasch, P. Grünberg, F. Saurenbach, and W. Zinn, *Enhanced magnetoresistance in layered magnetic structures with antiferromagnetic interlayer exchange*, Phys. Rev. B **39** (1989), 4828.

[17] M. Julliere, *Tunneling between ferromagnetic films*, Phys. Lett. A **54** (1975), 225.

[18] T. Miyazaki and N. Tezuka, *Giant magnetic tunneling effect in Fe/Al2O3/Fe junction*, J. Magn. Magn. Mater. **139** (1995), L231.

[19] J. S. Moodera, L. R. Kinder, T. M. Wong, and R. Meservey, *Large magnetoresistance at room temperature in ferromagnetic thin film tunnel junctions*, Phys. Rev. Lett. **74** (1995), 3273.

[20] M. Wimmer, *Quantum transport in nanostructures: From computational concepts to spintronics in graphene and magnetic tunnel junctions*, Ph.D. thesis, 2008, Universität Regensburg.

[21] S. Datta and B. Das, *Electronic analog of the electro-optic modulator*, App. Phys. Lett. **56** (1990), 665.

[22] S. Bandyopadhyay and M. Cahay, *Alternate spintronic analog of the electro-optic modulator*, App. Phys. Lett. **85** (2004).

[23] J. C. Egues, G. Burkard, and D. Loss, *Datta–das transistor with enhanced spin control*, App. Phys. Lett. **82** (2003), 2658.

[24] D. Loss and D. P. DiVincenzo, *Quantum computation with quantum dots*, Phys. Rev. A **57** (1998), 120.

[25] J. Schliemann, J. C. Egues, and D. Loss, *Nonballistic spin-field-effect transistor*, Phys. Rev. Lett. **90** (2003), 146801.

[26] J. Fabian, I. Zutic, and S. Das Sarma, *Magnetic bipolar transistor*, App. Phys. Lett. **84** (2004), 85.

[27] N. Rangaraju, J. A. Peters, and B. W. Wessels, *Magnetoamplification in a bipolar magnetic junction transistor*, Phys. Rev. Lett. **105** (2010), 117202.

[28] H. C. Koo, J. H. Kwon, J. Eom, J. Chang, S. H. Han, and M. Johnson, *Control of spin precession in a spin-injected field effect transistor*, Science **325** (2009), 1515.

[29] I. Adagideli, V. Lutsker, M. Scheid, Ph. Jacquod, and K. Richter, *Spin transistor action from hidden onsager reciprocity*, Phys. Rev. Lett. **108** (2012), 236601.

[30] E. I. Rashba, *Properties of semiconductors with an extremum loop. 1. cyclotron and combinational resonance in a magnetic field perpendicular to the plane of the loop*, Sov. Phys. Solid State **2** (1960), 1109.

[31] Bychkov Y. A. and E. I. Rashba, *Oscillatory effects and the magnetic susceptibility of carriers in inversion layers*, J. Phys. C: Solid State Physics **17** (1984), 6039.

[32] G. Dresselhaus, *Spin-orbit coupling effects in zinc blende structures*, Phys. Rev. **100** (1955), 580.

[33] J. Nitta, T. Akazaki, H. Takayanagi, and T. Enoki, *Gate control of spin-orbit interaction in an inverted* $In_{0.53}Ga_{0.47}As/In_{0.52}Al_{0.48}As$ *heterostructure*, Phys. Rev. Lett. **78** (1997), 1335.

[34] G. Schmidt, D. Ferrand, L. W. Molenkamp, A. T. Filip, and B. J. van Wees, *Fundamental obstacle for electrical spin injection from a ferromagnetic metal into a diffusive semiconductor*, Phys. Rev. B **62** (2000), R4790.

[35] I. Žutić, J. Fabian, and S. Das Sarma, *Spintronics: Fundamentals and applications*, Rev. Mod. Phys. **76** (2004), 323.

[36] P. Wenk and S. Kettemann, *Spin relaxation in quantum wires*, Handbook on Nanophysics (2010), 49.

[37] L. Onsager, *Reciprocal relations in irreversible processes. ii.*, Phys. Rev. **38** (1931), 2265.

[38] B. A. Bernevig, J. Orenstein, and S.-C. Zhang, *Exact SU(2) symmetry and persistent spin helix in a spin-orbit coupled system*, Phys. Rev. Lett. **97** (2006), 236601.

[39] J. D. Koralek, C. P. Weber, J. Orenstein, B. A. Bernevig, S.-C. Zhang, S. Mack, and D. D. Awschalom, *Emergence of the persistent spin helix in semiconductor quantum wells*, Nature **458** (2009), 610.

[40] M. P. Walser, C. Reichl, W. Wegscheider, and G. Salis, *Direct mapping of the formation of a persistent spin helix*, Nat. Phys. **8** (2012), 757.

[41] F. G. Pikus and G. E. Pikus, *Conduction-band spin splitting and negative magnetoresistance in a_3b_5 heterostructures*, Phys. Rev. B **51** (1995), 16928.

[42] W. Knap, C. Skierbiszewski, A. Zduniak, E. Litwin-Staszewska, D. Bertho, F. Kobbi, J. L. Robert, G. E. Pikus, F. G. Pikus, S. V. Iordanskii, V. Mosser, K. Zekentes, and Yu. B. Lyanda-Geller, *Weak antilocalization and spin precession in quantum wells*, Phys. Rev. B **53** (1996), 3912.

[43] E. I. Rashba and E. Y. Sherman, *Spin-orbital band splitting in symmetric quantum wells*, Phys. Lett. A **129** (1988), 175.

[44] R. Winkler, H. Noh, E. Tutuc, and M. Shayegan, *Anomalous Rashba spin splitting in two-dimensional hole systems*, Phys. Rev. B **65** (2002), 155303.

[45] D. V. Bulaev and D. Loss, *Spin relaxation and decoherence of holes in quantum dots*, Phys. Rev. Lett. **95** (2005), 076805.

[46] J. K. Furdyna, *Diluted magnetic semiconductors*, J. App. Phys. **64** (1988), R29.

[47] M. Wimmer and K. Richter, *Optimal block-tridiagonalization of matrices for coherent charge transport*, J. Comp. Phys. **228** (2009), 8548.

[48] L. Landau, *Zur Theorie der Energieübertragung. II*, Phys. Z. d. Sov. Union **2** (1932), 46.

[49] C. Zener, *Non-adiabatic crossing of energy levels*, Proc. R. Soc. Lon. A **137** (1932), 696.

[50] J. D. Bjorken and S. D. Drell, *Relativistische Quantenmechanik*, BI-Wissenschaftsverlag Mannheim Wien Zürich, 1990.

[51] N. Tombros, C. Jozsa, M. Popinciuc, H. T. Jonkman, and B. J. van Wees, *Electronic spin transport and spin precession in single graphene layers at room temperature*, Nature **448** (2007), 571.

[52] S. Datta, *Electronic transport in mesoscopic systems*, Cambridge University Press, Cambridge, 1995.

[53] R. Winkler, *Spin-orbit coupling effects in two-dimensional electron and hole systems*, Springer, Berlin, 2003.

[54] N.W. Ashcroft and N.D. Mermin, *Festkörperphysik*, Oldenbourg Wissenschaftsverlag, München, 2005.

[55] E. O. Kane, *Band structure of indium antimonide*, J. Phys. Chem. Sol. **1** (1957), 249.

[56] J. M. Luttinger, *The effect of a magnetic field on electrons in a periodic potential*, Phys. Rev. **84** (1951), 814.

[57] P. O. Löwdin, *A note on the quantum-mechanical perturbation theory*, J. Chem. Phys. **19** (1951), 1396.

[58] G. L. Bir and G. E. Pikus, *Symmetry and strain-induced effects in semiconductors*, John Wiley and Sons New York Toronto, 1974.

[59] G. Czycholl, *Theoretische Festkörperphysik*, Springer-Verlag Berlin Heidelberg, 2004.

[60] J. M. Luttinger and W. Kohn, *Motion of electrons and holes in perturbed periodic fields*, Phys. Rev. **97** (1955), 869.

[61] J. M. Luttinger, *Quantum theory of cyclotron resonance in semiconductors: General theory*, Phys. Rev. **102** (1956), 1030.

[62] T. Dietl, *A ten-year perspective on dilute magnetic semiconductors and oxides*, Nat. Mater. **9** (2010), 965.

[63] J. König and A. H. MacDonald, *EPR and ferromagnetism in diluted magnetic semiconductor quantum wells*, Phys. Rev. Lett. **91** (2003), 077202.

[64] M Scheid, *Tailoring semiconductor spintronics devices: Tools for the creation and control of spins in two-dimensional electron gases*, Ph.D. thesis, 2010, Universität Regensburg.

[65] M. Abramowitz and I. A. Stegun, *Handbook of mathematical functions*, Dover Publications, New York, 1970.

[66] A. W. Holleitner, V. Sih, A. C. Gossard, and D. D. Awschalom, *Dimensionally constrained D'yakonov–Perel' spin relaxation in n-InGaAs channels: transition from 2D to 1D*, Nat. Phys. **9** (2007), 342.

[67] S. Giglberger, L. E. Golub, V. V. Bel'kov, S. N. Danilov, D. Schuh, C. Gerl, F. Rohlfing, J. Stahl, W. Wegscheider, D. Weiss, W. Prettl, and S. D. Ganichev, *Rashba and Dresselhaus spin splittings in semiconductor quantum wells measured by spin photocurrents*, Phys. Rev. B **75** (2007), 035327.

[68] F. J. Jedema, H. B. Heersche, A. T. Filip, J. J. A. Baselmans, and B. J. van Wees, *Electrical detection of spin precession in a metallic mesoscopic spin valve*, Nature **458** (2009), 610.

[69] M. Scheid, I. Adagideli, J. Nitta, and K. Richter, *Anisotropic universal conductance fluctuations in disordered quantum wires with Rashba and Dresselhaus spin–orbit interaction and an applied in-plane magnetic field*, Semicond. Sci. Tenchnol. **24** (2009), 064005.

[70] E. D. Black and J. C. Price, *Spin–Zeeman splitting and weak localization in lithium films*, Physica B **269** (1999), 1.

[71] T. Koga, J. Nitta, T. Akazaki, and H. Takayanagi, *Rashba spin-orbit coupling probed by the weak antilocalization analysis in InAlAs/InGaAs/InAlAs quantum wells as a function of quantum well asymmetry*, Phys. Rev. Lett. **89** (2002), 046801.

[72] S. Faniel, T. Matsuura, S. Mineshige, Y. Sekine, and T. Koga, *Determination of spin-orbit coefficients in semiconductor quantum wells*, Phys. Rev. B **83** (2011), 115309.

[73] D. K. Ferry and S. M. Goodnick, *Transport in nanostructures*, Cambridge University Press, Cambridge, 1997.

[74] F. Stern, *Quantum properties of surface space-charge layers*, Critical Reviews in Solid State and Materials Sciences **4** (1973), 499.

[75] V. Krueckl, M. Wimmer, I. Adagideli, J. Kuipers, and K. Richter, *Weak localization in mesoscopic hole transport: Berry phases and classical correlations*, Phys. Rev. Lett. **106** (2011), 146801.

[76] D. Neumaier, K. Wagner, S. Geiß ler, U. Wurstbauer, J. Sadowski, W. Wegscheider, and D. Weiss, *Weak Localization in Ferromagnetic (Ga,Mn)As nanostructures*, Phys. Rev. Lett. **99** (2007), 116803.

[77] I. Garate, J. Sinova, T. Jungwirth, and A. H. MacDonald, *Theory of weak localization in ferromagnetic (Ga,Mn)As*, Phys. Rev. B **79** (2009), 155207.

[78] N. S. Averkiev, L. E. Golub, and G. E. Pikus, *Anomalous magnetoresistance in p-type quantum wells*, Solid State Communications **107** (1998), 757.

[79] X. Bi, P. He, E. M. Hankiewicz, R. Winkler, G. Vignale, and D. Culcer, *Anomalous spin precession and spin Hall effect in semiconductor quantum wells*, Phys. Rev. B **88** (2013), 035316.

[80] S. Kettemann, *Dimensional control of antilocalization and spin relaxation in quantum wires*, Phys. Rev. Lett. **98** (2007), 176808.

[81] P. Wenk and S. Kettemann, *Dimensional dependence of weak localization corrections and spin relaxation in quantum wires with Rashba spin-orbit coupling*, Phys. Rev. B **81** (2010), 125309.

[82] J. Fischer and D. Loss, *Hybridization and spin decoherence in heavy-hole quantum dots*, Phys. Rev. Lett. **105** (2010), 266603.

[83] N. O. Lipari and A. Baldereschi, *Angular momentum theory and localized states in solids. investigation of shallow acceptor states in semiconductors*, Phys. Rev. Lett. **25** (1970), 1660.

[84] A. Scholz, T. Dollinger, P. Wenk, K. Richter, and J. Schliemann, *Plasmons in spin-orbit coupled two-dimensional hole gas systems*, Phys. Rev. B **87** (2013), 085321.

[85] P. A. Mello and N. Kumar, *Quantum transport in mesoscopic systems*, Oxford University Press, Oxford, 2004.

[86] R. Blümel and U. Smilansky, *Classical irregular scattering and its quantum-mechanical implications*, Phys. Rev. Lett. **60** (1988), 477.

[87] R. A. Jalabert, H. U. Baranger, and A. D. Stone, *Conductance fluctuations in the ballistic regime: A probe of quantum chaos?*, Phys. Rev. Lett. **65** (1990), 2442.

[88] P. W. Anderson, *Absence of diffusion in certain random lattices*, Phys. Rev. **109** (1958), 1492.

[89] B. L. Altshuler, D. Khmel'nitzkii, A. I. Larkin, and P. A. Lee, *Magnetoresistance and Hall effect in a disordered two-dimensional electron gas*, Phys. Rev. B **22** (1980), 5142.

[90] G. Bergmann, *Weak localization in thin films: a time-of-flight experiment with conduction electrons*, Phys. Rep. **107** (1984), 1.

[91] S. Hikami, A. I. Larkin, and Y. Nagaoka, *Spin-orbit interaction and magnetoresistance in the two dimensional random system*, Prog. of Theo. Phys. **63** (1980), 707.

[92] D. Waltner and K. Richter, *Classical correlations and quantum interference in ballistic conductors*, Handbook of Nonlinear Dynamics in Nanosystems, Wiley-VCH, Weinheim (2009).

[93] H. U. Baranger, R. A. Jalabert, and A. D. Stone, *Quantum-chaotic scattering effects in semiconductor microstructures*, Chaos **3** (1993), 665.

[94] K. Richter and M. Sieber, *Semiclassical theory of chaotic quantum transport*, Phys. Rev. Lett. **89** (2002), 206801.

[95] O. Zaitsev, D. Frustaglia, and K. Richter, *Semiclassical theory of weak antilocalization and spin relaxation in ballistic quantum dots*, Phys. Rev. B **72** (2005), 155325.

[96] L. P. Gor'kov, A. I. Larkin, and D. E. Khmel'nitskii, *Particle conductivity in a two-dimensional random potential*, JETP Lett. **30** (1980), 228.

[97] H. Bruus and K. Flensberg, *Many-body quantum theory in condensed matter physics: An introduction*, Oxford University Press, Oxford, 2004.

[98] A. Lagendkjk, B. van Tiggelen, and D. Wiersma, *Fifty years of Anderson localization*, Phys. Today (2009), 24.

[99] B. L. Altshuler, A. G. Aronov, and P. A. Lee, *Interaction effects in disordered fermi systems in two dimensions*, Phys. Rev. Lett. **44** (1980), 1288.

[100] N.S. Averkiev, L.E. Golub, and G.E. Pikus, *Weak localization in semiconductor structures with strong spin-orbit coupling*, Journal of Experimental and Theoretical Physics **86** (1998), 780.

[101] M. M. Glazov and L. E. Golub, *Nondiffusive weak localization in two-dimensional systems with spin-orbit splitting of the spectrum*, Semicond. **40** (2006), 1209.

[102] K. Richter, *Semiclassical theory of mesoscopic quantum systems*, 1997, Habilitation thesis, Universität Augsburg.

[103] T. Ando, *Quantum point contacts in magnetic fields*, Phys. Rev. B **44** (1991), 8017.

[104] R. Kubo, *A general expression for the conductivity tensor*, Can. J. Phys. **34** (1956), 1274.

[105] R. Landauer, *Spatial variation of currents and fields due to localized scatterers in metallic conduction*, IBM J. Res. Develop. **1** (1957), 223.

[106] B. J. van Wees, H. van Houten, C. W. J. Beenakker, J. G. Williamson, L. P. Kouwenhoven, D. van der Marel, and C. T. Foxon, *Quantized conductance of point contacts in a two-dimensional electron gas*, Phys. Rev. Lett. **60** (1988), 848.

[107] M. Büttiker, Y. Imry, R. Landauer, and S. Pinhas, *Generalized many-channel conductance formula with application to small rings*, Phys. Rev. B **31** (1985), 6207.

[108] S. Chakravarty and A. Schmid, *Weak localization: the quasiclassical theory of electrons in a random potential*, Phys. Rep. **140** (1986), 193.

[109] K. von Klitzing, *The quantized Hall effect*, Rev. Mod. Phys. **58** (1986), 519.

[110] D. S. Fisher and P. A. Lee, *Relation between conductivity and transmission matrix*, Phys. Rev. B **23** (1981), 6851.

[111] R. Peierls, *Zur Theorie des Diamagnetismus von Leitungselektronen*, Z. Phys. **80** (1933), 763.

[112] I. N. Bronstein, K. A. Semendjajew, G. Musiol, and H. Mühlig, *Taschenbuch der Mathematik*, Verlag Harri Deutsch, Franfurt am Main, 2001.

[113] M. C. Gutzwiller, *Chaos in classical and quantum mechanics*, Springer, New York, 1990.

[114] J. Bolte and S. Keppeler, *A semiclassical approach to the Dirac equation*, Annals of Physics **274** (1999), 125.

[115] M. C. Gutzwiller, *Phase-integral approximation in momentum space and the bound states of an atom*, J. Math. Phys. **8** (1967), 1979.

[116] H.-J. Stöckmann, *Quantum chaos - an introduction*, Cambridge University Press, Cambridge, 1999.

[117] P. Wenk, *Itinerant spin dynamics in structures of reduced dimensionality*, Ph.D. thesis, 2011, Jacobs University Bremen.

[118] L. H. Thomas, *The kinematics of an electron with an axis*, Phil. Mag. **3** (1927), 1.

[119] B. J. van Wees, H. van Houten, C. W. J. Beenakker, and J. G. Williamson, *Quantized conductance of point contacts in a two-dimensional electron gas*, Phys. Rev. Lett **60** (1988), 848.

[120] G. Vattay, J. Cserti, G. Palla, and G. Szalka, *Diffraction in the semiclassical description of mesoscopic devices*, Chaos **8** (1997), 1031.

[121] L. Wirtz, J.-Z. Tang, and J. Burgdörfer, *Geometry-dependent scattering through ballistic microstructures: Semiclassical theory beyond the stationary-phase approximation*, Phys. Rev. B **56** (1997), 7589.

[122] İ. Adagideli, P. Jacquod, M. Scheid, M. Duckheim, D. Loss, and K. Richter, *Geometric correlations and breakdown of mesoscopic universality in spin transport*, Phys. Rev. Lett. **105** (2010), 246807.

[123] R. Balian and Bloch C., *Distribution of eigenfrequencies for the wave equation in a finite domain : I. three-dimensional problem with smooth boundary surface*, Annals of Physics **60** (1970), 401.

[124] R. Balian and C. Bloch, *Asymptotic evaluation of the green's function for large quantum numbers*, Annals of Physics **63** (1971), 592.

[125] R. Balian and C. Bloch, *Solution of the schrödinger equation in terms of classical paths*, Annals of Physics **85** (1974), 514.

[126] A. D. Mirlin, E. Altshuler, and P. Wölfle, *Quasiclassical approach to impurity effect on magnetooscillations in 2d metals*, (1995), arXiv:cond-mat/9507081.

[127] D. Weiss, K. Richter, A. Menschig, R. Bergmann, H. Schweizer, K. von Klitzing, and G. Weimann, *Quantized periodic orbits in large antidot arrays*, Phys. Rev. Lett. **70** (1993), 4118.

[128] H. C. Koo, H. Yi, J.-B. Ko, J. Chang, S.-H. Han, D. Jung, S.-G. Huh, and J. Eom, *Electrical spin injection and detection in an InAs quantum well*, App. Phys. Lett. **90** (2007), 022101.

[129] M. Born and V. Fock, *Beweis des Adiabatensatzes*, Zeitschrift für Physik A **51** (1928), 165.

[130] J. D. Jackson, *Classical electrodynamics*, John Wiley and Sons Inc., New York, 1999.

[131] M. Calvo, *Quantum theory of neutrons in helical magnetic fields*, Phys. Rev. B **18** (1978), 5073.

[132] C. Jia and J. Berakdar, *Tunneling anisotropic magnetoresistance of helimagnet tunnel junctions*, Phys. Rev. B **81** (2010), 052406.

[133] C. Betthausen, *Spin effects in high- and low-field magnetotransport experiments in semimagnetic $Cd_{1-x}Mn_xTe$ heterostructures*, Ph.D. thesis, 2012, Universität Regensburg.

[134] J. W. Kim, Kim N., and T. W. Kang, *Spin currents modulated by magnetic barriers in semiconductor nanowires*, Semicond. Sci. Technol. **21** (2006), 647.

[135] I. S. Ibrahim and F. M. Peeters, *The magnetic Kronig–Penney model*, Am. J. Phys. **63** (1995), 171.

[136] I. S. Ibrahim and F. M. Peeters, *Two-dimensional electrons in lateral magnetic superlattices*, Phys. Rev. B **52** (1995), 17321.

[137] G. A. Hagedorn and A. Joye, *Determination of non-adiabatic scattering wave functions in a Born-Oppenheimer model*, (2004), arXiv:math-ph/0406041.

[138] M. V. Berry, *Quantal phase factors accompanying adiabatic changes*, Proc. R. Soc. Lon. A **392** (1984), 45.

[139] S. Blanes, F. Casas, J. A. Oteo, and J. Ros, *The Magnus expansion and some of its applications*, Phys. Rep. **470** (2009), 151.

[140] J. P. Davis and P. Pechukas, *Nonadiabatic transitions induced by a time-dependent Hamiltonian in the semiclassical/adiabatic limit: The two-state case*, J. Chem. Phys. **64** (1975), 3129.

[141] A.S. Mel'nikov, S.V. Mironov, and S.V. Sharov, *Dephasing time and magnetoresistance of two-dimensional electron gas in spatially modulated magnetic fields*, Phys. Rev. B **81** (2010), 115308.

[142] F. Schwabl, *Quantum mechanics*, Springer, Berlin Heidelberg, 1992.

[143] M. Popp, D. Frustaglia, and K. Richter, *Conditions for adiabatic spin transport in disordered systems*, Phys. Rev. B **68** (2003), 041303.

[144] A. Stern, *Berry's phase, motive forces, and mesoscopic conductivity*, Phys. Rev. Lett. **68** (1992), 1022.

[145] A. G. Mal'shukov and K. A. Chao, *Waveguide diffusion modes and slowdown of D'yakonov-Perel' spin relaxation in narrow two-dimensional semiconductor channels*, Phys. Rev. B **61** (2000), R2413.

[146] T. Dietl, H. Ohno, F. Matsukura, J. Cibert, and D. Ferrand, *Zener model description of fe<rromagnetism in zinc-blende magnetic semiconductors*, Science **289** (2000), 1019.

[147] J. C. Slonczewski, *Current-driven excitation of magnetic multilayers*, J. Magn. Magn. Mater. **159** (1996), L1.

[148] M. Buhl, A. Erbe, J. Grebing, S. Wintz, J. Raabe, and J. Fassbender, *Lateral spin transfer torque induced magnetic switching at room temperature demonstrated by x-ray microscopy*, Sci. Rep. **3** (2013), 2945.

[149] J. Rammer, *Quantum transport theory*, Westview Press, 2008.

[150] J. S. Langer and T. Neal, *Breakdown of the concentration expansion for the impurity resistivity of metals*, Phys. Rev. Lett. **16** (1966), 984.

[151] L. S. Schulman, *Techniques and applications of path integration*, Wiley New York, 1996.

[152] A. M. Chang, H. U. Baranger, L. N. Pfeiffer, and K. W. West, *Weak localization in chaotic versus nonchaotic cavities: A striking difference in the line shape*, Phys. Rev. Lett. **73** (1994), 2111.

[153] Y. Aharonov and D. Bohm, *Significance of electromagnetic potentials in the quantum theory*, Phys. Rev. **115** (1959), 485.

[154] I. S. Gradshteyn and I.M. Ryzhik, *Table of integrals, series, and products*, 4 ed., Academic Press, New York London, 1965.

[155] C. W. J. Beenakker, *Random-matrix theory of quantum transport*, Rev. Mod. Phys. **69** (1997), 731.

[156] M. I. Dyakonov and V. I. Perel, *Possiblity of orientating electron spins with current*, Sov. Phys. JETP Lett. **13** (1971), 467.

[157] Matthias C. Lüffe, Janik Kailasvuori, and Tamara S. Nunner, *Relaxation mechanisms of the persistent spin helix*, Phys. Rev. B **84** (2011), 075326.

[158] R. J. Elliott, *Theory of the effect of spin-orbit coupling on magnetic resonance in some semiconductors*, Phys. Rev. **96** (1954), 266.

[159] Y. Yafet, *g factors and spin-lattice relaxation of conduction electrons*, Solid State Phys. **14** (1963), 1.

[160] G. Bir, A. Aronov, and Pikus G., *Spin relaxation of electrons scattered by holes*, Sov. Phys. JETP **42** (1975), 705.

[161] T. D. Stanescu and V. Galitski, *Spin relaxation in a generic two-dimensional spin-orbit coupled system*, Phys. Rev. B **75** (2007), 125307.

[162] M. Duckheim, D. Loss, M. Scheid, K. Richter, I. Adagideli, and P. Jacquod, *Spin accumulation in diffusive conductors with Rashba and Dresselhaus spin-orbit interaction*, Phys. Rev. B **81** (2010), 085303.

[163] E. L. Ivchenko, *Optical spectroscopy of semiconductor nanostructures*, Alpha Science Int., Harrow UK, 2006.

[164] V. Belkov and S. Ganichev, *Cubic-in-k spin splitting in (001)-grown QW structures*, unpublished.

[165] M. Scheid, M. Kohda, Y. Kunihashi, K. Richter, and J. Nitta, *All-electrical detection of the relative strength of Rashba and Dresselhaus spin-orbit interaction in quantum wires*, Phys. Rev. Lett. **101** (2008), 266401.

[166] I. L. Aleiner and V. I. Fal'ko, *Spin-orbit coupling effects on quantum transport in lateral semiconductor dots*, Phys. Rev. Lett. **87** (2001), 256801.

[167] Sacksteder V. E. IV and B. A. Bernevig, *Hole spin helix: Anomalous spin diffusion in anistropic strained hole quantum wells*, 2013, arXiv:1308.4248 [cond-mat.mes-hall].

[168] T. L. Hoghes, Y. B. Bazaliy, and B. A. Bernevig, *Transport equations and spin-charge propagating mode in a strongly confined two-dimensional hole gas*, Phys. Rev. B **74** (2006), 193316.

[169] M. V. Berry, *The quantum phase, five years after*, World Scientific (1989), 7.

[170] H. Ohno, A. Shen, F. Matsukura, A. Oiwa, A. Endo, S. Katsumoto, and Y. Iye, *(Ga,Mn)As: A new diluted magnetic semiconductor based on gaas*, App. Phys. Lett. **69** (1996), 363.

[171] K. Y. Wang, R. P. Campion, K. W. Edmonds, M. Sawicki, T. Dietl, C. T. Foxon, and B. L. Gallagher, *Magnetism in (Ga,Mn)As thin films with* T_C *up to 173K*, AIP Conf. Proc. **772** (2005), 333.

[172] A. Zenesini, H. Lignier, G. Tayebirad, J. Radogostowicz, D. Ciampini, R. Mannella, S. Wimberger, O. Morsch, and E. Arimondo, *Time-resolved measurement of Landau-Zener tunneling in periodic potentials*, Phys. Rev. Lett. **103** (2009), 090403.

[173] T. Köhler, K. Góral, and P. S. Julienne, *Production of cold molecules via magnetically tunable Feshbach resonances*, Rev. Mod. Phys. **78** (2006), 1311.

[174] M. Sillanpää, T. Lehtinen, A. Paila, Y. Makhlin, and P. Hakonen, *Continuous-time monitoring of Landau-Zener interference in a Cooper-pair box*, Phys. Rev. Lett. **96** (2006), 187002.

[175] G. Cao, H.-O. Li, T. Tu, L. Wang, C. Zhou, M. Xiao, G.-C. Guo, H.-W. Jiang, and G.-P. Guo, *Ultrafast universal quantum control of a quantum-dot charge qubit using Landau–Zener–Stückelberg interference*, Nat. Commun. **4** (2013), 1401.

[176] A. J. Olson, S.-J. Wang, R. J. Niffenegger, C.-H. Li, C. H. Greene, and Y. P. Chen, *Tunable Landau-Zener transitions in a spin-orbit coupled Bose-Einstein condensate*, 2013, arXiv:1310.1818 [cond-mat.quant-gas].

[177] H. R. Lewis and W. B. Riesenfeld, *An exact quantum theory of the time-dependent harmonic oszillator of a charged particle in a time-dependent electromagnetic field*, J. Math. Phys. **10** (1969), 1458.

[178] X. Chen, I. Lizuain, A. Ruschhaupt, D. Guéry-Odelin, and J. G. Muga, *Shortcut to adiabatic passage in two- and three-level atoms*, Phys. Rev. Lett. **105** (2010), 123003.

[179] E. Torrentegui, S. Ibáñez, S. Martínez-Garaot, M. Modugno, A. del Campo, D. Guéry-Odelin, A. Ruschhaupt, X. Chen, and J. G. Muga, *Shortcuts to adiabaticity*, 2012, arXiv:1212.6343 [quant-ph].

[180] S. Müller, S. Heusler, P. Braun, and F. Haake, *Semiclassical approach to chaotic quantum transport*, New J. Phys. **9** (2007), 12.

[181] M. Sieber, *Geometrical theory of diffraction and spectral statistics*, J. Phys. A: Math. Gen. **32** (1999), 7679.

[182] H. U. Baranger, R. A. Jalabert, and A. D. Stone, *Weak localization and integrability in ballistic cavities*, Phys. Rev. Lett. **70** (1993), 3876.

[183] L. Wirtz, C. Stampfer, S. Rotter, and J. Burgdörfer, *Semiclassical theory for transmission through open billiards: Convergence towards quantum transport*, Phys. Rev. E **67** (2003), 016206.

[184] C. Stampfer, S. Rotter, J. Burgdörfer, and L. Wirtz, *Pseudopath semiclassical approximation to transport through open quantum billiards: Dyson equation for diffractive scattering*, Phys. Rev. E **72** (2005), 036223.

[185] I. Březinová, C. Stampfer, L. Wirtz, S. Rotter, and J. Burgdörfer, *Diffractive paths for weak localization in quantum billiards*, Phys. Rev. B **77** (2008), 165321.

[186] M. Tabor, *Chaos and integrability in nonlinear dynamics - an introduction*, John Wiley and Sons Inc., New York, 1989.

[187] Y. Aharonov and J. Anandan, *Phase change during a cyclic quantum evolution*, Phys. Rev. Lett. **58** (1987), 1593.

[188] J. H. Hannay, *Angle variable holonomy in adiabatic excursion of an integrable Hamiltonian*, J. Phys. A: Math. Gen. **18** (1985), no. 2, 221.

[189] J. Anandan, *The geometric phase*, Nature **360** (1992), 307.

[190] K. Richter, *The ABC of Aharonov effects*, Physics **5** (2012), 22.

[191] Y. Aharonov and A. Casher, *Topological quantum effects for neutral particles*, Phys. Rev. Lett. **53** (1984), 319.

[192] Y. B. Lyanda-Geller, *Berry phase, conductance oscillations and phase breaking in mesoscopic transport*, Surface Science **361/362** (1996), 692.

[193] M. Z. Hasan and C. L. Kane, *Colloquium: Topological insulators*, Rev. Mod. Phys. **82** (2010), 3045.

[194] Ando T., *Theory of electronic states and transport in carbon nanotubes*, J. Phys. Soc. Jpn. **74** (2005), 777.

References of the author

- C. Betthausen, **T. Dollinger**, H. Saarikoski, V. Kolkovsky, G. Karczewski, T. Wojtowicz, K. Richter, and D. Weiss, *Spin-transistor action via tunable Landau-Zener transitions*, Science **337** (2012), 324.
- H. Saarikoski, **T. Dollinger**, and K. Richter, *Spin transmission control in helical magnetic fields*, Phys. Rev. B **86** (2012), 165407.
- M. Kohda, V. Lechner, Y. Kunihashi, **T. Dollinger**, P. Olbrich, C. Schönhuber, I. Caspers, V. V. Bel'kov, L. E. Golub, D. Weiss, K. Richter, J. Nitta, and S. D. Ganichev, *Gate-controlled persistent spin helix state in (In,Ga)As quantum wells*, Phys. Rev. B **86** (2012), 081306.
- A. Scholz, **T. Dollinger**, P. Wenk, K. Richter, and J. Schliemann. *Plasmons in spin-orbit coupled two-dimensional hole gas systems* Phys. Rev. B **87** (2013), 085321
- **T. Dollinger**, A. Scholz, P. Wenk, R. Winkler, J. Schliemann, and K. Richter. *Signatures of spin-preserving symmetries in two-dimensional hole gases*, arXiv:1304.7747 [cond-mat.mes-hall] (2013). (submitted to Phys. Rev. B)

List of Figures

Acknowledgments

I want to thank everybody who made the present work possible.

I am indebted to the supervisor of this thesis, Prof. Klaus Richter, who always provided valuable guidance during the creation of this work, on a scientific as well as on a personal level. I enjoyed the inspiring conversations with him and the other collaborators of my research projects.

The key ideas of the findings presented here have to a significant portion been enabled by the contributions of Dr. Henri Saarikoski, Dr. Christian Bettausen, Dr. Jan Fischer, Prof. Dieter Weiss, Prof. Sergey Ganichev, Prof. Junsaku Nitta, Prof. John Schliemann, Prof. Roland Winkler, Dr. Paul Wenk and Andreas Scholz.

I am grateful to Michael Wimmer for providing the framework of his transport algorithm, which was essential for the numerical results in this thesis.

Moreover, I want to thank the remaining colleagues at the chair Richter, who made my extended stay a very pleasant and interesting experience.

I would also like to thank the following people, for carefully reading portions of my thesis: Dr. Viktor Krückl, Jan Bundesmann, Josef Michl and Michael Schnitzbauer.

I furthermore acknowledge the organizations my work was funded by, the Elitenetzwerk Bayern and the DFG within the collaborative research project SFB689.

Last but not least I am grateful for the support of my family, my parents, grandparents and my wife Sylvia.

Regensburg, December 2013